

**MAXIMIZING THE SIGNAL-TO-NOISE
RATIO OF DIVERGING ULTRASONIC
WAVES IN MULTIPLE SCATTERING,
ATTENUATING, AND DIFFRACTING
MEDIA**

A DISSERTATION SUBMITTED TO
THE GRADUATE SCHOOL OF ENGINEERING AND SCIENCE
OF BILKENT UNIVERSITY
IN PARTIAL FULFILLMENT OF THE REQUIREMENTS FOR
THE DEGREE OF
DOCTOR OF PHILOSOPHY
IN
ELECTRICAL AND ELECTRONICS ENGINEERING

By
Yasin Kumru
September 2022

Copyright Information

This thesis includes content from the following publications:

© “Reproduced from [Yasin Kumru and Hayrettin Köymen, “Signal-to-noise ratio of diverging waves in multiscattering media: Effects of signal duration and divergence angle”, *The Journal of the Acoustical Society of America* 151, 955-966 (2022) <https://doi.org/10.1121/10.0009410>], with permission of Acoustical Society of America. Copyright [2022], Acoustical Society of America.”

© 2021 arXiv, Reprinted, with permission, from Y. Kumru and H. Köymen, “Coded divergent waves for fast ultrasonic imaging: Optimization and comparative performance analysis,” arXiv, *Signal Processing (eess.SP)*, April 2021, <https://doi.org/10.48550/arXiv.2104.10526>. All rights reserved.

© 2021 arXiv, Reprinted, with permission, from Y. Kumru and H. Köymen, “Ultrasonic array characterization in multiscattering and attenuating media using pin targets,” arXiv, *Systems and Control (eess.SY)*, May 2021, <https://doi.org/10.48550/arXiv.2105.14816>. All rights reserved.

Maximizing the Signal-to-Noise Ratio of Diverging Ultrasonic Waves in Multiple Scattering, Attenuating, and Diffracting Media

By Yasin Kumru

September 2022

We certify that we have read this dissertation and that in our opinion it is fully adequate, in scope and in quality, as a dissertation for the degree of Doctor of Philosophy.

Hayrettin Köymen (Advisor)

Abdullah Atalar

Vakur Behçet Ertürk

Nevzat Güneri Gençer

İmam Şamil Yetik

Approved for the Graduate School of Engineering and Science:

Orhan Arıkan

Director of the Graduate School

ABSTRACT

MAXIMIZING THE SIGNAL-TO-NOISE RATIO OF DIVERGING ULTRASONIC WAVES IN MULTIPLE SCATTERING, ATTENUATING, AND DIFFRACTING MEDIA

Yasin Kumru

Ph.D. in Electrical and Electronics Engineering

Advisor: Hayrettin Köymen

September 2022

Diverging wave imaging is an unfocused imaging method in which a diverging beam is transmitted to insonify the entire region of interest. This diverging beam is formed by applying appropriate time delays to each transducer array element. It provides a higher data acquisition rate and thus a higher temporal resolution, quantified as a higher frame rate. Therefore, diverging wave imaging is widely used in fast ultrasound imaging applications where rates above 1000 frames per second are required. Diverging wave imaging is generally implemented with phased array transducers having a smaller aperture than their counterparts to increase the field of view.

Although diverging wave imaging allows for a high frame rate, it has a decreased spatial resolution and limited SNR due to the broader unfocused beam transmission compared to conventional focused imaging techniques. Conventional focused imaging techniques employ focused narrow beam transmissions for every image line resulting in a higher spatial resolution and SNR in the focal region. However, it offers approximately 30 frames per second, and thus it is not used in fast ultrasound imaging applications.

There is a trade-off between frame rate, image quality, and SNR in diverging wave imaging. Therefore, fast imaging with high SNR and resolution while maintaining a high frame rate remains a practical problem in medical ultrasound.

This thesis focuses on SNR maximization of diverging waves in weakly and multiple scattering, attenuating, and diffracting media. The primary outcome is that the SNR improves at deeper regions if the transmitted burst duration or the chip signal duration in the case of coded transmission is decreased when diverging waves are used. The maximum SNR is obtained in diverging wave transmission when the transmitted burst or the chip signal is as short-duration as the array permits. This result does not comply with the expectation implying that more transmitted energy results in higher SNR.

The analytical foundation for diverging wave propagation in weakly and multiple scattering media is not sufficient at the level required to derive analytical results. In order to understand this counter-intuitive result, either finite element analysis (FEA) or semi-analytical simulation tools can be utilized. FEA can predict this counter-intuitive result, but detailed modeling of the medium is quite involved and results in very long simulation times, which renders the use of FEA impossible. Unlike the other imaging modalities, the wavelength is on the order of hundred micrometers in medical ultrasound imaging; thus, the simulation of a reasonable tissue volume is impossible. Semi-analytical simulation tools based on linear spatial impulse response produce erroneous results because scatterers are modeled as monopole sources, and multiple scattering is not modeled. As there is no analytical and simulation-based solution for this problem, the experimental verification of the results is presented.

The transmitted ultrasound energy spreads over a broader region in diverging wave imaging. The energy spreading further aggravates due to diffraction and multiple scattering, which may cause energy loss. Keeping the transmitted ultrasound energy within the region of interest prevents this energy loss in diverging wave imaging. Therefore, we determined the optimum diverging wave profile to confine the transmitted ultrasound energy in the imaging sector. Using this optimized profile contributes to the SNR maximization.

Complementary Golay sequences and Binary Phase Shift Keying modulation are used to code the transmitted signal. We used an ultrasound research scanner, a tissue-mimicking phantom, and a 128-element phased array transducer with 70% bandwidth at 7.5 MHz center frequency for data acquisition. The SNR in speckle and pin targets is maximized with respect to chip signal length and code length. The SNR performances of the optimized coded diverging wave and conventional single-focused phased array imaging are compared on a single frame basis. The focal region in the focused scheme is used as a reference.

For the 90° imaging sector, the SNR of an 8-bit coded signal is maximum when the chip signal duration is one cycle of the center frequency. The SNR of the optimized coded diverging wave is higher than that of the conventional single-focused phased array imaging at all depths and regions. One frame of diverging wave data is acquired in 200 microseconds, equivalent to 5000 frames/s, whereas the time required for single-focused phased array imaging is 181 times more.

Keywords: Diffraction, Multiple Scattering Media, Attenuation, Signal-to-Noise Ratio, Diverging Waves, Coded Excitation, Complementary Golay Sequences, Binary Phase Shift Keying Modulation.

ÖZET

ÇOKLU SAÇILMALI, SOĞURMALI VE KİRİNİMLİ ORTAMLARDA İRAKSAYAN ULTRASONİK DALGALARIN SİNYAL GÜRÜLTÜ ORANININ MAKSİMİZASYONU

Yasin Kumru

Elektrik ve Elektronik Mühendisliği, Doktora

Tez Danışmanı: Hayrettin Köymen

Eylül 2022

İraksayan dalga görüntüleme yöntemi odaklamanın kullanılmadığı bir görüntüleme yöntemidir. Bu yöntemde, ıraksayan bir hüzme tüm ilgili bölgeyi aydınlatmak için kullanılır. İraksayan dalga, çevirici dizini elemanlarının her birine uygulanan zaman gecikmeleri ile oluşturulur. Bu yöntem yüksek veri toplama oranı ve dolayısıyla yüksek görüntü kare hızı olarak ölçülen yüksek bir zamansal çözünürlük sağlamaktadır. Bu sebeple, ıraksayan dalga görüntüleme yöntemi saniyede bin görüntü kare hızından daha fazla görüntü kare hızı gerektiren hızlı ultrason görüntüleme uygulamalarında yaygın olarak kullanılmaktadır. İraksayan dalga görüntüleme yöntemi, görüntülenen alanı artırabilmek amacıyla, genellikle daha küçük dizin açıklığına sahip faz dizinli çeviriciler ile kullanılmaktadır.

Daha yüksek görüntü kare hızı oranları sağlmasına rağmen, ıraksayan dalga görüntüleme yöntemi geniş ve odaklanmamış hüzme iletiminden dolayı geleneksel odaklamanın yapıldığı görüntüleme tekniklerine göre daha düşük uzaysal çözünürlüğe ve kısıtlı işaret gürültü oranına (SNR) sahiptir. Geleneksel odaklamalı görüntüleme teknikleri, her bir görüntü hattı için odaklama bölgesinde yüksek SNR ve uzaysal çözünürlük sağlayan dar hüzme iletimini kullanmaktadır.

Fakat bu yöntemde yaklaşık 30 resim kare hız oranı elde edilmektedir ve bu sebepten dolayı hızlı görüntüleme uygulamalarında kullanılmamaktadır.

İraksayan dalga görüntüleme yönteminde; görüntü kare hızı, görüntü kalitesi ve SNR arasında bir denge vardır. Bu nedenle, hızlı görüntüleme yöntemlerinde yüksek görüntü kare hız oranı korunurken yüksek SNR ve çözünürlüğün elde edilebilmesi medikal ultrason alanında çözüme kavuşturulması gereken bir problem olmaya devam etmektedir.

Bu tezde; zayıf ve çoklu saçılımlı, soğurmalı ve kırınımlı ortamlarda, iraksayan dalgaların SNR maksimizasyonuna odaklanılmaktadır. Bu tezde elde edilen asıl sonuç, iraksayan dalgalar kullanıldığında, ortama gönderilen darbenin veya kodlanmış iletim durumunda çip sinyalinin süresi azaldığında, SNR'nin derin bölgelerde iyileşmesidir. İraksayan dalga iletimi kullanıldığında, maksimum SNR, iletilen darbe veya çip sinyali çevirici dizininin izin verdiği kadar kısa süreli olduğunda elde edilir. Bu sonuç, daha fazla iletilen enerjinin daha yüksek SNR ile sonuçlanacağı beklentisiyle uyuşmamaktadır.

Zayıf ve çoklu saçılımlı ortamlarda iraksayan dalga yayılımının analitik temeli, analitik sonuçlar elde etmek için gereken düzeyde yeterli değildir. Bu sezgisel olmayan sonucu anlamak için ya sonlu eleman analizi (FEA) ya da yarı analitik simülasyon araçları kullanılabilir. FEA simülasyonları bu sezgisel olmayan sonucu tahmin edebilir, ancak FEA simülasyonlarında ortamın ayrıntılı modellenmesi oldukça karmaşıktır ve çok uzun simülasyon süreleriyle sonuçlanır. Bu durum FEA simülasyonlarının kullanımını imkansız hale getirir. Diğer görüntüleme yöntemlerinden farklı olarak, medikal ultrason görüntülemesinde dalga boyu yüz mikrometre mertebesindedir; bu nedenle, makul bir doku hacminin simülasyonu imkansızdır. Doğrusal uzaysal dürtü yanıtına dayalı yarı-analitik simülasyon araçları ise hatalı sonuçlar üretir çünkü yarı-analitik simülasyonlarda saçıcılar tek kutuplu kaynaklar olarak modellenir ve çoklu saçılma modellenememektedir. Zayıf ve çoklu saçılımlı ortamlarda iraksayan dalga yayılımı problemine yönelik analitik ve simülasyon tabanlı bir çözüm bulunmadığından, sonuçların deneysel olarak doğrulanması bu tezde sunulmaktadır.

Ortama iletilen ultrason enerjisi, iraksayan dalga görüntüleme yönteminde daha geniş bir bölgeye yayılır. Enerjinin yayılımı, kırınım ve çoklu saçılım nedeniyle daha da fazla olur ve bu da enerji kaybına neden olabilmektedir. Ortama iletilen enerjinin görüntüleme bölgesinde tutulması, iraksayan dalga görüntüleme yönteminde söz konusu enerji kaybını önler. Bu nedenle, ortama iletilen ultrason enerjisini görüntüleme sektörü içerisinde tutabilmek için en uygun iraksayan dalga profilini belirledik. Iraksayan dalga görüntüleme yönteminde en uygun profilin kullanılması SNR maksimizasyonuna katkıda bulunmaktadır.

Ortama iletilen sinyali kodlamak için tümleyici Golay dizileri ve İkili Faz Kaydırmalı Anahtarlama modülasyonu kullanılmıştır. Ölçümlerde veri toplamak amacıyla, bir ultrason araştırma tarayıcısı, doku taklit eden bir fantom ve 7.5 MHz merkez frekansında %70 band genişliğine sahip 128 elemanlı faz dizinli çevirici kullandık. Benek ve pin hedeflerindeki SNR, çip sinyal uzunluğu ve kod uzunluğuna göre maksimize edilmiştir. Optimize edilmiş kodlanmış iraksayan dalga ve geleneksel tek odaklı faz dizinli görüntülemenin SNR performansları, tek kare bazında karşılaştırılmıştır. Odaklamanın yapıldığı görüntüleme yönteminin odak bölgesi SNR karşılaştırmasında referans olarak kullanılmıştır.

90°'lik görüntüleme sektörü için, 8-çiplik kodlanmış sinyalin SNR'si, çip sinyalinin süresi merkez frekansta bir periyod olduğunda maksimum olmaktadır. Optimize edilen kodlanmış iraksayan dalganın SNR'si bütün derinliklerde ve bölgelerde geleneksel tek odaklı faz dizinli görüntüleme tekniği ile elde edilen SNR'den daha yüksektir. Bu çalışmamızda, iraksayan dalga yöntemi kullanılarak bir görüntü karesi oluşturabilmek için gerekli olan veri 200 mikrosaniyede elde edilmiştir. Söz konusu veri toplama hızı 5000 görüntü kare hızına eşdeğerdir. Buna karşılık, geleneksel tek odaklı faz dizinli görüntüleme tekniği için gerekli olan süre 181 kat daha fazladır.

Anahtar sözcükler: Kırınım, Çoklu Saçılmalı Ortam, Soğurma, İşaret Gürültü Oranı, Iraksayan Dalgalar, Kodlanmış Uyarma, Tümleyici Golay Dizileri, İkili Faz Kaydırma Anahtarlama Modülasyonu.

Acknowledgement

I would like to express my sincerest gratitude to my advisor Prof. Hayrettin Köymen for his guidance, contributions, and continuous support throughout the development of this thesis. I have always felt privileged and fortunate to find the opportunity to work with Prof. Hayrettin Köymen. I am grateful for all his patience and belief in me, which made me a confident engineer. I have started closely working with Prof. Köymen since 2011. It was an honor for me to work with him through all these years and benefit from his knowledge and experience. I must thank to him here because in addition to being a knowledgeable advisor, he is an incredible mentor to me in every aspect of life. I will always feel indebted for his endless support and encouragement during my studies. I sincerely hope that my friendship and collaboration with him endure in the future.

I would also like to thank Akif Sinan Taşdelen for his support during the development of my thesis. He was always there for a quick chat and discussion. I owe my deepest gratitude to him. I would also like to thank Dr. Kutay Üstüner for giving valuable feedback during my research.

I acknowledge my colleagues; Dr. İtir Köymen, Dr. Saadettin Güler, Kerem Enhoş, Cem Bülbül, Hüseyin Kağan Oğuz, Elif Aydoğdu Doğru, Aslı Ünlügedik, and Burak Şahinbaş. They are all valuable and lifelong friends to me. I am grateful to them for all beautiful times we had together.

The successful completion of this work would not have been possible without the financial support of TÜBİTAK under project grant 119E509.

I dedicate this thesis to my warm-hearted family. They have always been very inspiring and encouraging. I am thankful for their unconditional care and love. I hope to be a source of happiness for them.

Contents

1. INTRODUCTION	1
1.1 LITERATURE REVIEW	1
1.2 ORGANIZATION OF THIS THESIS	4
2. MEDICAL ULTRASOUND IMAGING	6
2.1 PRINCIPLES OF MEDICAL ULTRASOUND IMAGING.....	7
2.2 PHYSICAL SOUND CHARACTERISTICS	8
2.3 POST-PROCESSING STEPS FOR IMAGE CONSTRUCTION.....	10
3. METHODS & MATERIALS	12
3.1 MEASUREMENT SETUP	12
3.2 IMAGING TECHNIQUES	19
3.2.1 Conventional Single-Focused Phased Array Imaging.....	19
3.2.2 Beamforming in Transmission and Reception in Conventional Single-Focused Phased Array Imaging	20
3.2.3 Diverging Wave Imaging.....	23
3.2.4 Beamforming in Transmission and Reception in Diverging Wave Imaging	24
3.3 SIGNAL ENERGY.....	25
3.3.1 SNR Measurement	25
3.3.2 Noise Level Estimation Using Noise Measurements	26
3.3.3 Speckle Signal Level Estimation Using Speckle Measurements	26
4. SIMULATION RESULTS.....	27
4.1 PRESSURE FIELD SIMULATION	27
4.1.1. Simulation Results for Non-Attenuating Medium	29
4.1.2 Simulation Results for Attenuating Medium	34
4.2 SIMULATION RESULTS USING FIELD-II AND K-WAVE.....	35
5. CODED TRANSMISSION.....	39
5.1 COMPLEMENTARY GOLAY SEQUENCES.....	40
5.2 MODULATION SCHEME.....	46
5.3 TRANSMITTER AND RECEIVER FOR CODED TRANSMISSION.....	47
6. REFERENCE SIGNAL IN ATTENUATING MEDIUM.....	51
6.1 REFERENCE SIGNALS FOR FIXED CODE LENGTH.....	55
6.2 REFERENCE SIGNALS FOR FIXED CHIP LENGTH	57
7. DIVERGING WAVE TRANSMISSION FOR FAST ULTRASOUND IMAGING.....	59
7.1 ULTRASOUND ENERGY CONFINEMENT IN THE REGION OF INTEREST	59
7.2 NOISE IN DIVERGING WAVE IMAGING.....	61
7.3 SNR ALONG THE ARCS IN SPECKLE REGION.....	63
8. EFFECT OF CODE LENGTH ON SNR.....	66
8.1 SNR IN SPECKLE.....	66
8.2 SNR FOR PIN TARGETS	68
8.3 CONTRAST-TO-NOISE RATIO COMPARISON.....	70
9. EFFECT OF CHIP SIGNAL LENGTH ON SNR.....	72
9.1 SNR IN SPECKLE.....	72
9.2 SNR FOR PIN TARGETS	76

10. COMPARISON OF OPTIMIZED DWI WITH CONVENTIONAL SINGLE FOCUSED IMAGING	78
10.1 NOISE IN CSFI	78
10.2 SNR COMPARISON IN THE SPECKLE REGION.....	79
10.3 SNR COMPARISON IN THE PIN TARGET REGION	80
10.4 SSR COMPARISON.....	82
11. DISCUSSION OF RESULTS	83
11.1 PERFORMANCE VARIATION.....	83
11.2 LIMITATIONS AND POTENTIAL IMPROVEMENTS	84
11.3 CODED IMAGES.....	85
11.4 SYSTEM HARDWARE REQUIREMENTS	88
11.5 SOUND SPEED ESTIMATION	88
12. CONCLUSION	91
A MEASUREMENT PROTOCOLS.....	100
A.1 PHANTOM MEASUREMENT PROTOCOL FOR DWI.....	100
A.2 PHANTOM MEASUREMENT PROTOCOL FOR CSFI.....	101
A.3 FRESHWATER MEASUREMENT PROTOCOL	102
A.4 NOISE MEASUREMENT PROTOCOL	103
B ANALYTICAL EXPRESSION FOR PRESSURE	104
B.1 DERIVATION FOR NON-ATTENUATING MEDIUM	104
B.2 DERIVATION FOR ATTENUATING MEDIUM	106
C CHARACTERIZATION OF THE PHASED ARRAY TRANSDUCER USED IN THE MEASUREMENTS	107
C.1 TRANSDUCER DIAGRAM FOR TRANSMISSION AND RECEPTION	107
C.2 COMPARISON OF THE MEASURED DATA AND THE DATA PROVIDED BY THE TRANSDUCER MANUFACTURER	109

List of Figures

2.1	The illustration of the sound propagation in a medium. The sound propagation manifests itself as density and pressure variations. The label “C” stands for compression, and “R” stands for rarefaction. (a) density variations (b) pressure variations (c) graphical representation for the density and pressure variations.	8
2.2	The block diagram illustrating the processing steps required to construct the medical ultrasound image.	11
3.1	The ultrasound research scanner, Digital Phased Array System (DiPhAS), used in the measurements for ultrasound data acquisition.	12
3.2	Electrical pulse width modulated (PWM) drive signals. The PWM signals for (a) 2-cycle pulse, (b) 1.5-cycle pulse (c) 1-cycle pulse. (d) 0.5-cycle pulse. $v_{TX}(t)$ is the voltage amplitude of the transmit waveform.	14
3.3	Matlab Simulink model used in this study to generate PWM signals.	15
3.4	The phased array transducer used throughout this study. It has 128 elements with 0.1 mm element pitch and operates at 7.5 MHz center frequency. ...	16
3.5	The structure of the ultrasound phantom used in the measurements. The attenuation is 0.5 dB/cm/MHz in the rubber-based tissue-mimicking material, and the sound speed is 1450 m/s at room temperature. The solid rectangles indicate the horizontal pin targets at 40 mm depth and the vertical pin targets. The parallel-hatched rectangle indicates the speckle region, which is a target free region. The dashed rectangle indicates the anechoic cysts with different diameters.	17
3.6	Experimental setup for phantom measurements. The setup consists of DiPhAS integrated with a personal computer, a phantom, a phased array transducer positioned on top of the phantom surface, and a holder for fixing the transducer array position.	17

3.7	The principle of focusing in transmission. The time delays applied to each signal at each transducer array element are adjusted such that the transmitted signals arrive at the focal point simultaneously.	20
3.8	The principle of beam steering in transmission. The time delays applied to each signal at each transducer array element are adjusted such that the wavefront is steered through a desired direction.	22
3.9	The principle of focusing and beam steering in reception. The time delays applied to each signal at each transducer array element are adjusted based on the distance between the field point and the respective transducer element.	23
3.10	The principle of generating a diverging wavefront in the propagating medium in transmission. The time delays applied to each signal at each transducer array element are adjusted such that a diverging wavefront is formed in the propagating medium.	24
4.1	The geometry used in simulations to derive analytical expression. Δx is the element pitch. D is the total aperture length. θ is the angle between the array surface and the r . r_i is the distance from i th element to the field point.....	29
4.2	Simulation result in a non-attenuating medium. 2-cycle pulse is transmitted from all transducer array elements. (a) The pressure for focused, PW, and DW transmissions when $\theta = 90^\circ$ and $r = 4$ cm. (b) The maximum pressure values for focused, PW, and DW transmissions at different depths when $\theta = 90^\circ$	31
4.3:	Simulation result for the total pressure at the field point for focused, PW, and DW transmissions when $\theta = 80^\circ$ and $r = 4$ cm in a non-attenuating medium. 2-cycle pulse is transmitted from all transducer array elements.	32
4.4	Simulation result for the total pressure at the field point for focused, PW, and DW transmissions when $\theta = 60^\circ$ and $r = 4$ cm in a non-attenuating medium. 2-cycle pulse is transmitted from all transducer array elements.	33

4.5	Simulation result for the total pressure at the field point for DW transmission when $\theta = 60^\circ$ and $r = 4$ cm in an attenuating medium. 2-cycle pulse is transmitted from all transducer array elements.	34
4.6	Simulated cyst phantom ultrasound image obtained by using DW data. Field II simulation program is used. The blue arrows show the point targets. The red arrows show the artifacts. Color bar is in dB scale.	36
4.7	Beamformed signal along the center line of the simulated image. The blue arrows show the echoes coming from the point targets. The red arrows show the artifacts in the beamformed signal.....	37
5.1	The 8-chip CGS coded signals with different chip lengths used in the measurements. (a) CGS(A) coded signal with 0.5 cycle/chip. (b) CGS(B) coded signal with 0.5 cycle/chip. (c) CGS(A) coded signal with 1 cycle/chip. (d) CGS(B) coded signal with 1 cycle/chip. (e) CGS(A) coded signal with 1.5 cycle/chip. (f) CGS(B) coded signal with 1.5 cycle/chip. (g) CGS(A) coded signal with 2 cycle/chip. (h) CGS(B) coded signal with 2 cycle/chip.	43
5.2	The 2-cycle/chip CGS coded signals with different code lengths used in the measurements. (a) CGS(A) coded signal with 2 chips. (b) CGS(B) coded signal with 2 chips. (c) CGS(A) coded signal with 4 chips. (d) CGS(B) coded signal with 4 chips. (e) CGS(A) coded signal with 8 chips. (f) CGS(B) coded signal with 8 chips. (g) CGS(A) coded signal with 10 chips. (h) CGS(B) coded signal with 10 chips. Each chip is 2-cycle long (2-cycles/chip).....	44
5.3	The illustration of the complementarity property by using 8-chip long CGSs with 2-cycle/chip. (a) Autocorrelation of the CGS(A) coded signal. (b) Autocorrelation of the CGS(B) coded signal. (c) The sum of the autocorrelations.	45
5.4	Summation of the aperiodic autocorrelations of CGS(A) and CGS(B) coded signals under MSK modulation. The amplitude is normalized with respect to its maximum.....	47

5.5	Transmitter configuration for coded DWI. CGS(A) is a Golay sequence, and CGS(B) is its complementary sequence. The transducer elements are driven by CGS(A) and CGS(B) coded signals successively. Appropriate time delays are applied to each array element to form a diverging wavefront..	48
5.6	Receiver configuration for coded DWI. The same transducer is used for both transmission and reception. A matched filtering is applied to received data. The resulting MF output is beamformed and post-processed to construct the ultrasound image.	49
6.1	The freshwater measurement setup. The steel plate is immersed in the water at 5 cm depth and the transducer is positioned over the steel plate. The size of the water tank is $50 \times 20 \times 30$ cm (length, width and depth).....	52
6.2	The signals reflected from the thick steel plate and received by the 64th element of the phased array transducer. 8-chip CGS(A) coded received signal with (a) 0.5-cycle/chip, (b) 1-cycle/chip, (c) 1.5-cycle/chip, (d) 2-cycle/chip. The amplitude unit in this work is in terms of LSB of DiPhAS acquisition system.	53
6.3	The signals reflected from the thick steel plate and received by the 64th element of the phased array transducer. 2-cycle/chip CGS(A) coded received signal with (a) 2 chips, (b) 4 chips, (c) 8 chips, (d) 10 chips. The amplitude unit in this work is in terms of LSB of DiPhAS acquisition system.	54
6.4	Received signals on the 64th element of the phased array transducer after attenuation compensation. All signal energy is fixed at $8 \text{ LSB}^2\text{-s}$. 8-chip CGS(A) coded received signal with (a) 0.5-cycle/chip, (b) 1-cycle/chip, (c) 1.5-cycle/chip, (d) 2-cycle/chip. The bit transitions and phase transition instants are marked for convenience. Every row within each figure corresponds to adaptive attenuation compensation with respect to depths of 0.5, 1.5, 2.5, and 4.5 cm (return path length of 1, 3, 5, and 9 cm), respectively.....	56

- 6.5 Received signals on the 64th element of the phased array transducer after attenuation compensation. The signal energies are 1, 2, 4, and 8 LSB²-s, respectively for pulsed signal and 2, 4, and 8-chip coded signals. (a) 1-chip pulsed signal with 2-cycle/chip (b) 2-chip CGS(B) coded signal with 2-cycle/ chip. (c) 4-chip CGS(B) coded signal with 2-cycle/ chip, (d) 8-chip CGS(B) coded signal with 2-cycle/ chip. Every row within each figure corresponds to adaptive attenuation compensation with respect to depths of 0.5, 1.5, 2.5, and 4.5 cm (return path length of 1, 3, 5, and 9 cm), respectively..... 58
- 7.1 The geometry used to derive a phase profile for a particular DW. For a given aperture, the virtual source distance, r_v determines the geometrical divergence sector. φ is the geometrical divergence sector angle. The time delays applied to each array element is calculated for the geometrical beamwidth of φ . Insonification sector is wider than the geometrical divergence sector due to the diffraction. The arc in speckle region is also shown along which SNR is measured to determine the appropriate virtual source distance, and the required beamwidth..... 61
- 7.2 Noise amplitude for coded DWI (8 chips and $r_v = 10.5$ mm) with 4 different chip lengths. The noise amplitude variation with respect to depth is same for all chip lengths. This graph also shows the noise level in CSFI-GF and CSFI-MF. Note that the noise analysis for coded DWI (implemented with MF), CSFI-GF, and CSFI-MF have different gains. The average noise power is measured over independently taken 13 measurements without any transmission. The received noise amplitude is plotted in dB//LSB. The arrow shows the 12 dB increase in noise between MFs of CSFI and DWI. 62
- 7.3 Noise amplitude for coded DWI (2, 4, 8 and 10 chips with 2-cycle/chip) with 4 different code lengths. This graph also shows the noise level in CSFI-GF and DWI with pulsed transmission (1-chip). Note that the noise analysis for coded DWI (implemented with MF), and CSFI-GF have different gains. The

	average noise power is measured over independently taken 13 measurements without any transmission. The received noise amplitude is plotted in dB//LSB. The arrow shows the 3 dB increase in noise when the code length doubles.	63
7.4	SNR of 8-bit coded DWI with 1-cycle/chip along the arcs at 20, 25, 40, and 50 mm ranges when r_v is 10.5 mm. The arcs constitute equidistant imaging points at which the attenuation remains same. The mean SNR values are also plotted with dashed lines where the measurement variance is relatively high.	65
8.1	SNR ₊₁ measurement results in speckle region for 2, 4, 8 and 10-chip coded DWI with 2-cycle/chip. This graph also shows the measurement results for pulsed DWI (1 chip with 2-cycle/chip) and CSFI techniques. 6-dB reference is also plotted with dotted line for penetration depth analysis.	67
8.2	SNR for CSFI and coded DWI (8 chips and $r_v = 14$ mm). CSFI-MF is shown for comparison. (a) SNR for horizontally spaced pin targets at 40 mm depth (b) SNR for vertically spaced pin targets.	69
8.3	CNR for anechoic cyst with 4 mm diameter positioned at 40 mm depth. White circles show the regions where CNR calculations are made. (a) CNR variation against evaluation region size for CSFI-GF and coded DWI. The dashed circle represents the region where the CNR calculation is reliable. The CNR for one frame of the coded DWI varies between 1.05 and 2.04, with 1.6 mean and 0.3 standard deviation. CNR obtained in CSFI image is 2.3. The cyst images obtained by (b) CSFI-GF. (c) Coded DWI when the transducer is at median position.	71
9.1	SNR ₊₁ measurement results in speckle region for (a) coded DW transmission (8 chips and $r_v = 10.5$ mm) with 4 different chip lengths and for (b) pulsed DW transmission (1 chip and $r_v = 10.5$ mm) with 4 different pulse lengths. SNR + 1 for 1-cycle/chip coded signal is also shown for reference. Speckle amplitude is measured over 11 different measurements	

	each yielding statistically independent data. 6-dB reference is also plotted with dotted line for penetration depth analysis.	74
9.2	The reflected signals with 0.5, 1, 1.5, and 2 cycles from the steel plate in freshwater and received by the 64th element of the phased array transducer.	75
9.3	The SNR_{+1} for coded DWI (8 chips and $r_v = 10.5$ mm) with 4 different chip lengths. (a) SNR_{+1} along the line of horizontal pin targets positioned at 40 mm depth. The SNR_{+1} along the horizontal direction in speckle region is also plotted on the same graph to make a comparison for speckle level variation. (b) SNR_{+1} along the line of vertical pin targets.	77
10.1	Speckle region SNR_{+1} measurement results for CSFI-GF, CSFI-MF and coded DWI (8 chips and $r_v = 10.5$ mm). The maximum SNR is available in the vicinity of the focal region when CSFI-MF is used. In the nonfocal region, the coded DWI offers the highest SNR when attenuation compensation is applied. Note that the coded DWI with compensation offers higher SNR than the uncompensated case, while the results are similar at closer range. A 6-dB reference is plotted with a dotted line for penetration depth analysis.	79
10.2	SNR for CSFI and coded DWI (8 chips and $r_v = 10.5$ mm). CSFI-GF and CSFI-MF are shown for comparison. (a) SNR for horizontal pin targets at 40 mm depth (b) SNR for vertical pin targets.	81
10.3	SSR of CSFI-GF, CSFI-MF, and coded DWI (8 chips, 1-cycle/chip, and $r_v = 10.5$ mm) along the vertical line of pin targets.	82
11.1	Ultrasound images of the anechoic cyst targets. A dynamic range of normalized image intensity values are from 0 to -45 dB. (a) The photo of the measurement setup. (b) CSFI-GF image constructed by 181 focused transmissions. (b) 1-cycle/chip coded DWI image. (c) 2-cycle/chip coded DWI image. Coded DWI images are constructed by using two transmissions (acquired in 200 μ s) and attenuation compensation.	87

C.1	The transmit and receive diagram of the phased array transducer used in this study.....	108
C.2	Fresh-water measurement result. Only the 64th element of the transducer array is fired. 0.5-cycle pulse is transmitted. All the elements receive the echo signal. (a) Received signal at the 64th element, $s_{RX}(t)$. (b) The frequency spectrum of this received signal, $S_{RX}(f)$	110
C.3	The measured two-way transfer function of the 64th element of the phased array transducer used in the measurements.	110
C.4	The data provided by the manufacturer of the phased array transducer (courtesy: Fraunhofer IBMT). The parameters and respective values at the bottom part of the figure can be clearly seen if this figure is enlarged. ..	111

List of Tables

5.1	Bipolar Representation of 2, 4, 8 and 10-chips CGS(A). These sequences are used to code the transmitted signals in coded DWI.	42
5.2	Bipolar Representation of 2, 4, 8 and 10-chips CGS(B). These sequences are used to code the transmitted signals in coded DWI.	42

Chapter 1

Introduction

1.1 Literature Review

Ultrasound imaging uses high-frequency sound waves to visualize tissues, organs, and other body structures. Ultrasound imaging is an easily accessible, noninvasive, and nonionizing modality [1]. Recently, there has been an interest in using ultrafast imaging techniques to observe the transient and rapid physiologic events in human tissue and evaluate tissue functions beyond anatomical information [1], [39]. Myocardial stiffness and motion imaging, blood flow imaging, assessing the contraction/relaxation periods of the heart cycle, shear wave imaging, and assessing the viscoelastic properties of the tissue are some applications in ultrafast imaging. In these applications, a frame rate in the order of thousands of frames per second is required, which is much larger than the frame rates of conventional imaging techniques [1].

In conventional ultrasound imaging, short-duration bursts of sinusoidal signals are utilized to improve the range resolution. The energy of such signals is proportional to their duration, and the signal-to-noise ratio (SNR) is reduced for high resolution [2]. Longer duration bursts with higher transmitted energy would increase the SNR at the cost of high resolution. However, the burst duration is limited due to regulations relating to patient safety. Both the resolution and SNR are valuable for medical ultrasound imaging to obtain accurate and high-quality ultrasound images.

The attenuation in the medium distorts the ultrasonic signals and reduces the signal intensity. The attenuation increases as the ultrasound waves propagate through the medium resulting in SNR degradation [3]. Furthermore, the ultrasonic signals undergo several scattering events in the medium, known as multiple-scattering, before reaching the transducer array [4]. It causes signal interference in the sound field and distorts the spatial coherence of the transmitted signals in the field, which also causes SNR degradation.

Since SNR is crucial for ultrasound image quality, several techniques have proposed in literature to increase the SNR. The focused imaging techniques offer higher SNR in the focal region than the unfocused imaging techniques. The conventional ultrasound imaging techniques using phased arrays employ focused and steered beam transmissions for every image line [1]. This implies that several transmission and reception events are required to form an ultrasound image (typically 180 transmissions for a 90° imaging sector), which causes decrease in frame rate. Therefore, limitations arise in fast ultrasound imaging applications where fast phenomena are needed to be observed [1]. In conventional focused imaging techniques, the transmitted signals from the transducer array elements are superimposed constructively in the focal region. The SNR improves in the focal region as the transmitted signal duration increases. On the other hand, the transmitted signals are added destructively outside the focal region, which causes SNR degradation.

To increase the frame rate, ultrafast imaging using unfocused beam transmissions has been proposed to compensate for the poor temporal resolution of conventional focused imaging techniques. In recent years, diverging wave imaging (DWI) has become a prominent imaging technique due to its high temporal resolution. However, DWI, an unfocused imaging technique, suffers from the low SNR. It employs the transmission of diverging wavefronts by a virtual source positioned behind the transducer array [16]. It allows a broader region insonification with a single transmission, and thus the frame rate is

considerably increased. The transmitted signals add up destructively in the field due to the unmatched phases [5-12], limiting the SNR and penetration depth in DWI [1]. This effect is aggravated when the DWs propagate in a multiple-scattering and diffracting medium. Because the medium also causes the ultrasound beam to diverge and produces interference in the sound field [4], [13], [14]. Furthermore, when the beamwidth in DWI is determined using only geometric considerations, a significantly larger insonified sector emerges due to multiple scattering and diffraction, which causes a waste of available energy.

The use of several steered DWs with the coherent spatial compounding technique increases the SNR and penetration depth [15-17]. However, this method is susceptible to motion artifacts, and the number of the compounded waves must be limited [17]. The motion compensation integrated with the compounding technique further improves the SNR and penetration depth [18].

Coded excitation also increases the SNR and penetration depth. The first application of coded transmission for medical ultrasound imaging is introduced in [19]. Encoding with chirp signals [20-23], Barker codes [24], m-sequences [25], [26], and complementary Golay sequences (CGSs) [27], [28] have been studied. Some researchers used both chirp signals and CGSs to make a performance comparison [2], [3], [29-32]. Only CGSs provide range lobe cancellation among all coding sequences. However, they require two successive transmissions and reduce the frame rate to half [31]. Using CGSs and orthogonal CGSs with DW transmission enables SNR improvement compared to uncoded DW transmission [33-35]. The studies on coded excitation employ different chip lengths such as half [32], one [24], [28], [32], [34], one and a half [33], [35], two [3], [27], [29], [30], [31], and five-cycle/chip [2]. The other studies reviewed in this work have no relevant data on chip length [25], [26].

In addition to the coding sequences, another approach to obtain coding is to use matrix-based coding techniques. Hadamard coding, [36], [37] its extended versions [38-40], and S-sequence coding [41] techniques benefit from the matrix-based coding. The experimental results show that encoding with matrices also improves the SNR and penetration depth.

The attenuation in the tissue impairs the performance of coded signals in medical ultrasonic imaging. The correlation between the received signal and the reference signal deteriorates at the deeper imaging regions. The attenuation compensation with various compression filters [42] or a frequency downshift estimator [43] for coded transmission offers SNR improvement.

In this respect, we investigated the effect of the chip signal duration on SNR experimentally in a multiple-scattering, attenuating and diffracting medium [44]. We obtained the maximum SNR at the longer distance when the chip signal duration is short enough to correspond to the transducer bandwidth. SNR deteriorates when the signal duration increases. We also determine the required beamwidth in coded DWI, which adequately confines the ultrasound beam energy into the sector to be imaged. Using this optimized beamwidth contributes to SNR maximization. We compared the SNR of optimized coded DWI to that of the conventional single-focused phased array imaging (CSFI) [45], [46].

1.2 Organization of this Thesis

The rest of this thesis is organized as follows. In chapter 2, we describe the fundamental concepts of medical ultrasound imaging. In chapter 3, we present the methods and materials used in this study. We present the imaging techniques used in this study together with the respective transmission and reception beamforming methods. In chapter 4, we investigate the pressure field in DWI by using a simulation-based approach to understand the propagation in weakly and multiple scattering, attenuating, and diffracting media. In chapter 5, we discuss the coded

transmission and coding sequences in DWI. Chapter 6 describes the construction of the reference signals used in the receiver and the compensation of the reference signals for the frequency-dependent attenuation. Chapter 7 gives the optimization of the DW profile for a given field of view and the experimental results. In Chapter 8 and Chapter 9, we experimentally evaluate the effects of code length and chip signal duration on SNR, respectively. Chapter 10 presents the performance comparison of the optimized coded DWI and CSFI in terms of SNR and signal-to-speckle ratio (SSR). We experimentally show the significance of the attenuation compensation. Finally, we give the discussions and concluding remarks in Chapter 11 and Chapter 12, respectively.

Appendix A presents the guidelines and measurement protocols used for data acquisition during the measurements. Appendix B of this thesis includes the analytical derivation of the equations used in the simulation. Appendix C presents the characterization of the phased array transducer used in the measurements.

Chapter 2

Medical Ultrasound Imaging

Ultrasound imaging differs from other medical imaging modalities because it uses the local acoustic properties of the medium to form the ultrasound image [47]. The imaging equipment, including an ultrasound scanner and transducer array, is used to perform a pulse-echo measurement. The ultrasound signals are transmitted through the medium. The reflected signals are received and post-processed to form the ultrasound images, which are subjected to distortion caused by various sources. Over the years, the researchers have addressed the technical challenges of ultrasound imaging, and the imaging equipment technology has been developed. Consequently, the use of medical ultrasound imaging has expanded.

However, there are still problems to be resolved in medical ultrasound. In this respect, it is essential to understand the fundamentals of medical ultrasound imaging, which is detailed in this chapter. This chapter describes the principles of medical ultrasound imaging, physical sound characteristics, sound propagation, and imaging arrays. The final section describes the post-processing steps for constructing the medical ultrasound images.

2.1 Principles of Medical Ultrasound Imaging

Medical imaging aims to visualize the internal structure of the human body and provide a correct diagnosis and personalized approach to patient treatment [48]. Medical imaging refers to different imaging techniques, such as X-ray radiography, magnetic resonance imaging, and ultrasound imaging.

Medical ultrasound imaging is the safest and most cost-effective modality among all imaging modalities. [49]. It relies on the pulse-echo approach, and the ultrasound images are created by using the acoustic impedance difference within the region of interest [47]. The ultrasound waves partially reflect when they encounter an interface in tissue with two different acoustic impedances. For example, the interface between soft tissue and a bone produces relatively strong echoes due to the significant acoustic impedance difference compared to the interface between two soft tissues [50]. The transducer array receives partial reflections (or echoes), and these reflections are subsequently processed to form an image. Sweeping the direction of the transmitted beam builds up the scan and provides the entire ultrasound image.

SNR, SSR, contrast-to-noise ratio (CNR), temporal resolution, range resolution, and lateral resolution are crucial in medical ultrasound imaging. The trade-offs between these factors determine the ultrasound imaging effectiveness. Another crucial factor is patient safety [51]. It refers to protecting the patient from harmful side effects or injuries caused due to the mechanical or thermal effects produced during the ultrasound examination. Therefore, medical ultrasound imaging is strongly limited by the spatial peak pulse average intensity (I_{sppa}) and spatial peak temporal average intensity (I_{spta}) to ensure patient safety. I_{sppa} is the average value of the ultrasound pulse, where the maximum ultrasound intensity occurs. The maximum intensity generally occurs at the focal point of the transducer. I_{spta} is the largest value of time-averaged intensity at the focal depth. It also measures how often the largest intensity should be applied to the patient.

2.2 Physical Sound Characteristics

A wave is regarded as a movement of a disturbance from one point to another. The sound waves are mechanical longitudinal waves that require a material medium to propagate with a finite speed. The direction of sound propagation is parallel to the direction of the disturbance. Sound waves alternately produce compression and rarefaction (decompression) as they propagate through the medium [13].

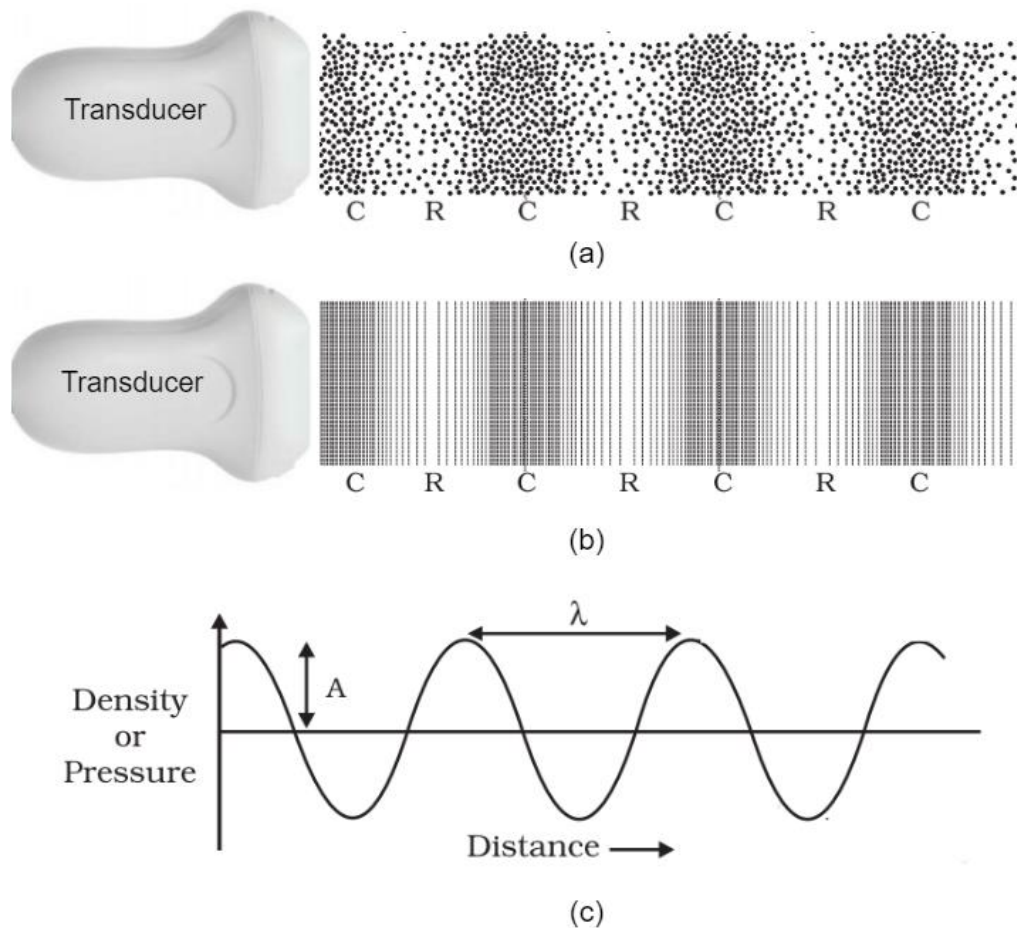


Figure 2.1: The illustration of the sound propagation in a medium. The sound propagation manifests itself as density and pressure variations. The label “C” stands for compression, and “R” stands for rarefaction. (a) density variations (b) pressure variations (c) graphical representation for the density and pressure variations.

When a transducer moves forward, it pushes and compresses the medium in front of it, creating a high-pressure region. This region is called a compression region. When a transducer moves backward, it creates a low-pressure region called the rarefaction region. As the transducer moves back and forth rapidly, a series of compression and rarefaction regions are created in the medium, which results in sound wave propagation through the medium.

Figure 2.1 shows the density and pressure variations as a sound wave propagates through the medium. The particles come closer in compression regions. On the contrary, the particles are furthest apart in the rarefaction regions. These regions are shown in Figure 2.1(a) and Figure 2.1(b) as density and pressure variations. The compression and rarefaction regions are marked with “C” and “R” in Figure 2.1, respectively. Note that “C” stands for compression and “R” stands for rarefaction. In compression regions, the density and pressure are higher than those in rarefaction regions, as shown in Figure 2.1(c). Also, the wavelength of the sound wave represented as λ is shown in Figure 2.1(c), where the wavelength is the distance between two consecutive compression regions or two rarefaction regions.

The sound classification depends on the frequency and wavelength, which are inversely proportional. The ultrasound frequencies exceed the upper limit (20 kHz) of audible human hearing [52]. In medical ultrasound imaging, the ultrasonic waves at several MHz are utilized. The selection of proper ultrasound frequency or wavelength is critical in medical ultrasound imaging. High-frequency (or small wavelength) waves enable high-resolution images, which are more attenuated than lower frequency waves. Increased attenuation causes a decrease in SNR and SNR-related performance, such as penetration depth. The tradeoff between the resolution and penetration depth determines the frequency selection. For example, high-frequency waves can be transmitted to obtain a high-resolution image of superficial tissue structures. On the other hand, lower frequency waves can be transmitted to monitor the deeper tissue regions at the expense of resolution.

In conventional clinical medical ultrasound systems, short-duration bursts of sinusoidal signals are used to improve axial resolution. The energy of such signals is approximately proportional to their duration, and SNR is reduced for increased resolution. Longer duration bursts would be employed to increase the SNR at the cost of resolution.

2.3 Post-Processing Steps for Image Construction

Many steps are required to collect and process the raw data to construct the ultrasound image. Figure 2.2 illustrates these steps performed by a commercial clinical ultrasound scanner [53].

The transmit beamformer adjusts the driving phases for each transmit signal at each transducer array element. The time delays are applied to each array element in transmit beamformer to obtain a required wave profile. The transmit beamforming allows achieving the desired transmission scheme. The resulting signals are transmitted from the transducer array. The same transducer array receives the reflected signals coming from the medium.

Post-processing steps are then applied to the received data to construct the ultrasound image. First, the received signals at each transducer array element are processed into a single image line in receive beamformer. Receive beamforming is obtained by considering the geometrical distance from the transmitting element to the field point and back to the receiving element. Appropriate phase sets (or time delays) are applied on received signals at each transducer array element to compensate for the differences in the arrival time, assuming a constant speed of sound through the imaging medium.

The ultrasound waves lose energy as they propagate through the medium due to the attenuation and defocusing effects. Consequently, the reflections from deeper tissue regions appear weaker in the data. Compensation is then applied to

the beamformed data to compensate for this effect. This compensation is called time gain compensation (TGC). The image scan lines are then filtered to reduce the noise outside the transmit frequency range. The resulting filtered image scan lines are then envelope detected.

Log compression is applied after envelope detection to adjust the dynamic range of the processed scan lines. Log compression is required in ultrasound systems since the dynamic range of the scan lines generally exceeds the grayscale range that can be displayed by a computer screen or visually perceived.

Finally, scan conversion is used to make the image suitable for display on the computer screen. Scan conversion is a signal processing technique in an ultrasound system, and it is responsible for translating input data captured in specified coordinates to cartesian coordinates [54]. The scan conversion uses interpolation between neighboring pixels to generate an interpolated pixel.

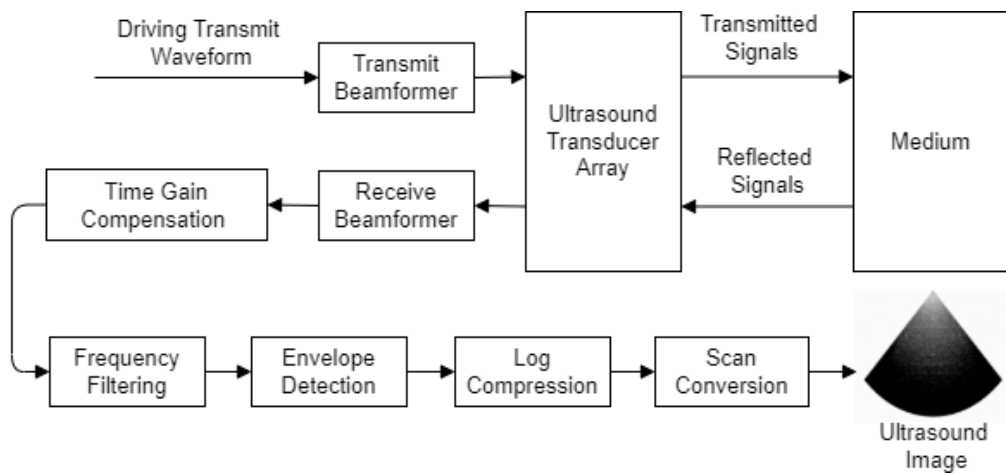


Figure 2.2: The block diagram illustrating the processing steps required to construct the medical ultrasound image.

Chapter 3

Methods & Materials

3.1 Measurement Setup

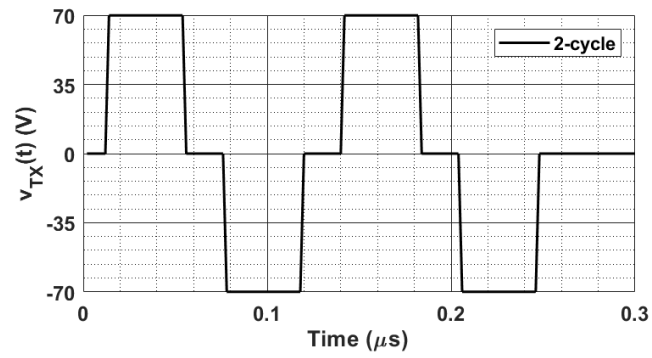
In this study, we collected the experimental data using an ultrasound research scanner; Digital Phased Array System (DiPhAS, Fraunhofer IBMT, Frankfurt, Germany). The DiPhAS components are shown in Figure 3.1. This system is designed for our research group by Fraunhofer IBMT. It has 256 dedicated channels for reception and transmission of ultrasound signals from 1 MHz to 20 MHz mid-frequency transmit range. It allows the transmission of customized signals. We sampled the recorded raw data at 80 MHz.



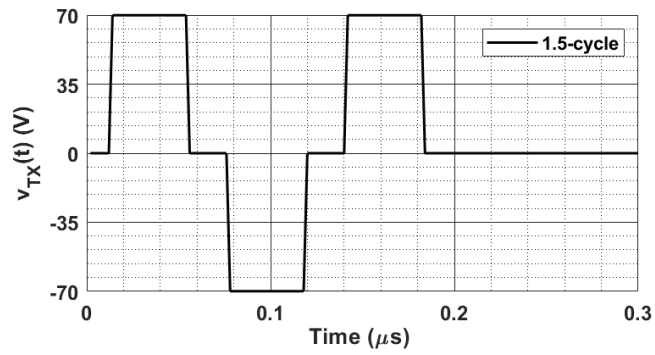
Figure 3.1: The ultrasound research scanner, Digital Phased Array System (DiPhAS), used in the measurements for ultrasound data acquisition.

DiPhAS driver output stages can provide output pulses at a 480 MHz symbol rate. Pulses can have 3-level output voltage, 0 and $\pm V_m$, where V_m is the excitation voltage and can be chosen between 5 V and 75 V. We used 70 V amplitude. It results in amplitude of +70 V and -70 V. The peak-to-peak voltage is 140 V.

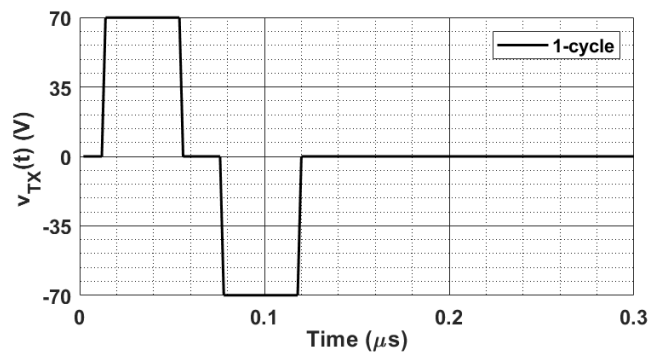
DiPhAS recommends the pulse width modulated (PWM) signals depicted in Figure 3.2, which shows the electrical PWM signals of 2-cycle, 1.5-cycle, 1-cycle, and 0.5-cycle pulses, respectively. These signals are suitable to generate the chip signal for coded transmission. The sampling interval at transmission is 2.083 ns, which corresponds to a 480 MHz sampling rate. Each half-period pulse contains 12.5 ns 0 V level at the beginning and end of the half-cycle and 41.7 ns of 70 V amplitude. We obtained the insonification signals with the widest bandwidth using the half-cycle signal. It is possible to have a wider spectrum if the pulse duration in Figure 3.2(d) is shortened. In this case, lower energy signals emerge, and the measurements may suffer from noise problems.



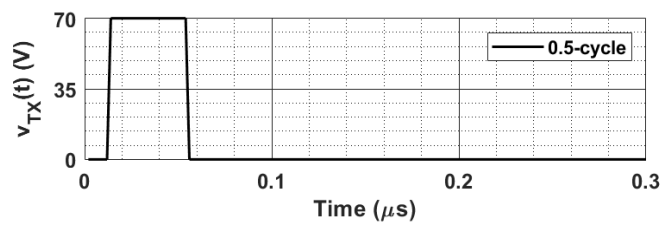
(a)



(b)



(c)



(d)

Figure 3.2: Electrical pulse width modulated (PWM) drive signals. The PWM signals for (a) 2-cycle pulse, (b) 1.5-cycle pulse (c) 1-cycle pulse, (d) 0.5-cycle pulse. $v_{TX}(t)$ is the voltage amplitude of the transmit waveform.

We used MATLAB Simulink for the PWM signal generation process. The model used in MATLAB Simulink to generate PWM signals is shown in Figure 3.3. First, we produce the transmitted signals by using the signal generator module. Then, we converted these signals into PWM signals by using the model. The resulting PWM signals are available in the MATLAB workspace for further use.

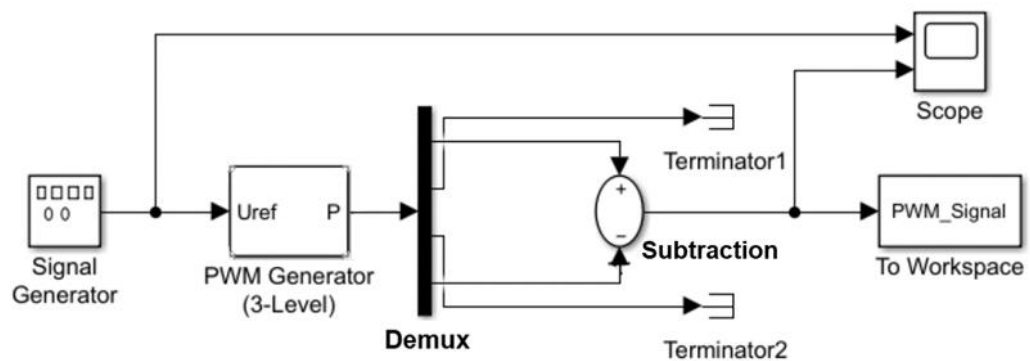


Figure 3.3: Matlab Simulink model used in this study to generate PWM signals.

We used a phased array transducer (Fraunhofer IBMT, Frankfurt, Germany) operating at 7.5 MHz center frequency with a fractional bandwidth of 70%. The transducer used in the measurements is shown in Figure 3.4. This transducer array consists of 128 elements spaced by 0.1 mm element pitch. The same transducer is used for transmission and reception throughout this study.

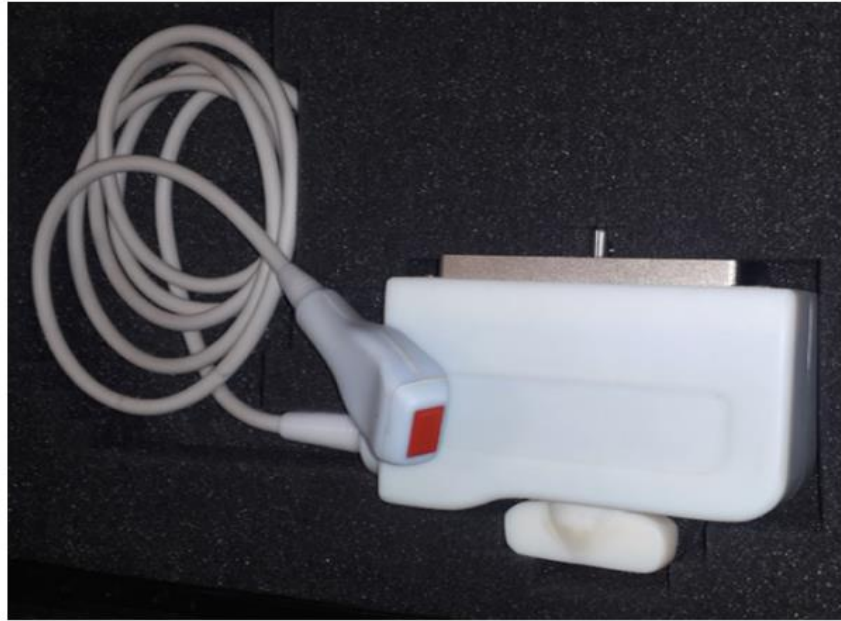


Figure 3.4: The phased array transducer used throughout this study. It has 128 elements with 0.1 mm element pitch and operates at 7.5 MHz center frequency.

The phantom used in this study (Model 550, Breast & Small Parts Phantom, ATS Laboratories, Bridgeport, USA) is designed with monofilament nylon line targets (pin targets) and tissue-mimicking cylindrical targets of varying sizes and contrasts. The structure of this phantom is shown in Figure 3.5. The pin targets have a diameter of $50 \mu\text{m}$ and have very weak reflectivity at 7.5 MHz, where the wavelength is $200 \mu\text{m}$. The phantom is constructed of rubber-based tissue-mimicking material. The sound speed in this material is $1450 \text{ m/s} \pm \%1$, and the attenuation is 0.5 dB/MHz/cm at 23°C . The experimental setup for phantom measurements is illustrated in Figure 3.6. Low viscosity gel is applied between the array and the phantom surface before scanning. We recorded the phantom temperature and the ambient temperature during the measurements.

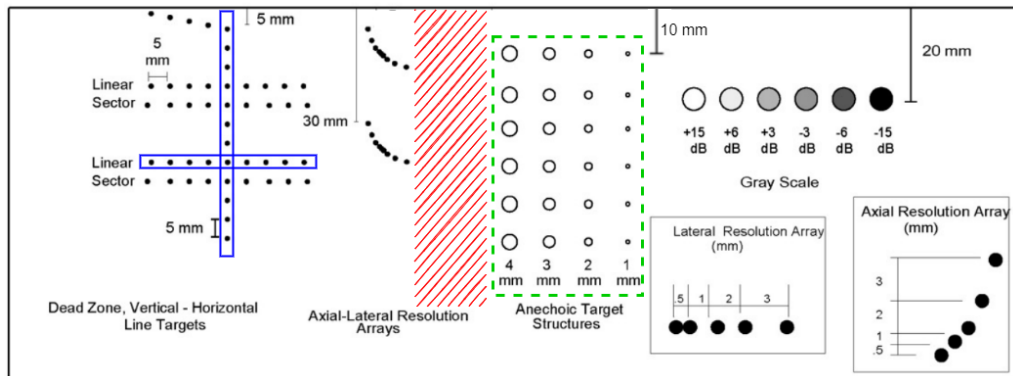


Figure 3.5: The structure of the ultrasound phantom used in the measurements. The attenuation is 0.5 dB/cm/MHz in the rubber-based tissue-mimicking material, and the sound speed is 1450 m/s at room temperature. The solid rectangles indicate the horizontal pin targets at 40 mm depth and the vertical pin targets. The parallel-hatched rectangle indicates the speckle region, which is a target free region. The dashed rectangle indicates the anechoic cysts with different diameters.



Figure 3.6: Experimental setup for phantom measurements. The setup consists of DiPhAS integrated with a personal computer, a phantom, a phased array transducer positioned on top of the phantom surface, and a holder for fixing the transducer array position.

The total dynamic range for programmable gain is 45 dB in DiPhAS. We applied a 22 dB fixed gain to ensure a sufficient noise signal was present at each channel and all delays for reliable noise measurements. We limited the time-varying gain to 2.3 dB/cm to avoid any accidental signal saturation. The reasons

for using a large fixed gain (22 dB) plus 2.3 dB/cm varying gain are explained below.

There are three different types of noise in medical imaging signals. The noises are transducer-originated noise, preamplifier noise, and quantization noise.

The transducer-originated noise is the acoustic noise due to the radiation resistance and mechanical noise due to losses in the transducer. The preamplifier noise is the electronic noise generated in the preamplifier (subsequent amplification stages have minimal noise contribution when the preamplifier gain is large). The quantization noise arises due to the least significant bit (LSB) level at the analog to digital converter (ADC) input. The transducer and preamplifier noise contributions are part of the received signal at the preamplifier output. The SNR degradation caused by these noise contributions cannot be avoided in weak signal situations. However, the limitation caused by quantization noise can be avoided by using sufficient preamplification at all depths. The sum of transducer-originated noise and preamplifier noise levels must be kept well above the quantization noise to measure the received noise at every channel accurately and assess the SNR reliably. We used a 22 dB fixed gain at TGC, which enabled the measurement of transducer and preamplifier noise approximately 6 dB above the quantization noise level at all delays.

TGC other than a sufficient fixed gain level is unimportant in this work. Any level of TGC variation can be implemented in post-processing by software without any loss in generality. SNR will not be affected once there is a sufficient level of fixed gain to secure the transducer and preamplifier noise contribution in measurements. The received signals are noise limited and not quantization noise (level) limited. We used a 2.3 dB/cm variable gain to avoid accidental signal saturation (for 7 cm depth, the maximum variable gain we could use is 3.2 dB/cm after 22 dB fixed gain in DiPhAS).

3.2 Imaging Techniques

This section describes the imaging techniques used in this study and the respective beamforming processes.

3.2.1 Conventional Single-Focused Phased Array Imaging

CSFI technique employs focused and steered beam transmissions to form the image lines [1]. The transmitted signals are coherently superimposed at the focal point. This constructive addition provides images with improved SNR and related performances in the focal zone. Since the transmission is focused at a single point per frame in CSFI, the resulting images suffer from SNR and related performances in the nonfocal regions. The data acquisition time required to construct the entire ultrasound image depends on the number of image lines.

CSFI technique provides high resolution and maximum achievable SNR in the focal region. Therefore, we used the CSFI as a reference imaging technique for SNR comparison in this study.

In CSFI measurements, we transmitted either 1-cycle pulse or 2-cycle-pulse, depending on the comparison with DWI. We used 181 steered and focused beam transmissions to construct the image scan lines sequentially. The steering angle ranges from -45° to 45° with respect to normal and spaced at 0.5° intervals. We focused each transmission at 40 mm distance from the transducer array center. We use all array elements in each transmit and receive event.

We applied receive delay-and-sum beamforming directly on the raw data at each array element to form a scan line along the beam axis. We employed a Gaussian filter (GF) centered at 7.5 MHz to reduce the out-of-band noise and interference components of the beamformed signal. The frequency spectrum of the GF is given by [47]:

$$H_{GF}(\omega) = \frac{\sqrt{2\pi}}{\sigma_\omega} e^{-\frac{j\omega}{c_0}} e^{-\frac{(\omega-\omega_c)^2}{2\sigma_\omega^2}}, \quad (3.1)$$

where c_0 is 1450 m/s, ω_c is the center angular frequency, and $\sigma_\omega/(0.425\omega_c)$ is the -6 dB fractional bandwidth of the GF. The fractional bandwidth is 63% when σ_ω is 1.25×10^7 . We normalized the amplitude of the frequency spectrum to unit amplitude. We then constructed the images by calculating the 20 log of the envelope information [55] and using scan conversion. This imaging technique is referred to as CSFI-GF in this thesis from now on.

Applying matched filtering to CSFI is expected to increase the SNR further in the focal region. Therefore, we also implemented CSFI with a matched filter (MF) to compare with coded DWI, although this method is not employed in practice. We referred to this scheme as CSFI-MF in this study. The MF implementation in CSFI is exactly similar to the implementation used in coded DWI.

3.2.2 Beamforming in Transmission and Reception in Conventional Single-Focused Phased Array Imaging

The beam focusing and steering can be obtained by applying appropriate time delays to array elements. The principle of transmit beam focusing is illustrated in Figure 3.7 using a 5-element transducer array for simplicity.

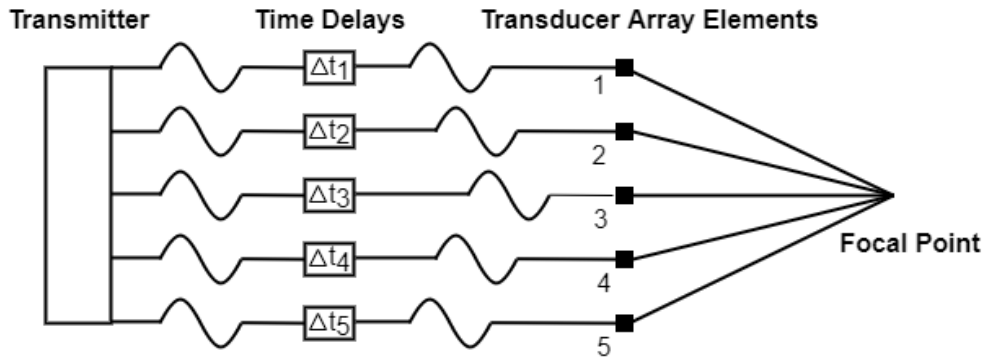


Figure 3.7: The principle of focusing in transmission. The time delays applied to each signal at each transducer array element are adjusted such that the transmitted signals arrive at the focal point simultaneously.

The time required for a sound wave to propagate from each element to the focal point depends on the distance from the element to the focal point and the sound propagation speed. The distance from element 1 to the focal point is larger than that for element 3. Therefore, the propagation time for the ultrasound wave to travel from element 1 to the focal point is larger than that for element 3. Due to the symmetry in Figure 3.7, the propagation time from element 1 to the focal point is equal to that for element 5. Suppose an appropriate time delay is assigned to each array element such that the transmitted signals arrive at the point of interest simultaneously. In that case, the signals are coherently summed up at that point of interest. For an N -element transducer array, the time delay required for the i th transducer element to achieve transmit-focusing can be obtained by [47],

$$\tau_i = \frac{1}{c_0} \left[\sqrt{R_f^2 + \frac{(N-1)^2 d^2}{4}} - \sqrt{R_f^2 + (id)^2} \right] \quad (3.2)$$

where $-(N-1)/2 \leq i \leq (N-1)/2$, R_f is the focal distance in the axial direction, N is the number of the transducer elements and assumed to be odd here for convenience, c_0 is the velocity of sound in the region of interest and d is the element pitch. It is evident from Eq. (3.2) that the time delay required for transmit-focusing in the absence of steering is 0 for the two outermost elements and maximum for the central element.

Transmit focusing is limited to a fixed single focal point per excitation, and thus it cannot be changed once transducer elements are excited. Once the data is collected, the focal point can be changed by modifying the time delays for each element to rescan the same image line with a new focal point. Transmit focusing to this new focal point along the propagation direction requires an additional excitation. In this manner, transmit focusing with multiple focal points is achieved, and spatial resolution is improved. However, it requires several transmissions for each image line, causing a decrease in frame rate.

Transmit focusing occurs within the near field of the transducer array and narrows the beam width in the focal region.

The propagation direction of the transmitted beam can be changed to any desired direction by beam steering. The principle of beam steering in the transmission is illustrated in Figure 3.8. The array elements are excited sequentially with a unique time delay. Element 1 is excited first, and element 5 is excited last. The transmitted signals constitute a wavefront, the direction of which is different from the normal of the aperture surface. This wavefront propagates through the medium with a constant steering angle, ϕ_s .

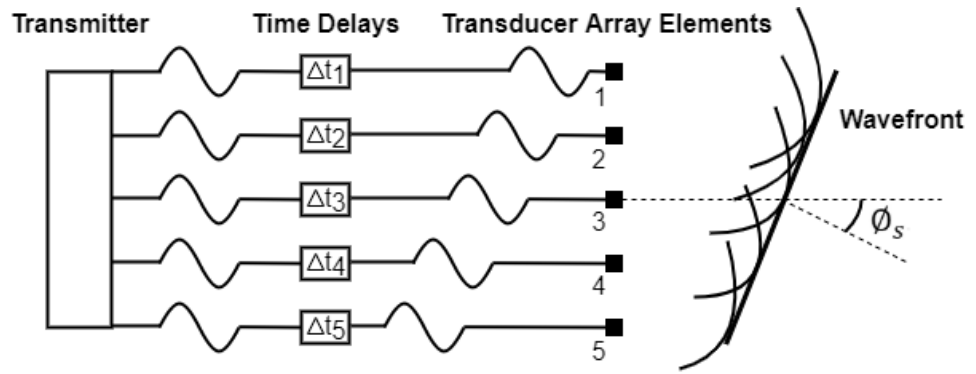


Figure 3.8: The principle of beam steering in transmission. The time delays applied to each signal at each transducer array element are adjusted such that the wavefront is steered through a desired direction.

In the presence of both focusing and steering, the time delays for each element can be calculated by Eq. (3.3) [47]. In Eq. (3.3), the first term accounts for beam steering, the second term accounts for beam focusing, and the third is a constant time delay to ensure that the time delays are positive.

$$\tau_i = \frac{i d \sin(\phi_s)}{c_0} - \frac{(i d)^2 \cos^2(\phi_s)}{2 c_0 R_f} - \tau_0 \quad (3.3)$$

Since transmission and reception are analogous processes, beam focusing and steering can also be achieved in reception. Time delays associated with a single

spatial point of interest can be applied to each array element to synchronize the echoes coming from that point. This process is referred to as receive beamforming.

Figure 3.9 shows the receive beamforming for a point, z_1 . The time delays are applied to each array element to synchronize the signals. Summing up these synchronized signals produces a large amplitude signal if a target exists there. The time delays can be dynamically varied during the data acquisition to focus on a different spatial point. This procedure is referred to as dynamic receive focusing.

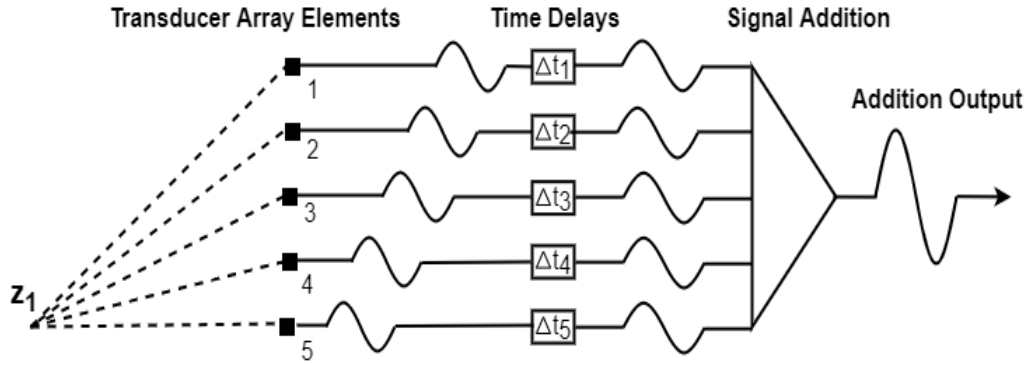


Figure 3.9: The principle of focusing and beam steering in reception. The time delays applied to each signal at each transducer array element are adjusted based on the distance between the field point and the respective transducer element.

3.2.3 Diverging Wave Imaging

We used coded DWI in this study. We coded the transmitted signal using 2, 4, 8, and 10-chips CGSs with a 2-cycle/chip to investigate the code length effect on SNR. We also coded the transmitted signal using 8-chips CGSs with 0.5, 1, 1.5, and 2 cycle/chip to investigate the chip length effect on SNR. The CGSs used for coding are discussed in Sec. V.

The receiver for coded signals incorporates MF at reception. Therefore, we applied matched filtering to the coded DW data. MF is implemented as a correlation receiver, the structure of which is presented in Sec. V.

3.2.4 Beamforming in Transmission and Reception in Diverging Wave Imaging

The time delays are applied to the signals at each transducer element to form a diverging wave in the propagating medium. In the present study, these time delays are calculated by Eq. (3.4), where $T_{TBF,i}$ is the time delay applied to i th transducer element by the transmit beamformer and r_v is the virtual source distance [16].

$$T_{TBF,i} = \frac{1}{c_0} \left[\sqrt{\left\{ \left(i - \frac{N-1}{2} \right) \Delta x \right\}^2 + r_v^2} - r_v \right] \quad (3.4)$$

The principle of forming a diverging wave in the propagating medium is illustrated in Figure 3.10 using a 5-element transducer array for simplicity. The mid-element of the transducer array, Element 3, is excited first, and the outermost elements, Element 1 and Element 5, are excited last, resulting in a diverging wavefront in the propagating medium. The principle of beamforming in reception for DWI is the same as described in Figure 3.9.

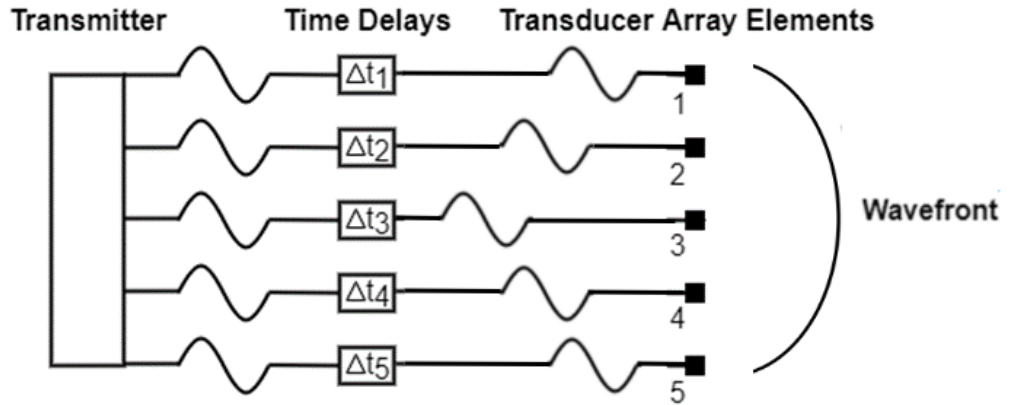


Figure 3.10: The principle of generating a diverging wavefront in the propagating medium in transmission. The time delays applied to each signal at each transducer array element are adjusted such that a diverging wavefront is formed in the propagating medium.

3.3 Signal Energy

The LSB of the ADC in DiPhAS is the amplitude unit in this study, and the squared instantaneous amplitude (LSB²) is the instantaneous signal power. The signal energy over a certain period is proportional to the sum of the squares of instantaneous amplitude over that period multiplied by the receiver sampling interval, Δt , as given in Eq. (3.5). It has units of LSB²-s, and Δt is 12.5 ns in this study. The instantaneous signal amplitude at the i th transducer array element is represented by $y_i(n)$ in this equation.

$$E_i = \Delta t \sum_{q=1}^Q y_i^2(q), \quad (3.5)$$

3.3.1 SNR Measurement

SNR is the ratio of the signal power to noise power and is expressed in dB [56]. However, SNR is regarded as the speckle to noise ratio in medical ultrasound imaging and measured as SNR_{+1} , as given in Eq. (3.6) [57]. Since the received signal already contains noise,

$$SNR_{+1} = 10 \log_{10} \left(\frac{P_{speckle}}{P_n} + 1 \right) \quad (3.6)$$

where $P_{speckle}$ is the speckle power, and P_n is the noise power. The penetration depth is the depth at which SNR_{+1} falls below 6 dB and can be determined from SNR measurements [57]. We carried out signal, speckle, and noise measurements to measure the SNR reliably. The measurement protocols, which explain the procedures step by step, are provided in Appendix A.

3.3.2 Noise Level Estimation Using Noise Measurements

We recorded the received noise in each channel without any transmission. The array was kept acoustically in contact with the phantom surface to ensure the noise contribution of the radiation resistance. We processed each channel noise exactly similar to the way the received signal is processed in the respective imaging technique. We calculated the noise power at every delay (depth) as the average of the squared noise signal amplitude (in units of LSB^2) of independently taken 13 noise measurements.

3.3.3 Speckle Signal Level Estimation Using Speckle Measurements

Ultrasonic wave propagation in inhomogeneous medium gives rise to speckle signal [4]. The signal temporal variation has a random nature due to the random distribution of the inhomogeneities and the multiple-scattering structure of the media. The variance of the speckle signal amplitude can be quite large, but speckle signals can be smoothed by averaging statistically independent signals. The signal temporal variation changes if the signal spectrum changes or the transducer spatial position changes. The frequency spectrum is determined by the signal properties, particularly the duration, which is an optimization parameter in this study.

The speckle region is parallel-hatched in Figure 3.5. We carried out 11 measurements in this region at different transducer positions to have statistically independent speckle data. We moved the transducer array across the phantom surface at approximately 1 mm steps. We collected the speckle data, and we first calculated the speckle power (in LSB^2) at every delay as the square of the amplitudes in each recording. Then, we calculated the average power of 11 recordings. Finally, we calculated the average speckle signal amplitude as the square root of the average power.

Chapter 4

Simulation Results

The DWI provides a broader insonification with a single transmission and a high temporal resolution quantified as high frame rates. Therefore, DWI is commonly used in fast ultrasound imaging applications such as imaging the moving structures and fast transient motions occurring in the tissue. However, SNR and related performances are limited in DWI [1], which are dependent on the spatial coherence of the transmitted signals in the field.

The spatial coherence of the transmitted signals in the field affects the received signal and thus the imaging performance. Therefore, we investigate the transmitted signal coherence of focused and unfocused transmission schemes using a simulation-based approach. In Sec. 4.1, we describe our efforts to investigate the spatial coherence of the transmitted signal in the field and estimate the received signal. In Sec. 4.2, we presented the results of a semi-analytical simulation tool and a Finite Element Analysis (FEA) based simulation tool.

4.1 Pressure Field Simulation

CSFI requires many steered and focused beams, typically 180 transmissions or more, to cover the entire region of interest. This approach provides frame rates of around 25 fps.

By using fast ultrasound imaging techniques, the frame rate can be improved at the expense of resolution and SNR, which are critical for imaging and reliable diagnosis. Increasing the resolution and SNR without sacrificing the frame rate

remains an important practical issue in fast ultrasound applications. The resolution, SNR, and image quality are strongly linked to the spatial coherence of the transmitted beam in the field.

Therefore, it is necessary to investigate the coherence that the signals transmitted from the array elements constitute in the field of interest. In this study, we performed simulations on MATLAB to investigate the coherence of the transmitted signals. The simulation parameters correspond to the experimental parameters. We first derived the analytical expression for the pressure field in a non-attenuating medium generated by an unapodized array of equally spaced point sources. Figure 4.1 shows the geometry used to derive the analytical expression. Instead of spherical spreading, we utilize the cylindrical spreading approach. The pressure field generated by the transducer array at an arbitrary field point with the assumption of cylindrical spreading is expressed by Eq. (4.1), the derivation of which is provided in Appendix B.

$$P_{tot}(r, \theta) = \sum_{i=1}^N \frac{A}{B(r, i)} s(t - C(r, i) + \Delta t_i) \quad (4.1)$$

where i represents the array element index and N is the total number of transducer array elements. $s(t)$ is the transmitted signal in the time domain. Δt_i is the externally applied time delay for element i to achieve the desired transmission scheme, r is the distance from the central element to the field point. θ is the angle between the array surface and the \vec{r} . The term in amplitude, $B(r, i)$, and the term in phase, $C(r, i)$, are given in Eq. (4.2) and Eq.(4.3), where Δx is the element pitch, c_0 is the sound speed, and $n_i = i - 64$ where i ranges from 1 to 128.

$$B(r, i) = \sqrt{r} \left[1 + \frac{1}{4} \left(\frac{n_i \Delta x}{r} \right)^2 - \frac{1}{2} \left(\frac{n_i \Delta x \cos(\theta)}{r} \right) \right] \quad (4.2)$$

$$C(r, i) = \frac{r - n_i \Delta x \cos(\theta)}{c_0} + \frac{(n_i \Delta x)^2}{2 r c_0} \quad (4.3)$$

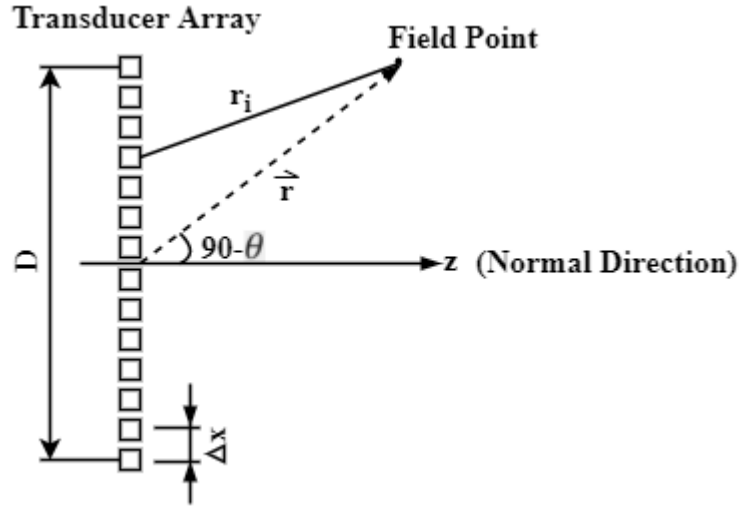


Figure 4.1: The geometry used in simulations to derive analytical expression. Δx is the element pitch. D is the total aperture length. θ is the angle between the array surface and the \vec{r} . r_i is the distance from i th element to the field point.

4.1.1. Simulation Results for Non-Attenuating Medium

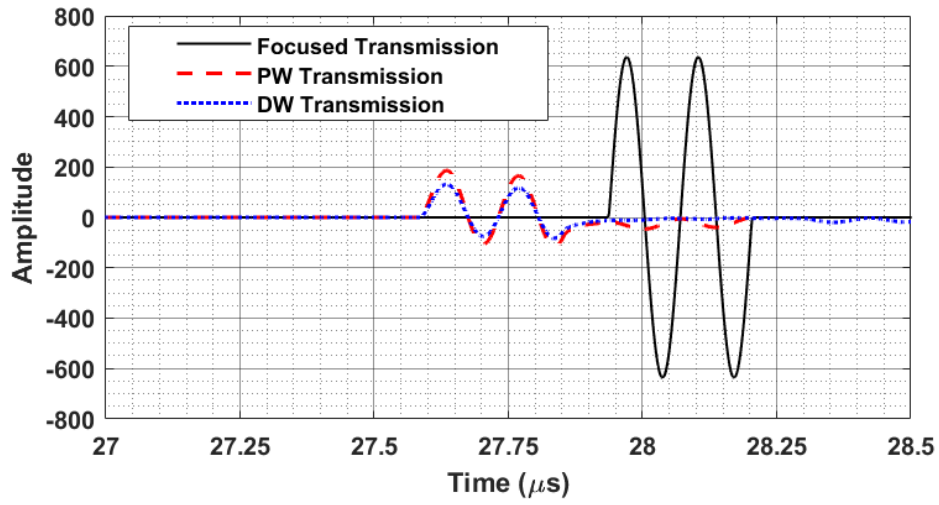
We investigated the pressure signal coherence in the field point for focused, plane wave (PW), and DW transmission schemes. In these schemes, we simulated a single transmission by applying appropriate phases to each simulated array element and examined the resulting pressure signal at an arbitrary field point.

We first examine the pressure signal coherence in the field for focused transmission. The driving phases are adjusted such that the transmission is focused along the normal direction ($\theta = 90^\circ$) at 40 mm away from the array center. The pressure for 2-cycle pulse transmission with 7.5 MHz center frequency generated at the focal point is shown in Figure 4.2(a). Due to the focused transmission, we observed that the transmitted signals are coherently superimposed at the focal point.

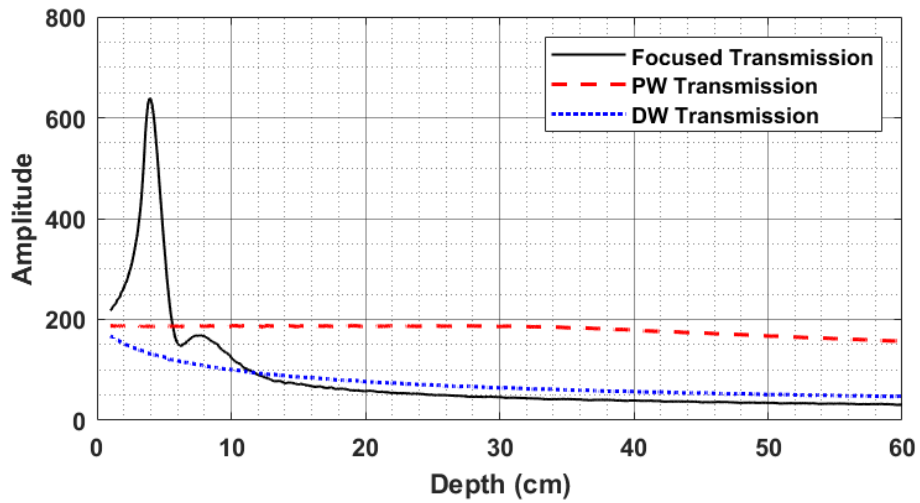
We also investigate the pressure signal coherence in the field by using unfocused transmissions. For this purpose, we used PW and DW transmissions, which are unfocused transmission schemes. For PW transmission, the driving

phases of each element are set to zero, which means that a 2-cycle pulse is transmitted simultaneously from each simulated array element. Figure 4.2(a) also shows the pressure signal for the PW transmission at 4 cm depth along the normal. Due to the unfocused transmission, the transmitted signals cannot be added constructively in the field, and the pressure decreases almost three times compared to focused transmission. Also, we observed that the destructive addition of the transmitted signals causes an expansion in the pressure signal even in the non-attenuating medium. The spatial coherence of the pressure field has become much worse in DW transmission, which is observable in Figure 4.2(a). The destructive addition of the pressure signals in the field point further aggravates. As a result, a decreased pressure amplitude and a further expansion in the pressure signal appear in DW transmission.

The maximum pressure amplitudes obtained along the normal of the transducer array ($\theta = 90^\circ$) at 4 cm for focused, PW, and DW transmissions are plotted as a function of depth in Figure 4.2(b). As expected, the maximum instantaneous pressure occurs at 4 cm depth in focused transmission, which is the transmit focus. The maximum pressure decreases monotonically as getting further from the focal point, where the nonfocal region is established. In PW transmission, the maximum pressure remains the same up to approximately 30 cm depth. Beyond this depth, the maximum pressure decreases monotonically. The maximum pressure amplitude in the nonfocal region for focused transmission is lower than that of the PW transmission. For example, the maximum pressure amplitude for focused transmission at 20 cm depth is one-fourth of the maximum pressure amplitude obtained in PW transmission. On the other hand, the maximum pressure decreases as the depth increases in DW transmission, and it is lower than the pressure of PW transmission at all depths.



(a)



(b)

Figure 4.2: Simulation result in a non-attenuating medium. 2-cycle pulse is transmitted from all transducer array elements. (a) The pressure for focused, PW, and DW transmissions when $\theta = 90^\circ$ and $r = 4$ cm. (b) The maximum pressure values for focused, PW, and DW transmissions at different depths when $\theta = 90^\circ$.

So far, we have discussed the pressure at the field point along the normal direction at 4 cm depth. We further investigate the pressure along the direction at which θ differs from 90° . The pressure fields at 4 cm depth along the direction which differs 10° from the normal ($\theta = 80^\circ$) for focused, PW, and DW transmissions are shown in Figure 4.3. In focused transmission scheme, we observed two separate pressure signals similar in amplitude but opposite in sign.

This means that the transmitted signals are added destructively outside the focal region, even when the angle differs slightly from the normal. A significant decrease in pressure amplitude occurs compared to that obtained along the normal as expected.

Figure 4.3 also shows the time domain pressure pulses for PW and DW transmissions for $\theta = 80^\circ$ and $r = 4$ cm. In PW transmission, we also observed that two separate pressure signals with opposite amplitude appear as in the focused case due to the destructive addition of the transmitted signals at the field point of interest. However, the second pressure pulse is relatively small compared to the first pulse in PW transmission. Similarly, we observed two separate pressure signals with opposite amplitude appear in DW transmission. However, the second pressure pulse is much smaller than the first pulse in DW transmission. The second pressure pulses are referred to as ghost artifacts [1]. These artifacts result from the destructive addition of the transmitted signals from each simulated transducer element and may lead to detection error. Therefore, their negative effects must be eliminated. The first and second pulses are shown in dashed circles in Figure 4.3.

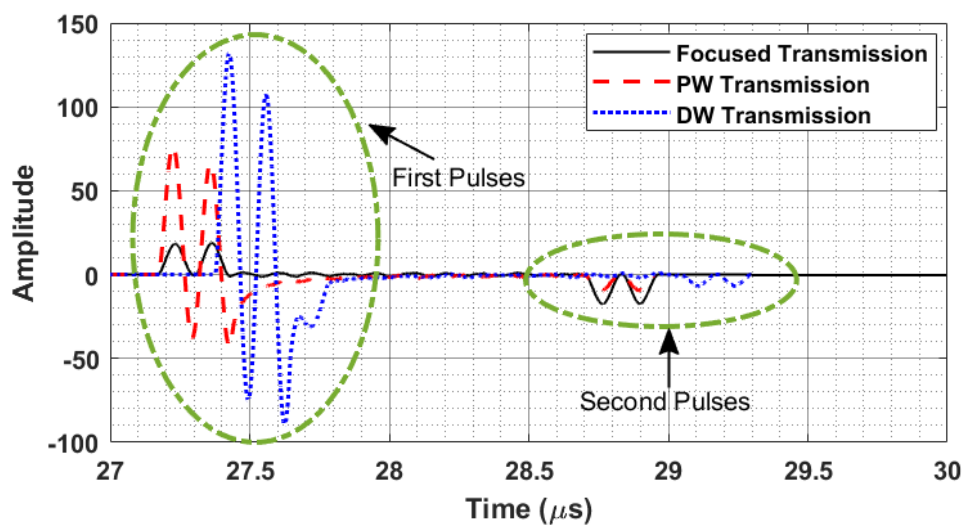


Figure 4.3: Simulation result for the total pressure at the field point for focused, PW, and DW transmissions when $\theta = 80^\circ$ and $r = 4$ cm in a non-attenuating medium. 2-cycle pulse is transmitted from all transducer array elements.

Getting further away from the normal direction causes a decrease in pressure amplitudes for focused, PW, and DW transmissions, as shown in Figure 4.4, where $\theta = 60^\circ$. Again, two pressure pulses with opposite signs appear in the field for all transmission schemes. The second pulse becomes similar in amplitude compared to the first pulse. We observe that the lag of the second pulse increases due to the larger angle. DW transmission performs the best since the ratio between the amplitudes of the first and second pulses is the lowest in DW transmission.

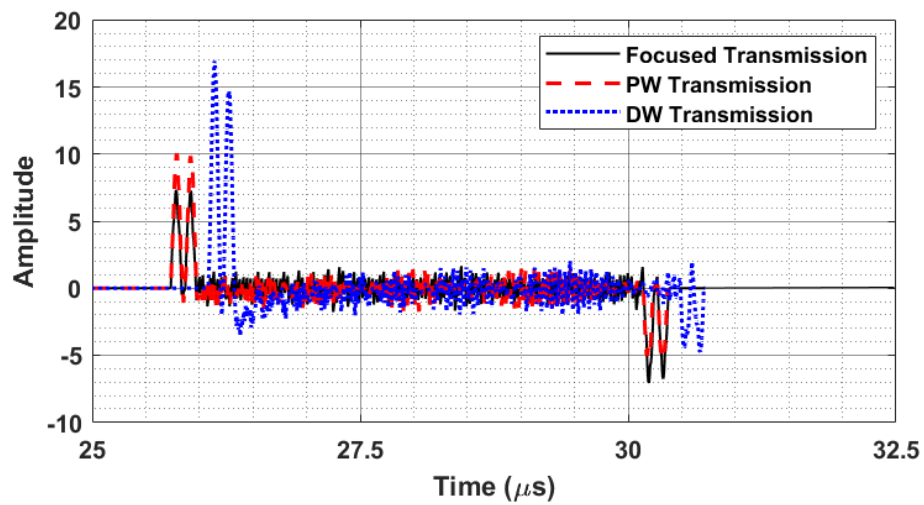


Figure 4.4: Simulation result for the total pressure at the field point for focused, PW, and DW transmissions when $\theta = 60^\circ$ and $r = 4 \text{ cm}$ in a non-attenuating medium. 2-cycle pulse is transmitted from all transducer array elements.

DW transmission performance exceeds the other transmission performances when the pressure field along the direction different from the normal direction is examined. It is intuitive since the transmitted signals are spread over a broader region, and a more uniform insonification is obtained in DW transmission than focused and PW transmissions.

Note that the change in θ affects the distance between the transmitting element and the field point, thus affecting the arrival time of the first pulse to the field point. The time delays applied to each array element in respective transmission scheme is the other parameter that affects the arrival time of the first pulse to the field point.

4.1.2 Simulation Results for Attenuating Medium

We further investigate the coherence of the transmitted signals in an attenuating medium. In the presence of attenuation, the analytical expression derived for the pressure in a non-attenuating medium shown in Eq. (4.1) extends to,

$$\hat{P}_{tot}(r, \theta) = P_{tot}(r, \theta)e^{-\alpha f r_i} \quad (4.4)$$

where α is the attenuation coefficient in the medium, f is the transmit frequency in MHz and r_i is the distance from the transmit element i to the observation point in cm. The attenuation coefficient is set to 0.5 dB/MHz/cm in simulations, which is the same as phantom attenuation.

Figure 4.5 shows the pressure pulse generated at 4 cm and an angle of 30° ($\theta = 60^\circ$) in the attenuating medium. The DW transmission with a 2-cycle pulse is used. We observed that the pressure pulse amplitude decreases significantly in attenuating medium compared to that obtained in nonattenuating medium. The pressure pulses at the field point are encircled with dashed lines for convenience.

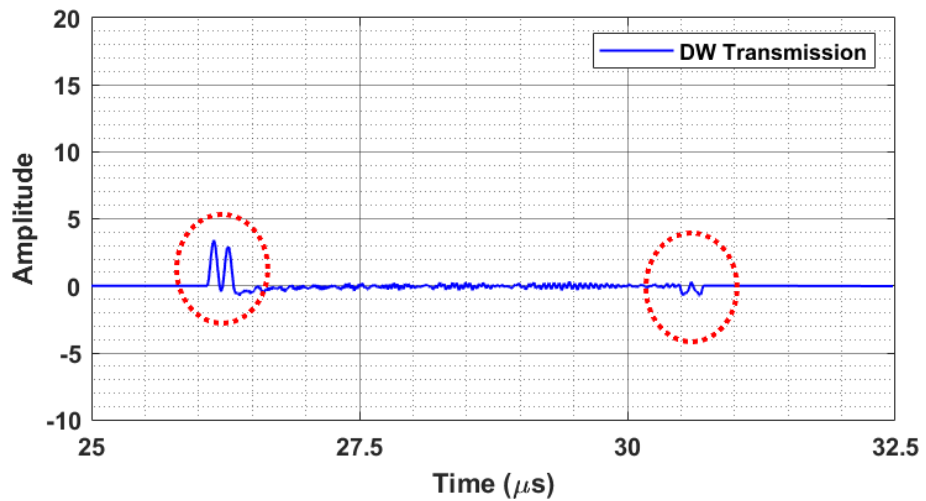


Figure 4.5: Simulation result for the total pressure at the field point for DW transmission when $\theta = 60^\circ$ and $r = 4$ cm in an attenuating medium. 2-cycle pulse is transmitted from all transducer array elements.

The simulations reveal the importance of the transmitted signal coherence in the field of interest. The performance of the respective transmission scheme is directly related to the pressure pulse generated in the field. The destructive addition in pressure pulse at a field point causes degradation in received signal amplitude, distortion in the beamformer output, and deterioration in the ultrasound image. This leads to ghost artifacts in the ultrasound image, which causes image duplication or even triplication. It is also apparent from simulation results that the ghost artifact appears even in the case of 2-cycle pulse transmission which has a $0.267 \mu\text{s}$ duration. The lag of this artifact increases at larger angles.

In this section, we used PW and DW transmission schemes to obtain an unfocused transmission, which causes destructive addition and decreases the transmitted signal coherence along the normal direction in the field compared to focused transmission. Compared to PW transmission, the unmatched phases applied to each array element in DW transmission further aggravate the destructive addition of the transmitted signals in the field. Therefore, it is evident that this increased destructive addition in DW transmission causes further deterioration in the received signals and the performances of the beamforming and imaging processes. On the other hand, DW transmission provides better insonification at larger angles which manifests itself as higher pressure amplitude and a decreased ghost artifact.

4.2 Simulation Results using Field-II and k-Wave

We also investigated the coherence of the transmitted signals in the field and the problems encountered in DWI using a semi-analytical simulation tool and an FEA-based simulation tool, which are commonly used in literature.

We used Field II as a semi-analytical simulation tool based on linear spatial impulse response. We simulated a wire phantom without attenuation using a phased array transducer, as described in the Field II website [58]. The wire

phantom consists of 100,000 scatterers and five-point targets. The transducer has 128 elements and operates at a 7.5 MHz center frequency. The physical elements are divided into two by three mathematical elements to increase the simulation accuracy. We used the respective procedure to obtain the full synthetic aperture scan data as described in [59]. We transmitted a 2-cycle pulse at the center frequency. We benefited from the linearity to obtain the DW data from synthetic aperture data. Therefore, we applied appropriate delays to synthetic aperture received data on each receiving element and obtained DW data. Then, we applied delay-and-sum beamforming, envelope detection, logarithmic compression, and scan conversion on the DW data to construct an image.

The simulated cyst phantom image is shown in Figure 4.6. We observed artifacts in the simulated image, and these artifacts are not caused by the waves coming from the transducer edge elements. These artifacts are independent of the target strength, the scatterer strength, and the number of the scatterers. The artifacts are present when point targets or line targets are employed. The line targets are modeled using 200-point scatterers separated by $50 \mu\text{m}$ (quarter wavelength at the center frequency) along a line.

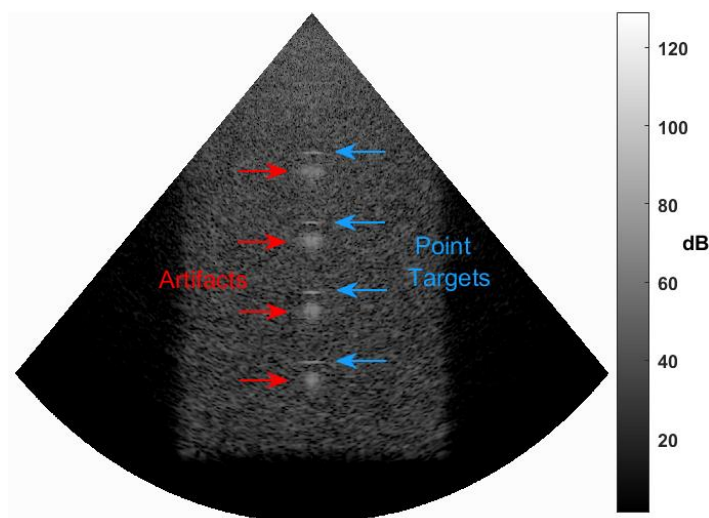


Figure 4.6: Simulated cyst phantom ultrasound image obtained by using DW data. Field II simulation program is used. The blue arrows show the point targets. The red arrows show the artifacts. Color bar is in dB scale.

The beamformed signal along the centerline of the simulated image is also shown in Figure 4.7. The echoes coming from the targets and the artifacts are easily observable and marked for convenience.

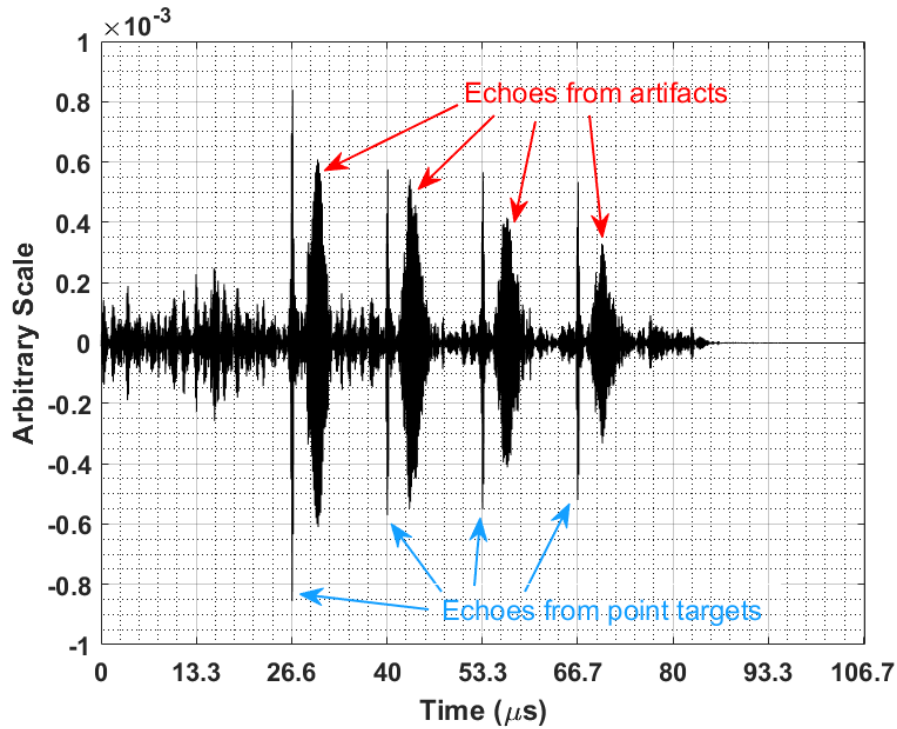


Figure 4.7: Beamformed signal along the center line of the simulated image. The blue arrows show the echoes coming from the point targets. The red arrows show the artifacts in the beamformed signal.

The artifacts observed in the Field II simulation study are similar to those observed in our efforts described in the previous section, where we employed a similar approach as in Field II. However, we do not observe these artifacts in the measurements. We do not employ any transmit and receive apodization in measurements and simulations. Semi-analytical simulation tools based on linear spatial impulse response like Field II produce erroneous results because they model the scatterers as monopole sources. The total signal power or energy in the field increases when the number of scatterers is increased. Therefore, using semi-analytical simulation tools based on linear spatial impulse response is not reliable to solve the wave propagation in multiple scattering and attenuating media.

We also used k-Wave simulation tool, which is an open-source acoustics toolbox [53]. It is an FEA-based simulation tool, where the wave equation is numerically solved in the medium model. We observed that modeling the multiple and weakly scattering media in FEA is critical for correct results. Detailed modeling of the medium is quite involved and results in very long simulation times [83]. This renders the use of FEA practically impossible to solve the wave propagation in multiple scattering and attenuating media.

Chapter 5

Coded Transmission

The conventional ultrasound systems employ short sinusoidal excitation signals [2]. The pulse amplitude or duration can be increased to achieve higher SNR and related performance. However, pulse amplitude is limited with the mechanical index regulations, and duration is limited with axial resolution [2]. The studies on using coded excitation signals in medical ultrasound imaging have been done to increase the SNR and related performance. The performance analysis of coded excitation compared to pulsed excitation is commonly investigated in the literature.

The received echoes in medical ultrasound imaging are distorted significantly due to the propagation medium's attenuation and nonlinear effects. This distortion causes degradation in imaging performance. In DWI, the problem gets further complicated since a high frame rate is achieved at the expense of SNR and related performance. Coded excitation signals are better candidates to solve the problem experienced in DWI. However, the coded waveform selection and the implementation method must be carefully handled. CGSs are commonly used in literature due to their complementarity property, fewer length restrictions, and rich diversity. In this study, we used CGSs to code the transmitted signals.

In this chapter, we first give the literature survey on CGSs. Then, we describe the properties and construction methods of these sequences. We also discuss the modulation scheme used in coded signal construction. In the final part of this chapter, we present the transmitter and receiver configurations for coded DWI.

5.1 Complementary Golay Sequences

The CGSs are first described in a paper dating back to 1961 [60], where the definition, construction method, and general properties are provided. CGSs have aroused interest over many years resulting in the development of these sequences. It was shown that the CGSs are very useful in medical ultrasound imaging due to their desired correlation properties [27].

Most researchers have used the results given in [60] and tried to solve the challenges in the construction of CGSs. In [61], the diversity of these sequences is discussed, and the canonical form for CGSs up to length 40 is provided. It is also possible to produce these sequences from already known sequences by using elementary operations such as multiplication, addition, concatenation, and interleaving [62]. Moreover, the notion of Golay array pairs is discussed, and CGSs are shown to be the projections of multidimensional Golay array pairs [62]. The non-existence of these sequences for some particular lengths is shown in [63].

The studies carried out for complementary sequences contributed to the emergence of new sequences in the literature. The sequences with zero correlations within a zone are proposed in [63] and [64]. This zone is called the zero-correlation zone. It is impossible to simultaneously have impulse-like autocorrelation functions and zero crosscorrelation functions in a sequence set. However, it was shown in [63] and [64] that ideal correlation properties of the sequences can be maintained only at correlation lags within the zero-correlation zone. The system performance does not deteriorate if the correlation values outside this zone are immaterial to the application of interest.

Moreover, it was also shown in [64] that the sequences providing zero correlation zones include conventional CGSs as a special case.

A set is a complementary set if the summation of aperiodic autocorrelation functions of each sequence in the set is equal to zero everywhere except zero phase shift [61]. A complementary set consisting of two sequences is the special case, which is called complementary Golay pair. Let A and B are the two CGSs with length n and given as $A = (A_0 A_1 A_2 \dots A_{n-1})$ and $B = (B_0 B_1 B_2 \dots B_{n-1})$. A_i 's and B_i 's are the elements of each CGS. CGSs are also known as bipolar sequences since the sequence elements only take the values of 1's and -1 's.

The CGSs, unlike the other code sequences, offer zero code range lobe. The sum of the autocorrelation functions of two sequences doubles at zero phase shift while it is zero for non-zero phase shifts. This property is known as the complementarity property. Let us define the autocorrelation function of each CGS as follows:

$$\begin{aligned} ACF_{A,j} &= \sum_{i=0}^{i=n-j} A_i A_{i+j} \\ ACF_{B,j} &= \sum_{i=0}^{i=n-j} B_i B_{i+j} \end{aligned} \tag{5.1}$$

According to the complementarity property, the relation between the autocorrelation functions of the two sequences can be written as:

$$ACF_{A,j} + ACF_{B,j} = \begin{cases} 0, & j \neq 0 \\ 2n, & j = 0 \end{cases} \tag{5.2}$$

We used 2, 4, 8 and 10-bit coded CGSs to code the transmitted signal in this study. We constructed these coded signals by means of the look up table and canonical forms given in [61]. Table 5.1 and Table 5.2 show the bipolar representation of these code sequences.

Table 5.1: Bipolar Representation of 2, 4, 8 and 10-chips CGS(A). These sequences are used to code the transmitted signals in coded DWI.

Sequence Type	Code Length	Bipolar Representation
CGS(A)	2 chips	{1, 1}
	4 chips	{1, 1, -1, 1}
	8 chips	{1, 1, -1, -1, -1, 1, -1, 1}
	10 chips	{1, 1, 1, 1, 1, -1, 1, -1, -1, 1}

Table 5.2: Bipolar Representation of 2, 4, 8 and 10-chips CGS(B). These sequences are used to code the transmitted signals in coded DWI.

Sequence Type	Code Length	Bipolar Representation
CGS(B)	2 chips	{1, -1}
	4 chips	{1, 1, 1, -1}
	8 chips	{1, 1, 1, 1, -1, 1, 1, -1}
	10 chips	{1, 1, -1, -1, 1, 1, 1, -1, 1, -1}

We used different code lengths (number of chips in the sequence) and chip lengths (duration of each chip) in the measurements. For example, Figure 5.1 shows the 8-bit coded CGS(A) and CGS(B) coded signals with different chip durations. Here, 180° phase transition occurs in the coded signals when the bit in the sequence changes from “+1” to “-1” or vice versa since we used Binary Phase Shift Keying (BPSK) to modulate the coded signals. The bit value of “1” corresponds to the 0° chip signal phase, and “-1” corresponds to the 180° phase.

The bit transitions are clear in Figure 5.1 when the code bit goes from “1” to “-1” or vice versa. In coded signals, the symbol used for each code bit is referred to as a chip. For example, the length of an 8-bit coded signal is 8-chip long. The 2-cycle/chip CGS(A) and CGS(B) coded signals with different code lengths are also shown in Figure 5.2.

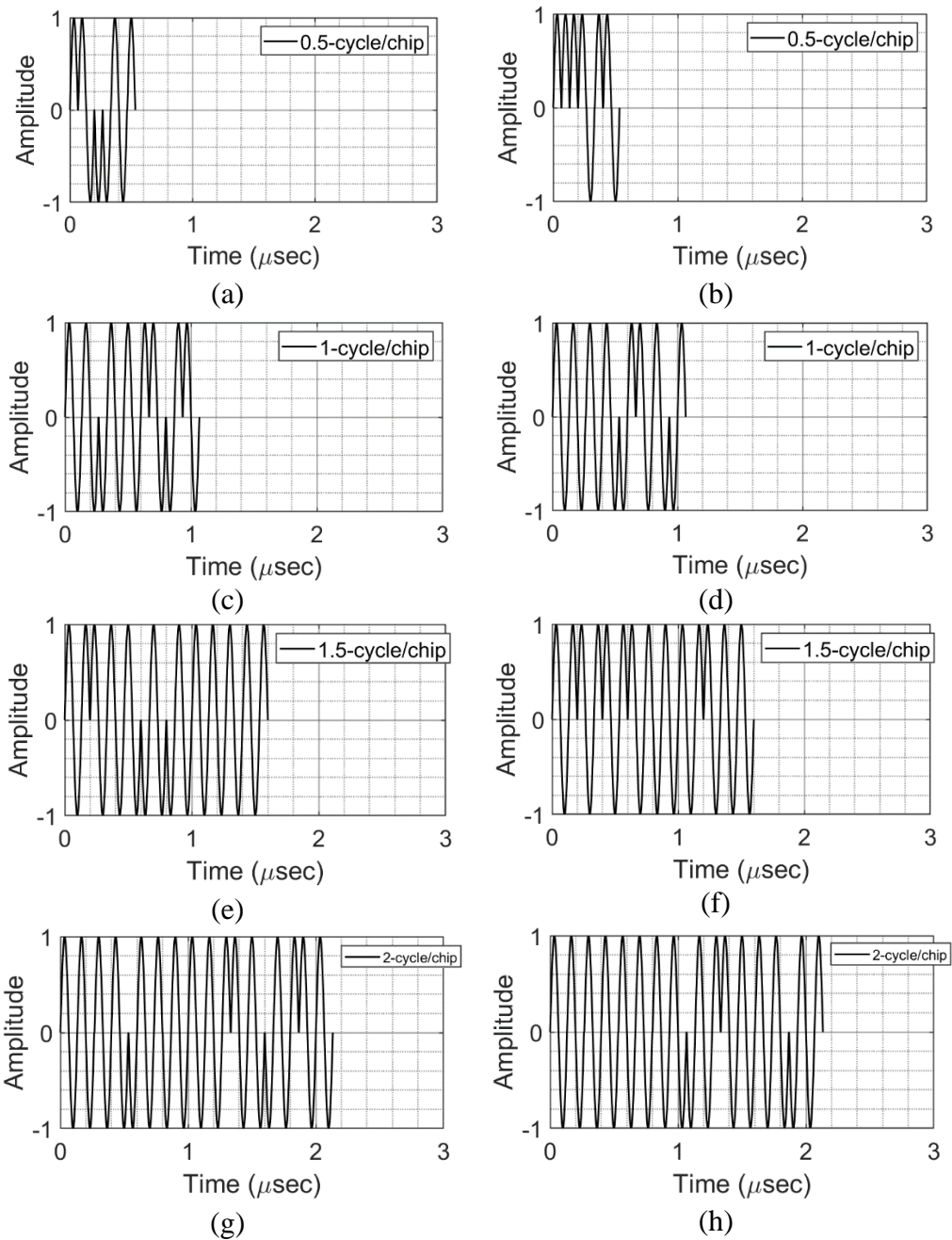


Figure 5.1: The 8-chip CGS coded signals with different chip lengths used in the measurements. (a) CGS(A) coded signal with 0.5 cycle/chip. (b) CGS(B) coded signal with 0.5 cycle/chip. (c) CGS(A) coded signal with 1 cycle/chip. (d) CGS(B) coded signal with 1 cycle/chip. (e) CGS(A) coded signal with 1.5 cycle/chip. (f) CGS(B) coded signal with 1.5 cycle/chip. (g) CGS(A) coded signal with 2 cycle/chip. (h) CGS(B) coded signal with 2 cycle/chip.

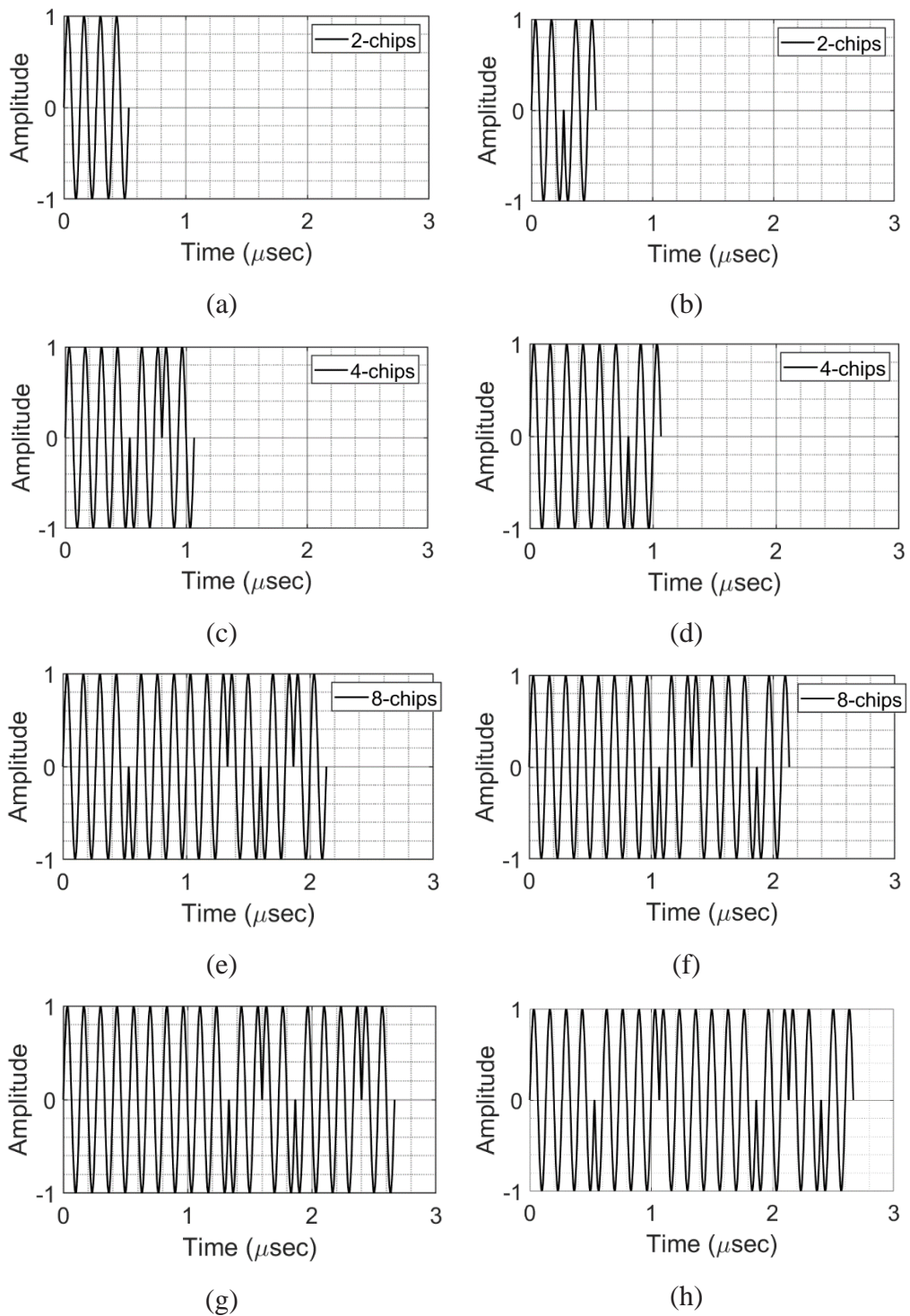


Figure 5.2: The 2-cycle/chip CGS coded signals with different code lengths used in the measurements. (a) CGS(A) coded signal with 2 chips. (b) CGS(B) coded signal with 2 chips. (c) CGS(A) coded signal with 4 chips. (d) CGS(B) coded signal with 4 chips. (e) CGS(A) coded signal with 8 chips. (f) CGS(B) coded signal with 8 chips. (g) CGS(A) coded signal with 10 chips. (h) CGS(B) coded signal with 10 chips. Each chip is 2-cycle long (2-cycles/chip).

Figure 5.3 shows the complementarity property associated with 8-chips CGS coded signals. The aperiodic autocorrelation of each sequence, shown in Figure 5.3(a) and Figure 5.3(b) respectively, is same in amplitude but opposite in sign at non-zero phase shifts. This yields a perfect cancellation at non-zero phase shifts, as shown in Figure 5.3(c) when they are summed up. Note that the CGS(A) and CGS(B) coded signals with 2-cycles/chip has $2.133 \mu\text{s}$ duration. Hence the summation of the autocorrelations doubles at $2.133 \mu\text{s}$ as expected. CGSs have the unique property that they offer zero code range lobe due to this cancellation.

On the other hand, the sum doubles at zero phase shift, as shown in Figure 5.3(c). Individual aperiodic autocorrelations are obtained using the 2 cycle/chip case. However, the complementarity property does not depend on the code or chip length used to construct the CGS-coded signal.

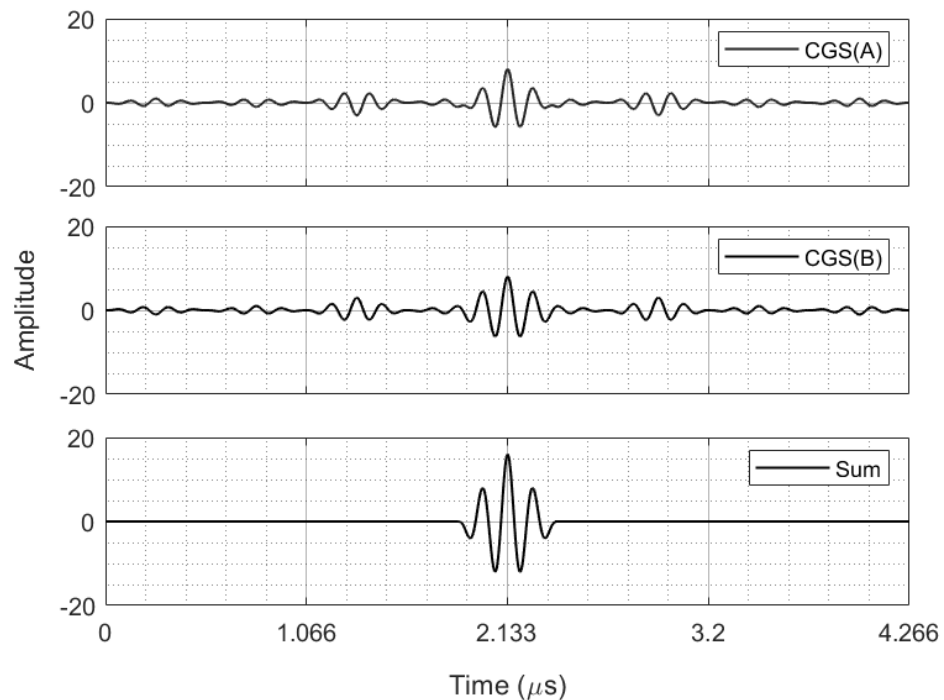


Figure 5.3: The illustration of the complementarity property by using 8-chip long CGSs with 2-cycle/chip. (a) Autocorrelation of the CGS(A) coded signal. (b) Autocorrelation of the CGS(B) coded signal. (c) The sum of the autocorrelations.

5.2 Modulation Scheme

We used BPSK to modulate the coded signals since it supports the complementarity property. However, the BPSK modulated coded signals suffer from energy loss due to phase and amplitude discontinuities involved. The modulation schemes offering constant phase and amplitude may be a better choice to avoid the energy loss of the coded signals. Therefore, we also investigated the Continuous Phase Modulation (CPM) techniques such as Frequency Shift Keying (FSK), Minimum Shift Keying (MSK), and Gaussian Minimum Shift Keying (GMSK) in this study.

The continuous phase modulated signals are suitable for improving transmission and reception efficiencies due to their constant phase and amplitude nature. Therefore, the continuous phase modulated signals suffer less from energy loss than BPSK modulated signals. However, we found that the coded signals modulated with CPM techniques do not support the complementarity property.

Figure 5.4 shows the sum of aperiodic autocorrelations of MSK modulated CGS(A) and CGS(B) signals. We observed that the prominent range lobe amplitude level is almost one-third of the main lobe, implying that MSK modulated signals suffer from strong range lobes. Similar behaviour is also observed in other continuous phase modulation schemes. Since complementarity property is critical to obtain high-resolution ultrasound images, we preferred to modulate the coded signals with BPSK modulation in our study.

There is a tradeoff between the complementarity and energy loss when CPM techniques are employed for modulation. Determination of the appropriate modulation technique must be considered in conjunction with this tradeoff. This issue requires further study and is a potential area for improvement.

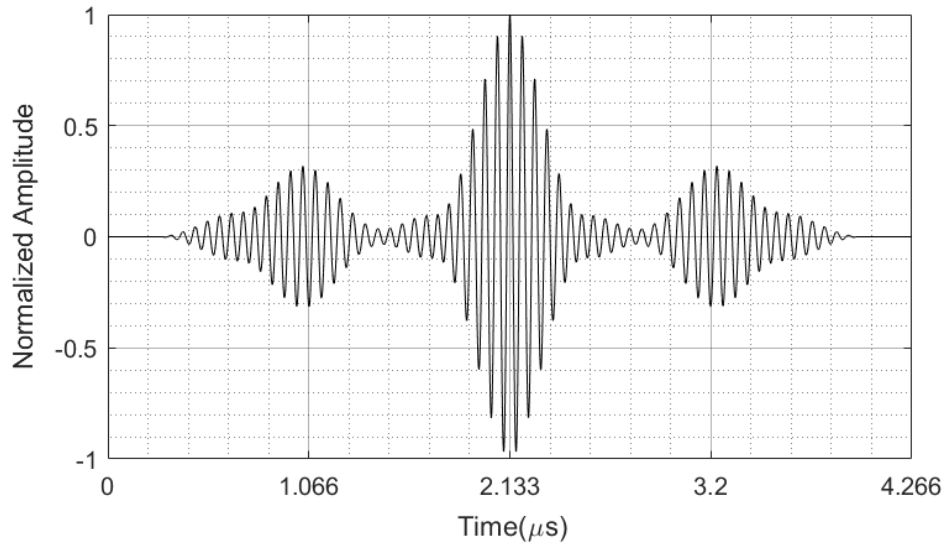


Figure 5.4: Summation of the aperiodic autocorrelations of CGS(A) and CGS(B) coded signals under MSK modulation. The amplitude is normalized with respect to its maximum.

5.3 Transmitter and Receiver for Coded Transmission

Coded signals increase available energy at a given power without sacrificing bandwidth [3]. This property can improve the SNR and related performance in ultrasound imaging.

Coded transmission requires correlation receivers for detection where correlator output is maximum at zero phase shift and low at other phase shifts [65]. These lower correlator outputs are referred to as code side lobe. The presence of code side lobes affects the range resolution. We used the term range lobe rather than side lobe to avoid confusion with the transducer side lobes.

The receiver for coded signals incorporates MF. The MF properties are determined by the properties of the coded transmit signal, which is modified by the transducer and medium attenuation. There are various receiver implementation methods in the literature, such as the frequency domain [23] and

time domain [27] approaches. We used the regular implementation of the coded signal. We employed correlation receiver implementation, which is common in real-time applications [66]. Since matched filtering is a linear operation, it can be used directly on the received channel data as well as on the beamformed data, equivalently.

Figure 5.5 shows the transmitter configuration used in this study for CGS-coded DWI. Time delays are applied to each array element to obtain the required wave profile. We transmit CGS(A) and CGS(B) coded signals successively from the transducer array.

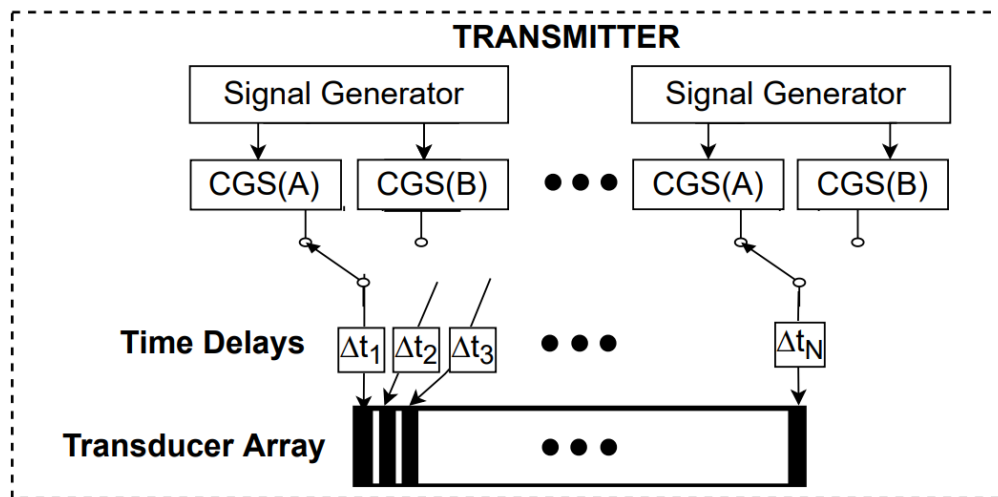


Figure 5.5: Transmitter configuration for coded DWI. CGS(A) is a Golay sequence, and CGS(B) is its complementary sequence. The transducer elements are driven by CGS(A) and CGS(B) coded signals successively. Appropriate time delays are applied to each array element to form a diverging wavefront.

Figure 5.6 shows the receiver configuration used in this study for CGS-coded DWI. The same transducer array is also used in reception. First, we filtered the CGS(A) coded received signals at each array element using the MF consisting of a mixer and an integrator.

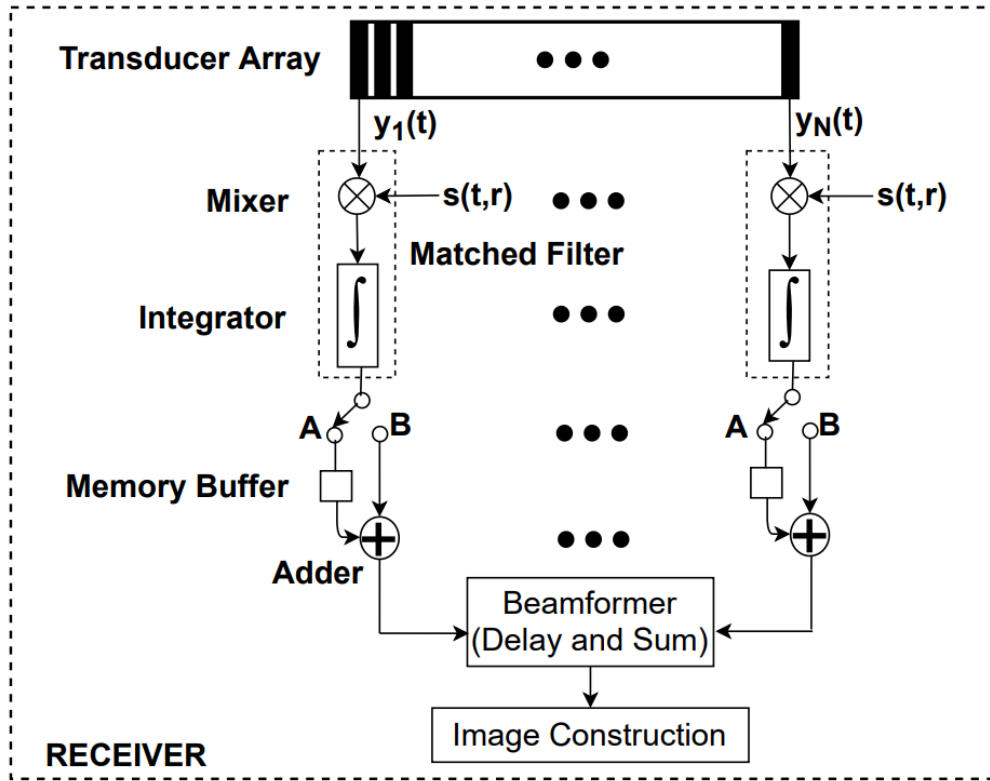


Figure 5.6: Receiver configuration for coded DWI. The same transducer is used for both transmission and reception. A matched filtering is applied to received data. The resulting MF output is beamformed and post-processed to construct the ultrasound image.

The MF output for the i th transducer array element $\hat{R}_{ys,i}$, is expressed as:

$$\hat{R}_{ys,i}(m) = \sum_{k=0}^{K-1} y_i(m+k) s_r(k) \quad (5.3)$$

where $y_i(l)$ is the l th sample of the received signal at the i th transducer array element and $s_r(k)$ is the k th sample of the reference signal with length K . For example, K is 146 for the 8-chip coded signal with 1-cycle/chip and 218 for 2-cycle/chip. Note that the increase in reference signal length is less than two folds due to the transducer transient response in each chip [67].

We compensated the reference signal for the attenuation in the medium, and it was updated 12 times at every 0.5 cm depth. The depth index, r , refers to the updated reference signal, where r ranges from 1 to 12. We describe the attenuation compensation in detail in Chapter VI. The MF output for CGS(A) coded transmission is buffered until the next CGS(B) coded transmission data is collected. Then, we added the MF outputs at each array element for two transmissions. The resulting signals are then beamformed using a delay-and-sum receive beamformer [47] to form the image scan lines. We employed Hilbert transform-based envelope detection [47] on the scan line data to obtain envelope information, which was subsequently used for SNR calculation and image construction. Image construction comprises evaluating $20 \log$ of envelope data and scan conversion [55].

Chapter 6

Reference Signal in Attenuating Medium

The correlation receiver requires a reference signal to compare the received signal. SNR is maximized if the received data contains the replicas of the reference signal [68]. The transducer transfer function modifies the driving transmit waveform significantly. Furthermore, the pressure waveform changes as the wave travels through the medium. The energy in the higher frequency range is absorbed more, and the signal mean frequency decreases with depth. Therefore, the reference signal must be modified to match the received pressure from different depths for higher correlation.

Compensation for the attenuation increases the correlation between the received ultrasonic signal and the reference signal, which yields SNR improvement. Therefore, we compensated the two-way transmitted-and-received signal for the nominal frequency-dependent attenuation. We used the resulting signal as the reference signal in the correlation receiver. We observed that using the compensated two-way transmitted-and-received signal as the reference signal improves the SNR at the correlator output by up to 6 dB compared to using an uncompensated two-way transmitted-and-received signal. We also observed that using the driving transmit waveform as the reference signal causes a further decrease in SNR because both the transducer transfer function and the attenuation in the medium modifies the transmitted signal very significantly.

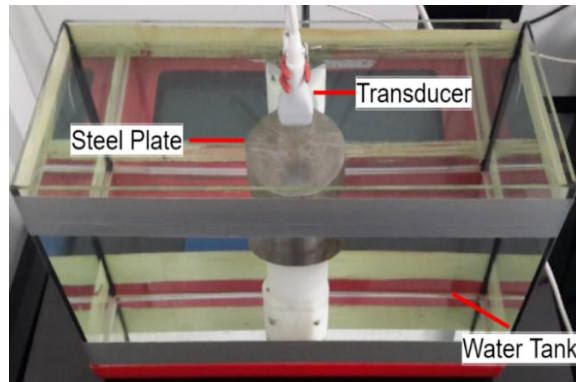


Figure 6.1: The freshwater measurement setup. The steel plate is immersed in the water at 5 cm depth and the transducer is positioned over the steel plate. The size of the water tank is $50 \times 20 \times 30$ cm (length, width and depth).

We used two reference signals, one for each CGS. The reference signal must be a two-way transmitted-and-received signal to include the effect of the transducer transfer function. We measured the two-way transmitted-and-received signal in freshwater to clearly observe the effect of this function. Figure 6.1 shows the freshwater measurement setup. A highly reflective material, a thick steel plate, was immersed in the water at 5 cm depth (approximately). We transmitted from the mid-element, 64th element, of the phased array transducer and conducted pulse-echo measurements for all code and chip lengths combinations.

As an example, the 8-chip coded received signals with 0.5, 1, 1.5, and 2 cycles/chip at the 64th array element are illustrated in Figure 6.2. The attenuation in freshwater is negligible compared to tissue attenuation. Therefore, the signals shown in Figure 6.2 preserve the bit-transitions when the code bits go from “-1” to “1” or vice versa. These signals approximate the unattenuated reference signals for each array element since the two-way electro-mechanical transfer functions of all combinations of the transducer elements are not exactly the same.

The 2-cycle/chip coded received signals with 2, 4, 8, and 10 chips at the 64th array element are also illustrated in Figure 6.3. The signals preserve the bit-transitions when the code bits go from “-1” to “1” or vice versa as in those shown in Figure 6.2.

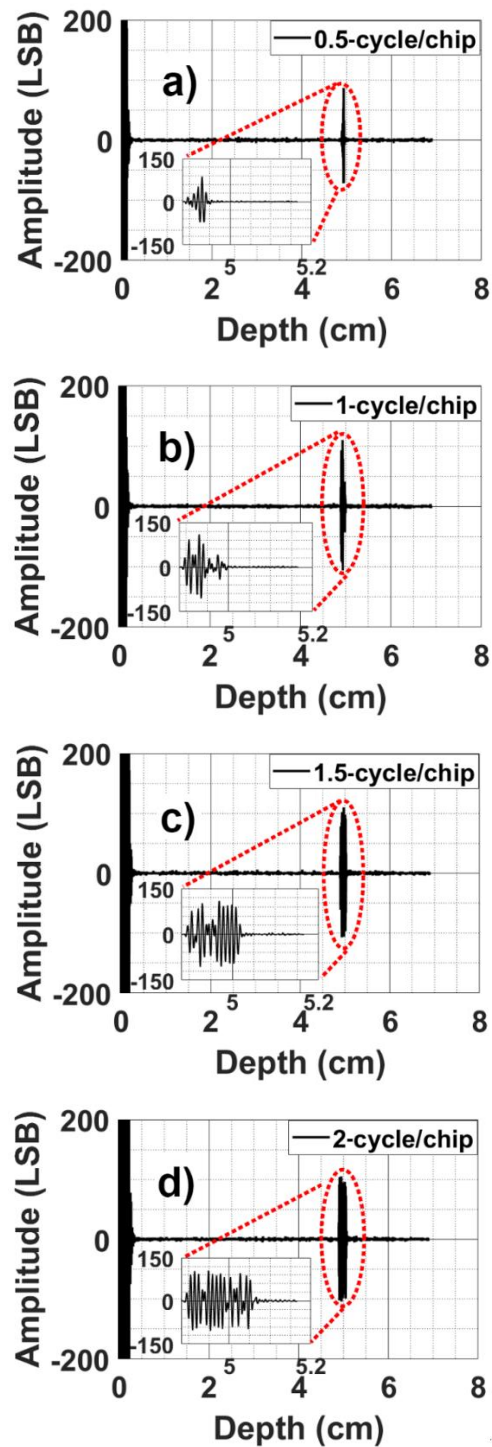


Figure 6.2: The signals reflected from the thick steel plate and received by the 64th element of the phased array transducer. 8-chip CGS(A) coded received signal with (a) 0.5-cycle/chip, (b) 1-cycle/chip, (c) 1.5-cycle/chip, (d) 2-cycle/chip. The amplitude unit in this work is in terms of LSB of DiPhAS acquisition system.

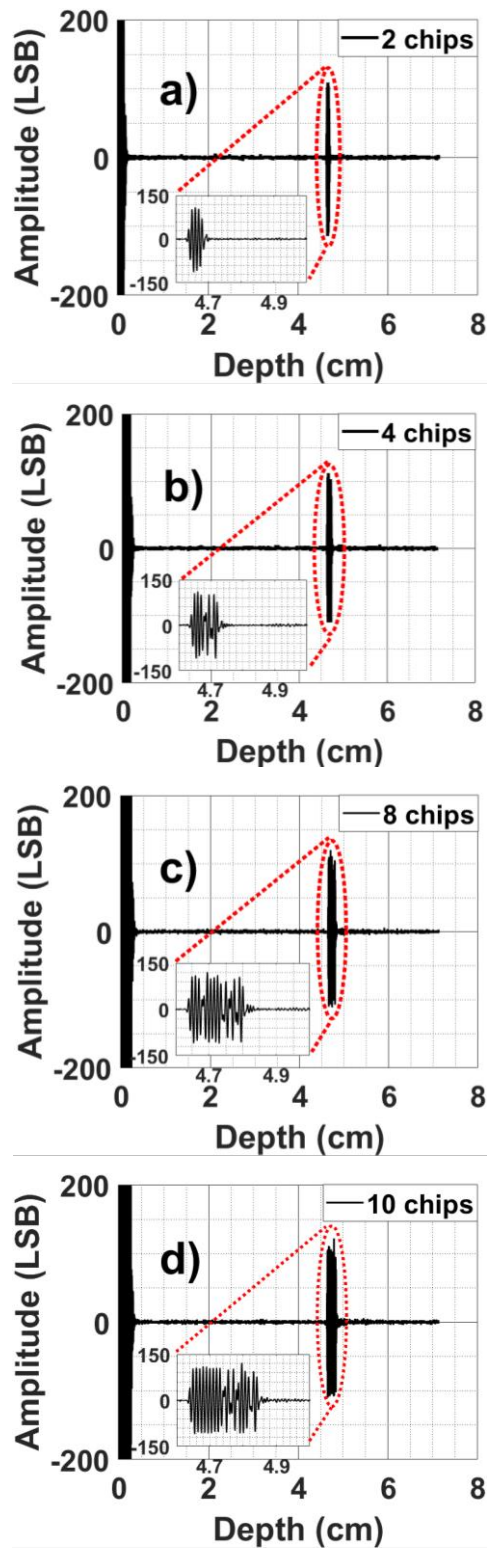


Figure 6.3: The signals reflected from the thick steel plate and received by the 64th element of the phased array transducer. 2-cycle/chip CGS(A) coded received signal with (a) 2 chips, (b) 4 chips, (c) 8 chips, (d) 10 chips. The amplitude unit in this work is in terms of LSB of DiPhAS acquisition system.

The attenuation prevents the perfect cancellation of code range lobes of the Golay pairs [3]. This attenuation effect must also be imposed on the reference signal to improve the MF output in the attenuating medium. We applied attenuation compensation to the two-way transmitted-and-received signal at every 0.5 cm up to 6 cm depth. We performed this compensation on the reference signal in the frequency domain by applying exponential attenuation at the aforementioned depths. We first transformed the uncompensated reference signal, $s(t)$, into the frequency domain and obtained $S(f)$. We performed the attenuation compensation on $S(f)$ as:

$$S_r(f) = S(f) e^{-\alpha f(2r)} \quad (6.1)$$

to obtain the compensated reference signal $S_r(f)$ transform for depth r in cm, where f is the frequency in MHz and α is the nominal attenuation coefficient of the phantom, which is 0.057 Nepers/cm/MHz. We then transformed $S_r(f)$ back to the time domain and obtained $s_r(t)$.

After applying attenuation correction, we normalized the energy of each coded signal based on their code length. The energy of each coded signal is proportional to its code length. For example, the energy of a 4-chip coded signal is 4 LSB²-s, and an 8-chip coded signal is 8 LSB²-s, regardless of their chip length or, i.e., chip signal duration. We used these normalized signals as reference signals in the MF. When a fixed energy reference signal is used in the correlator, the gain in the correlator remains the same for all fixed-energy reference signals.

6.1 Reference Signals for Fixed Code Length

The reference signals of the coded signals with the same code length but different chip lengths have the same fixed energy. For example, the energy of each reference signal of 8-chip coded signal with 0.5, 1, 1.5, and 2 cycles/chip is 8 LSB²-s regardless of the chip length. 8-chip CGS(A) coded reference signals with 0.5, 1, 1.5, and 2 cycle/chip are shown in Figure 6.4. The amplitude of the

reference signals with longer chips is lower in fixed energy reference signals. The bit and phase transitions are delineated in Figure 6.4 (d). Note that 180° phase transitions are visible at 0.5 cm and 1.5 cm depths when the coded signal bits go from “+1” to “-1” or vice versa. The phase transition instants are also visible.

Attenuation compensation distorts the reference signal. The phase transitions become visually less observable at longer ranges, 2.5 cm and 4.5 cm depths. Similar behavior is also visible in Figure 6.4 (a), Figure 6.4 (b) and Figure 6.4 (c).

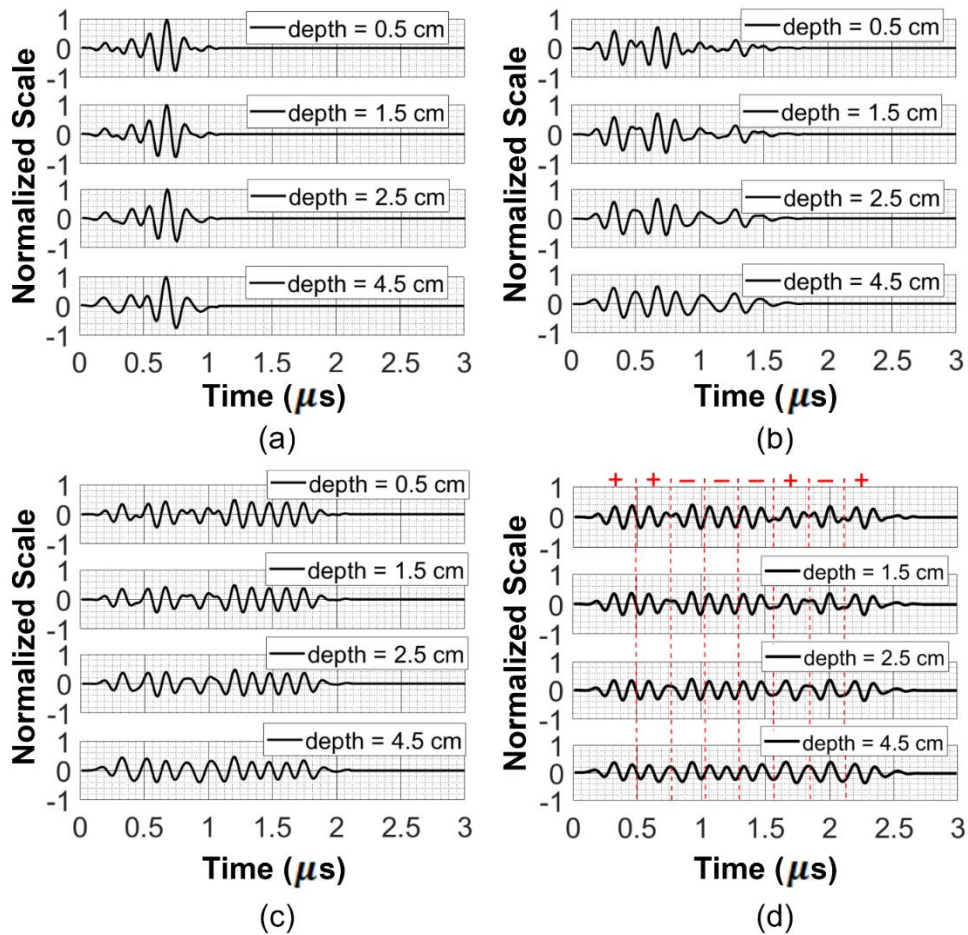


Figure 6.4: Received signals on the 64th element of the phased array transducer after attenuation compensation. All signal energy is fixed at $8 \text{ LSB}^2\text{-s}$. 8-chip CGS(A) coded received signal with (a) 0.5-cycle/chip, (b) 1-cycle/chip, (c) 1.5-cycle/chip, (d) 2-cycle/chip. The bit transitions and phase transition instants are marked for convenience. Every row within each figure corresponds to adaptive attenuation compensation with respect to depths of 0.5, 1.5, 2.5, and 4.5 cm (return path length of 1, 3, 5, and 9 cm), respectively.

6.2 Reference Signals for Fixed Chip Length

The reference signals of the coded signals with different code lengths but the same chip length have different energies, which are proportional to the number of chips it contains. Thus, a single chip reference signal has unit energy, the energy of a 2-chip coded signal is $2 \text{ LSB}^2\text{-s}$, the energy of a 4-chip coded signal is $4 \text{ LSB}^2\text{-s}$. This corresponds to keeping the amplitude of the coded signals fixed, regardless of the code length. A 1-chip pulsed reference signal with 2-cycle/chip and 2, 4, and 8-chips CGS(B) coded reference signals with a 2-cycle/chip are shown in Figure 6.5. Note that the amplitudes of the reference signals remain the same. Similarly, 180° phase transitions are visible at 0.5 cm and 1.5 cm depths when the coded signal bits go from “+1” to “-1” or vice versa.

Attenuation compensation distorts the reference signal. The phase transitions become visually less observable at longer ranges, 2.5 cm and 4.5 cm depths. Similar behavior is also visible in Figure 6.5 (a), Figure 6.5 (b) and Figure 6.5 (c).

On the other hand, since the reference signal used in the MF of CSFI-MF is only either a 1-cycle signal (1 chip of 1-cycle/chip) or 2-cycle signal (1 chip of 2-cycle/chip), its energy is either $1 \text{ LSB}^2\text{-s}$ or $2 \text{ LSB}^2\text{-s}$.

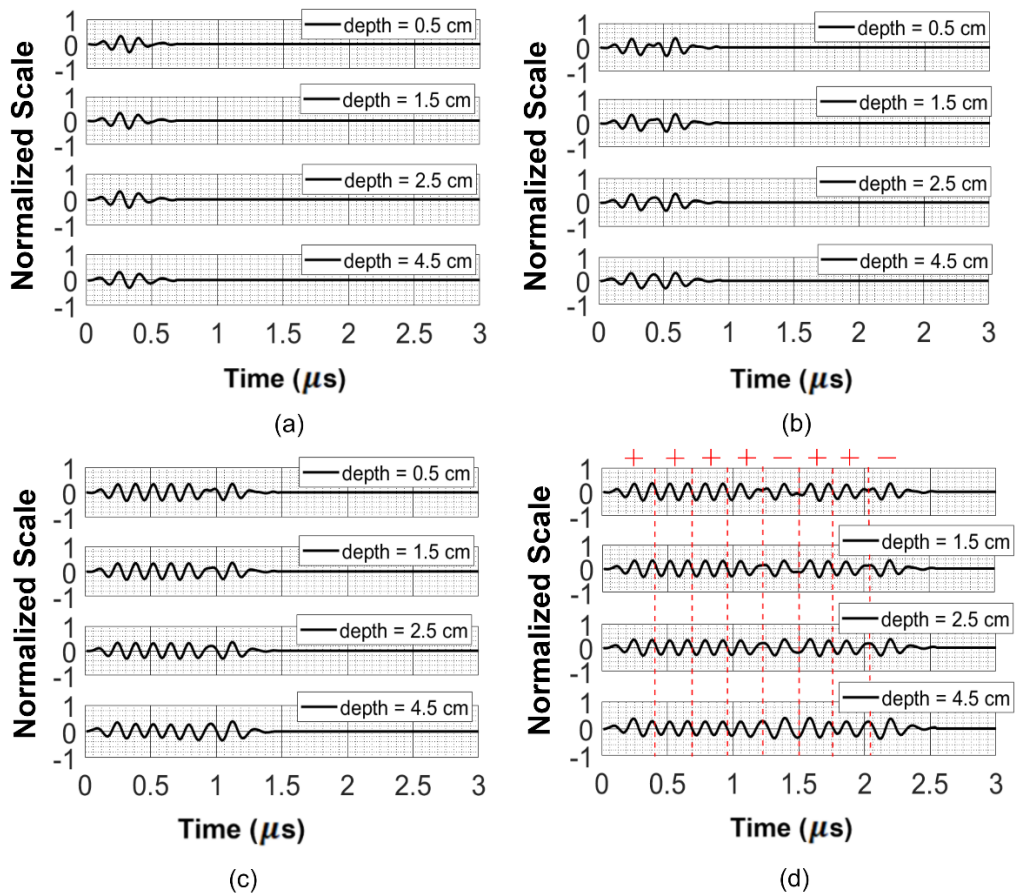


Figure 6.5: Received signals on the 64th element of the phased array transducer after attenuation compensation. The signal energies are 1, 2, 4, and 8 $\text{LSB}^2\text{-s}$, respectively for pulsed signal and 2, 4, and 8-chip coded signals. (a) 1-chip pulsed signal with 2-cycle/chip (b) 2-chip CGS(B) coded signal with 2-cycle/ chip. (c) 4-chip CGS(B) coded signal with 2-cycle/ chip, (d) 8-chip CGS(B) coded signal with 2-cycle/ chip. Every row within each figure corresponds to adaptive attenuation compensation with respect to depths of 0.5, 1.5, 2.5, and 4.5 cm (return path length of 1, 3, 5, and 9 cm), respectively.

Chapter 7

Diverging Wave Transmission for Fast Ultrasound Imaging

7.1 Ultrasound Energy Confinement in the Region of Interest

SNR in DWI is related to the available ultrasound energy in the region of interest. An appropriate DW profile keeps the ultrasound energy in the region of interest. Therefore, we determine an optimum DW profile to adequately confine the transmitted energy into the sector to be imaged. Using this profile yields the required beamwidth and contributes to the SNR improvement.

We obtained the DW profile by applying appropriate phases to array elements so that a cylindrically DW emanates from the array. We determined the phase profile used for a particular DW by the geometry given in Figure 7.1. The transmitted wave is assumed to be generated by an equivalent virtual source [16]. The assumed virtual source is a cylindrical omnidirectional line source. It is positioned behind the transducer array center at a distance of r_p . Since this virtual source has a negative axial coordinate, while the imaging field of view has a positive axial coordinate, DWI is commonly referred to as imaging with virtual negative focus. The omnidirectional cylindrical wave is assumed to be windowed by the array aperture; thus, the insonification sector is established. The half insonification sector is the solid-colored region in Figure 7.1.

The element pitch, d , is half of the wavelength at 7.5 MHz. The aperture length is Nd , where N is 128. The aperture length of the phased array transducer used in the measurements is 12.8 mm. When the delay profile is configured for a short r_v , the virtual source is close to the aperture, and the total available energy diverges to a wide insonification sector. When the profile is set for a long r_v , energy is confined to an acute sector and the transmission converges to plane wave transmission.

Actual energy distribution in the sector differs from the geometrical predictions due to diffraction and multiple scattering. The geometrical divergence sector is shown with a dotted arrow in Figure 7.1 and φ is the geometrical divergence sector angle. φ can be calculated as given in Eq. (7.1). As a result of diffraction and multiple scattering, the insonification sector is significantly broader than this geometrical divergence sector.

$$\varphi = 2 \times \tan^{-1} \left(\frac{Nd}{2r_v} \right) \quad (7.1)$$

Maximum SNR at the central region is obtained when r_v is as large as possible. However, r_v must be low enough to adequately insonify the imaging sector, which is 90° in this study. The half imaging sector is the cross-hatched region in Figure 7.1. Note that the insonification sector is also broader than this imaging sector. We adopted a criterium based on the SNR for adequate insonification within the imaging sector. We determined the r_v such that the SNR difference between the center and the outermost regions in the imaging sector is 3 dB. We measured the SNR of the coded DWI in the speckle region along arcs for different virtual source positions. As shown in Figure 7.1, an arc constitutes equidistant imaging points from the transducer array center.

A 10.5 mm virtual source distance yields an adequate insonification and uniform SNR distribution in the 90° imaging sector.

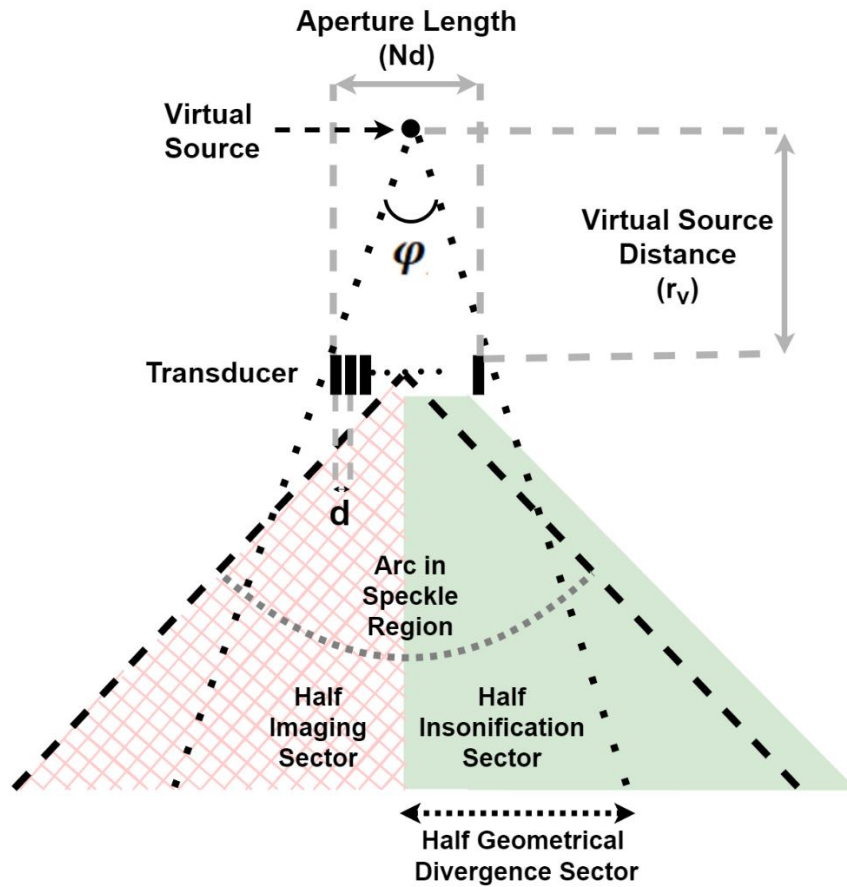


Figure 7.1: The geometry used to derive a phase profile for a particular DW. The transducer aperture length is Nd , where N is the number of the transducer array elements and d is the element pitch. In this study, N is 128, and d is half of the wavelength at the 7.5 MHz center frequency. For a given aperture, the virtual source distance, r_v , determines the geometrical divergence sector. φ is the geometrical divergence sector angle. The time delays applied to each array element is calculated for the geometrical beamwidth of φ . Insonification sector is wider than the geometrical divergence sector due to the diffraction. The arc in speckle region is also shown along which SNR is measured to determine the appropriate virtual source distance and the required beamwidth.

7.2 Noise in Diverging Wave Imaging

We performed the noise measurements using the method described in Chapter III. Figure 7.2 shows the noise contribution for the total noise in DWI (for CGS(A) and CGS(B)) in the case of fixed code length and varying chip length. Figure 7.2 also shows the noise contribution for one transmission in CSFI. The noise level in CSFI is discussed in Chapter X.

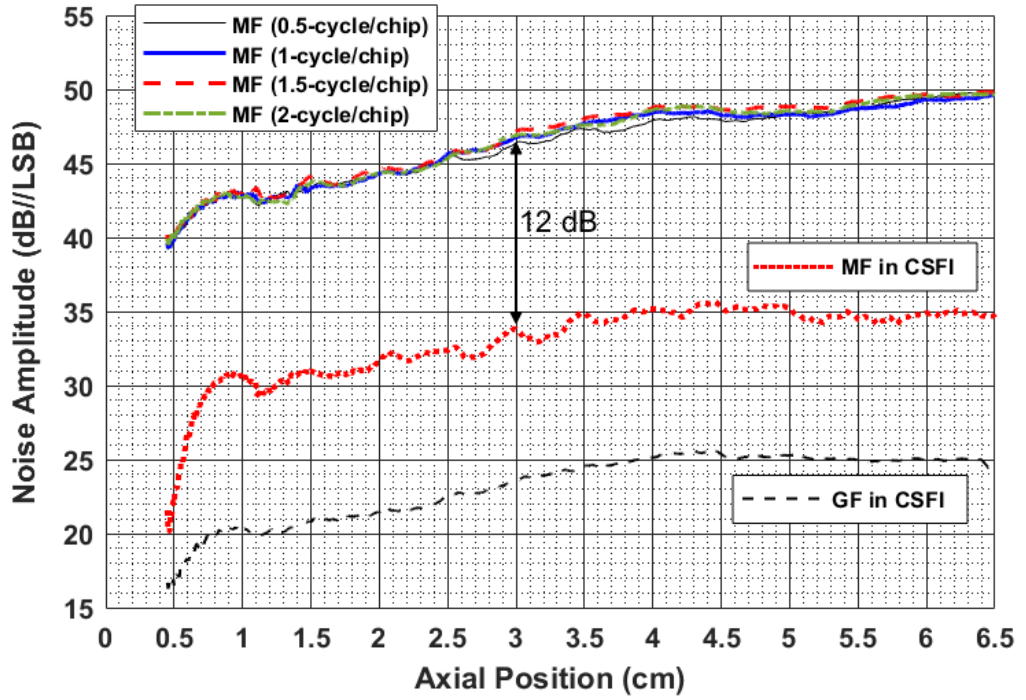


Figure 7.2: Noise amplitude for coded DWI (8 chips and $r_p = 10.5$ mm) with 4 different chip lengths. The noise amplitude variation with respect to depth is same for all chip lengths. This graph also shows the noise level in CSFI-GF and CSFI-MF. Note that the noise analysis for coded DWI (implemented with MF), CSFI-GF, and CSFI-MF have different gains. The average noise power is measured over independently taken 13 measurements without any transmission. The received noise amplitude is plotted in dB//LSB. The arrow shows the 12 dB increase in noise between MFs of CSFI and DWI.

We calculated the noise contribution in coded DWI using the respective reference signals, which are 8-chip coded signals with 0.5, 1, 1.5, and 2-cycles/chip. The unit of the received noise amplitude is dB//LSB. The noise contribution to the signal remains at the same level for all chip lengths since all reference signals in DWI are normalized to have the same energy, $8 \text{ LSB}^2\text{-s}$. Therefore, the correlator gain is the same for all reference signals.

Figure 7.3 shows the noise contribution for the total noise in DWI (for CGS(A) and CGS(B)) in the case of fixed chip length and varying code length. Figure 7.3 also shows the noise contribution for one transmission in CSFI. The noise level in CSFI is discussed in Chapter VIII. We calculated the noise contribution in coded DWI using the respective reference signals, which are 2, 4,

8, and 10-chip coded signals with 2-cycles/chip. When the code length is doubled, the noise amplitude is increased by 3 dB, as shown in Figure 7.3. Note that the significant noise amplitude difference between GF and MF noise is mainly due to the difference in the frequency response of the respective filters.

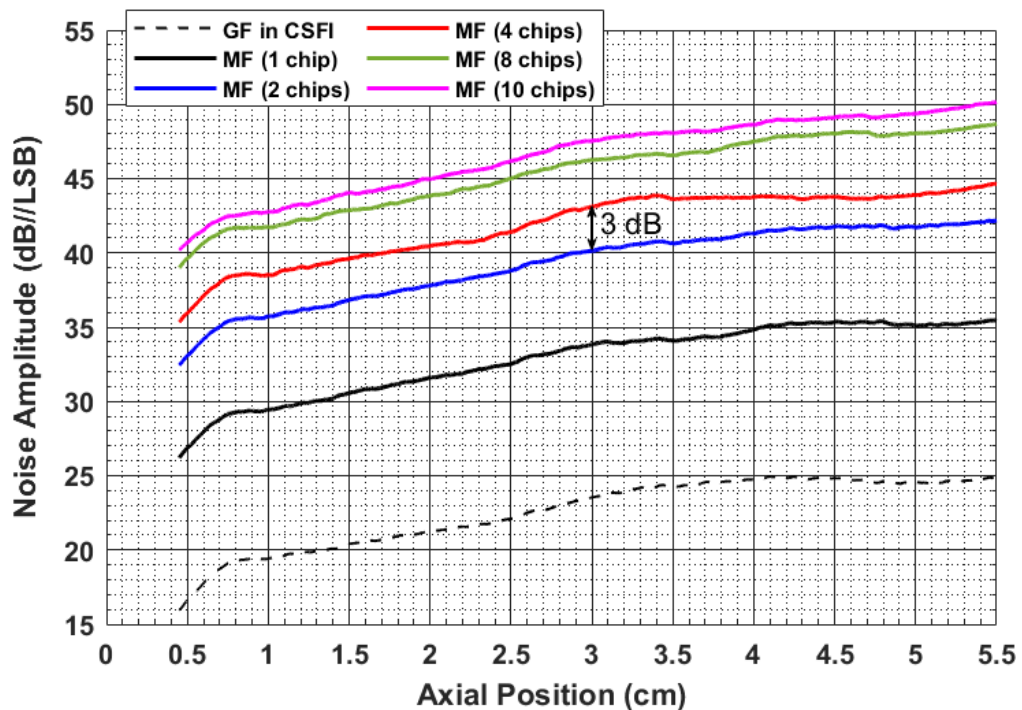


Figure 7.3: Noise amplitude for coded DWI (2, 4, 8 and 10 chips with 2-cycle/chip) with 4 different code lengths. This graph also shows the noise level in CSFI-GF and DWI with pulsed transmission (1-chip). Note that the noise analysis for coded DWI (implemented with MF), and CSFI-GF have different gains. The average noise power is measured over independently taken 13 measurements without any transmission. The received noise amplitude is plotted in dB//LSB. The arrow shows the 3 dB increase in noise when the code length doubles.

7.3 SNR Along the Arcs in Speckle Region

We measured the SNR of 8-bit coded DWI with 1-cycle/chip in the speckle region along the arcs positioned at different ranges to find the optimal virtual source distance. Figure 7.4 shows the SNR level and variation along the arcs at 20, 25, 40, and 50 mm ranges for 10.5 mm virtual source distance. The mean values of the SNR where the measurement variance is relatively high are also shown with

a dotted line in Figure 7.4. We estimated the imaging sector coverage based on the angle at which SNR drops by 3 dB from the mean value.

The imaging sectors are 95° and 90° for the arcs at 20 and 25 mm ranges, when r_v is 10.5 mm. At a 20 mm range distance, a portion of the transmitted energy is wasted due to the five degrees of excess in the imaging sector. Therefore, it is possible to use a larger r_v to insonify the imaging sector at this range adequately. In the deeper regions, e.g., 40 and 50 mm ranges, the imaging sectors are 83° and 81° , respectively. In this case, using a smaller r_v would extend the imaging sector at these regions and provides 90° for the imaging sector. The imaging sector has approximately 88° ($\sim 90^\circ$) -6 dB beamwidth for both 40 and 50 mm ranges, and it is larger than 90° at closer ranges. Similar beamwidth is also obtained when other chip lengths are used in 8-bit coded transmission.

The geometrical divergence sector prediction for 10.5 mm virtual source distance and a 12.8 mm array size (64λ at 7.5 MHz) is $\varphi = 62.7^\circ$ and not 90° . We achieved an approximately 90° imaging sector at all ranges when r_v is 10.5 mm. The difference between the geometrical prediction and the actual (achieved) coverage is due to diffraction and multiple scattering. If only geometrical considerations were used, the required source distance would be 6.4 mm. In this case, the virtual source would be closer to the transducer array surface. 6.4 mm source distance spreads the ultrasonic energy outside the region of interest and causes significant loss in SNR. Confining the insonification to the region of interest improves the SNR significantly.

Adequate insonification of the imaging sector must be considered in conjunction with the penetration depth since there is a trade-off between the SNR level and insonification angle. For example, if a single chip signal were used instead of an 8-bit coded signal, the penetration depth would be much lower, and a long r_v would yield the required beamwidth.

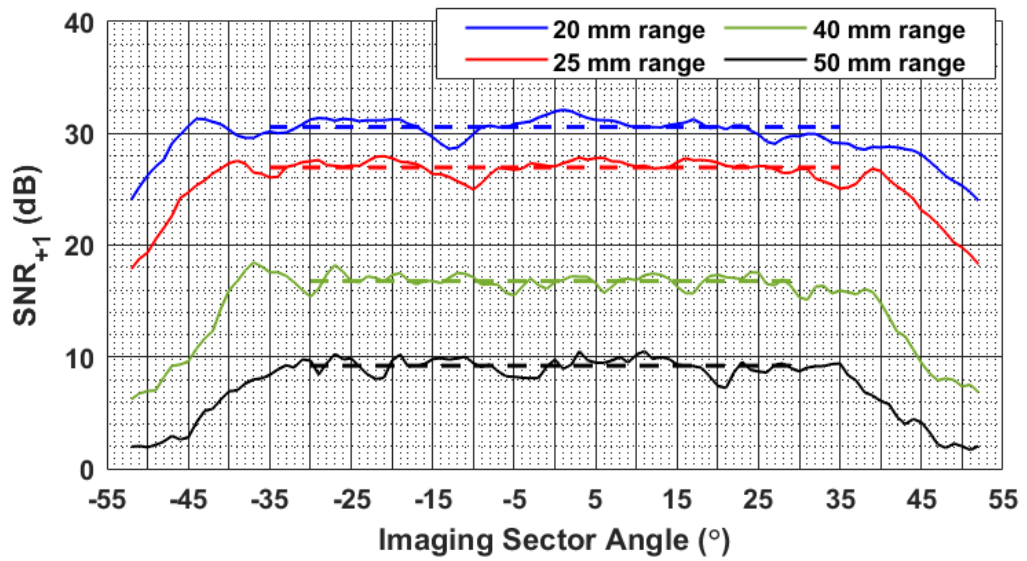


Figure 7.4: SNR of 8-bit coded DWI with 1-cycle/chip along the arcs at 20, 25, 40, and 50 mm ranges when r_v is 10.5 mm. The arcs constitute equidistant imaging points at which the attenuation remains same. The mean SNR values are also plotted with dashed lines where the measurement variance is relatively high.

Chapter 8

Effect of Code Length on SNR

We studied the performance of DWI with different code lengths [69]. We varied the code length from 2-to-10 chips and measured the SNR for a fixed chip signal length, 2-cycle/chip. These coded signals are shown in Figure 5.2. We also measured the SNR for a pulsed transmission, where 1-chip of 2 cycle/chip pulse is used. We compared the measured SNRs of pulsed and coded transmissions with the SNR of the CSFI in which a 2-cycle excitation pulse is used.

8.1 SNR in Speckle

We measured the SNR in the speckle region, which is parallel-hatched in Figure 3.5. The SNR for coded DW transmission with different code lengths when r_v is 14 mm (70λ) is compared with CSFI.

Single-pulse and 2-to-10-bit CGS coded signals are transmitted into the speckle region. The SNR_{+1} is shown in Figure 8.1 as a function of depth. The SNR improves by 3 dB up to 4.5 cm when the code length increases by two folds from 2 to 4 and 4 to 8 bits, which can be observed from inset A. In fact, when the code length is doubled, the speckle amplitude at the correlator output increases by 6 dB, whereas the noise amplitude increases by 3 dB, as shown in Figure 7.3. The SNR is improved by approximately 6 dB up to 4.5 cm depth in a 2-bit coded signal compared to pulsed transmission (see inset A). An additional 3 dB in SNR is due to the two transmissions in 2-bit coded signal. However, the gain in SNR achieved by increased code length decreases beyond 4.5 cm depth.

The SNR of CSFI is maximum at 4 cm depth, which is the transmit focus. The SNR of 8-chip coded DWI is 2 dB lower than that of the CSFI in the focal region. However, the SNR of CSFI deteriorates in non-focal regions. For example, the SNR of the 8-bit Golay coded signal is 8.2 dB larger than that of the CSFI at 2 cm depth.

The 6 dB reference is also shown with a dotted line in Figure 8.1 for penetration depth analysis. The CSFI offers the largest penetration depth, 5 cm, among all schemes. 5 cm is very close to the focus of the CSFI. The penetration depth of 8-bit Golay coded DWI is 4.75 cm, which is very close to that of the CSFI.

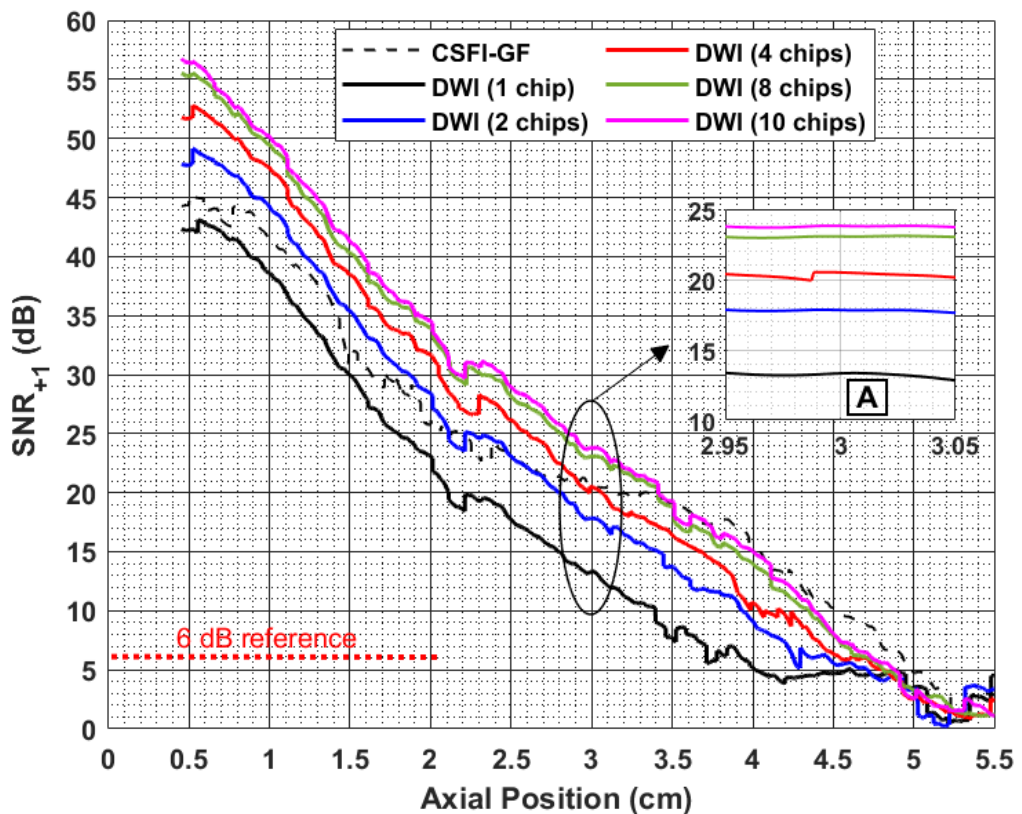


Figure 8.1: SNR_{+1} measurement results in speckle region for 2, 4, 8 and 10-chip coded DWI with 2-cycle/chip. This graph also shows the measurement results for pulsed DWI (1 chip with 2-cycle/chip) and CSFI techniques. 6-dB reference is also plotted with dotted line for penetration depth analysis.

8.2 SNR for Pin Targets

We also measured the SNR at pin targets. The SNR along the horizontally spaced pin targets positioned at 40 mm depth and vertically spaced pin targets are shown in Figure 8.2, respectively.

The SNR of 8-chip coded DWI at the horizontally spaced pin targets is 4 dB less than that of the CSFI in the focal region (center pin), and they are equal at the outermost pins when r_v is 14 mm. If MF is used instead of GF in CSFI, the SNR is further improved by 4 dB. It is evident in Figure 8.2(b) that the coded DWI has a significant SNR advantage over the CSFI in the non-focal region. CSFI-MF maintains up to 4 dB SNR advantage beyond the focal region.

A ninety-fold increase in the frame rate is obtained in DWI due to the ninety times less transmission. Note that there are two transmissions in coded DWI and 181 transmissions in the conventional method.

Theoretically, the SNR gain achieved by matched filtering is expressed as the time-bandwidth product of the signal. The time-bandwidth product of an uncoded signal is in the order of unity [3]. However, the coded signals have larger time-bandwidth products [3], which are equal to code sequence length, N . Therefore, the SNR gain in dB for a code length of N is $10 \times \log_{10}(N)$, if the coded signal is perfectly compressed with a matched filter [24], [28]. We observed that the SNR improves when we increase the code length while the chip signal length is fixed. SNR increases by 3 dB for every doubling of the code length.

The SNR gain in the 2-chip CGS coded signal compared to pulsed excitation (1-chip) is $10 \times \log_{10}(2N)$ [28]. We measured that the SNR improves by 6 dB in 2-chip CGS coded signal compared to pulse transmission. The additional 3 dB in SNR gain is due to the two transmissions in the 2-chip coded signal. The SNR gain obtained from the measured data agrees with the theoretical analysis.

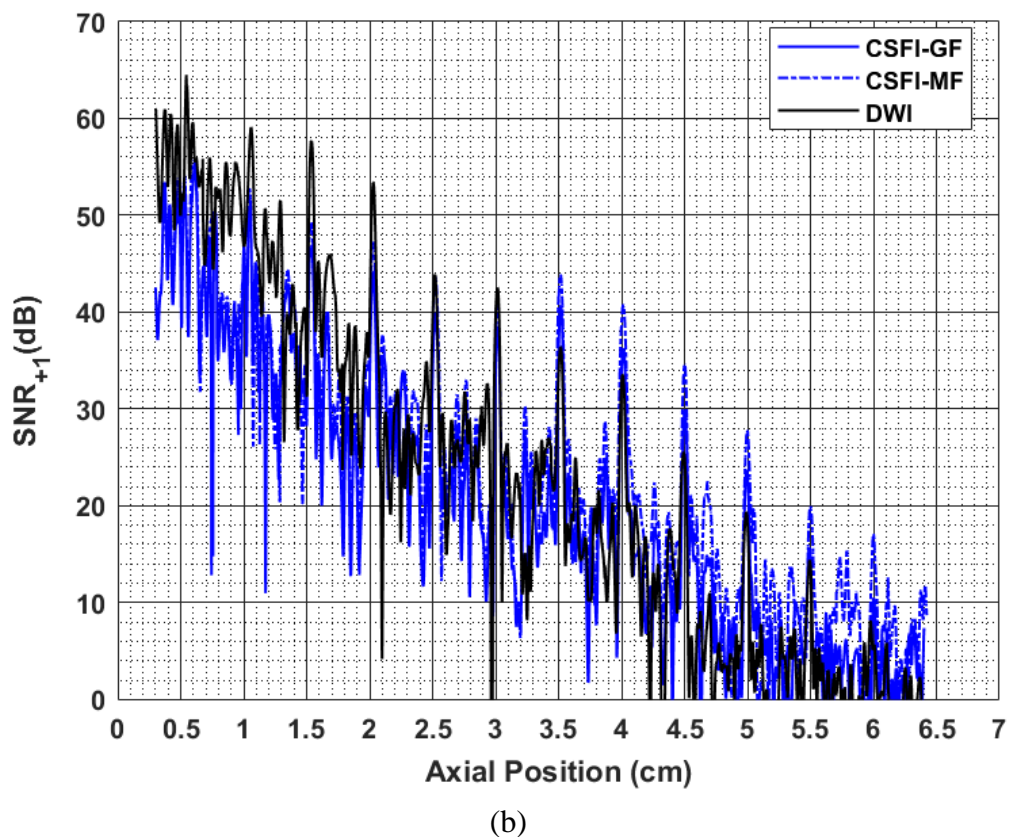
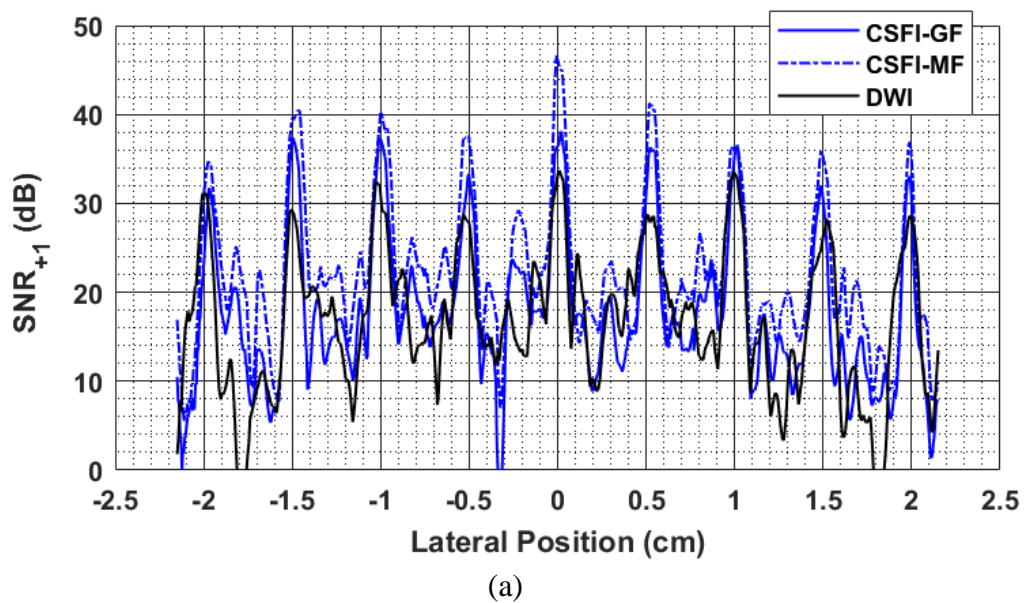


Figure 8.2: SNR for CSFI and coded DWI (8 chips and $r_v = 14$ mm). CSFI-MF is shown for comparison. (a) SNR for horizontally spaced pin targets at 40 mm depth (b) SNR for vertically spaced pin targets.

8.3 Contrast-to-Noise Ratio Comparison

We also used CNR to evaluate the performance of coded DWI. CNR is a quantitative measure to determine the contrast in the ultrasound image. It depends on the mean and variance in the image of the lesion region and the background speckle. We calculated CNR by using the following expression [47], [70]:

$$CNR = \frac{|\mu_C - \mu_B|}{\sqrt{\sigma_C^2 + \sigma_B^2}} \quad (8.1)$$

where $\mu_C, \mu_B, \sigma_C,$ and σ_B are the means and standard deviations of the log-envelope image pixel values of the cyst and background regions, respectively. We used the CNR for the largest anechoic cyst phantom structure for this purpose.

The anechoic cyst targets are encircled with a dashed line in Figure 3.5. The cyst target used for CNR evaluation has a 4 mm diameter and is positioned at 40 mm depth, the focal distance of the CSFI. We calculated the CNR using circular regions in the cystic area and background, as shown in Figure 8.3(b) and Figure 8.3(c). The white circles at the center are in the cyst and the circles at the right-hand side are in the background. A 9 dB correlator gain due to 8-bit code and a 6 dB gain (ideally) due to two transmissions per frame are effective on DWI signal. We subtracted 15 dB from DWI at every pixel. Figure 8.3(a) shows the variation of CNR for CSFI-GF and DWI as the circular area of calculation is increased. We obtained CNR values of 2.3 and 1.6, approximately, for CSFI-GF and coded DWI, respectively. It is possible to calculate CNR reliably when the circular region diameter is between 2.3 mm and 3.1 mm, as shown in Figure 8.3(a). We observed that the CNR of CSFI-MF and CSFI-GF are similar.

Eleven focused and steered transmissions out of 181 transmissions contribute to the image construction of the anechoic cyst in CSFI-GF. However, the same area is reconstructed by two transmissions in DWI. CNR calculation yields

different results in different frames in coded DWI. The cystic region diameter is quite small, and the number of statistically independent pixels contributing to the mean and variance of CNR calculation is limited in a single DWI frame. We made 11 transmissions at different transducer array positions to have statistically independent data suitable to assess the frame-to-frame CNR variation. We moved the array across the phantom surface at 1 mm steps. Figure 8.3(a) shows the mean and the variance of the CNR obtained by coded DWI for 11 independent measurements. We found that the CNR of the coded DWI would be 5.3 if the CNR is calculated by using the combined data of 11 independent measurements.

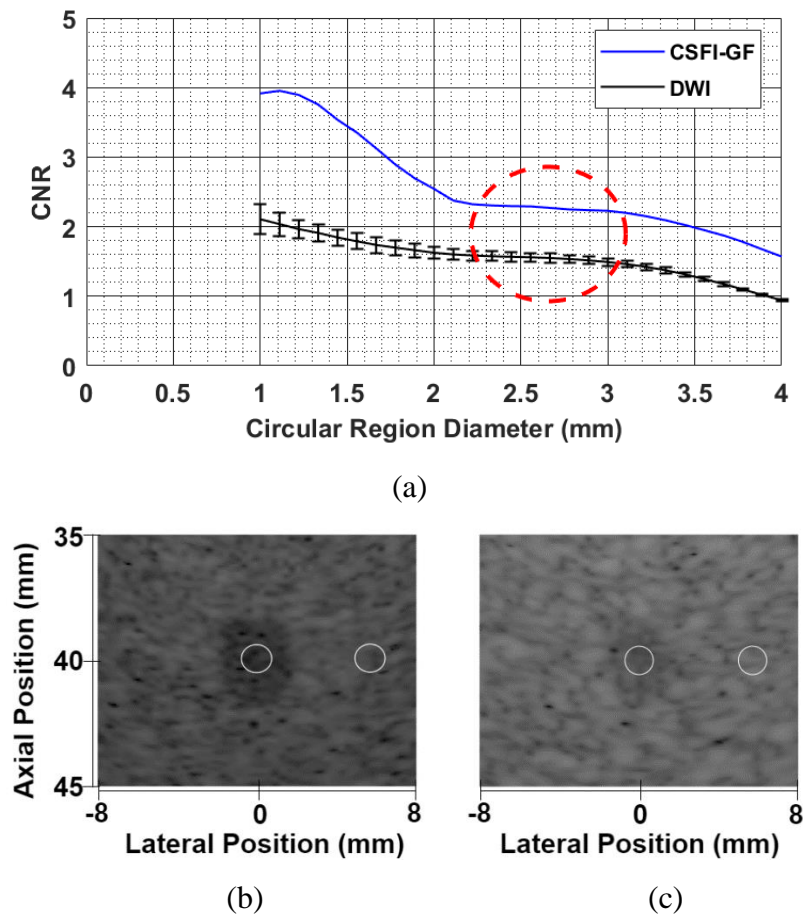


Figure 8.3: CNR for anechoic cyst with 4 mm diameter positioned at 40 mm depth. White circles show the regions where CNR calculations are made. (a) CNR variation against evaluation region size for CSFI-GF and coded DWI. The dashed circle represents the region where the CNR calculation is reliable. The CNR for one frame of the coded DWI varies between 1.05 and 2.04, with 1.6 mean and 0.3 standard deviation. CNR obtained in CSFI image is 2.3. The cyst images obtained by (b) CSFI-GF. (c) Coded DWI when the transducer is at median position.

Chapter 9

Effect of Chip Signal Length on SNR

9.1 SNR in Speckle

We investigated the effect of chip signal length on SNR for coded DWI. We measured SNR in the speckle region of the phantom. Figure 9.1(a) shows the SNR_{+1} as a function of depth, obtained for coded DWI for four different chip signal lengths when r_v is 10.5 mm. 6 dB SNR level is marked to compare the penetration depth of different signals. The penetration depths obtained with 0.5, 1, 1.5, and 2 cycle/chip signals are 5.3, 5.6, 5.3, and 4.8 cm, respectively. The maximum penetration depth is obtained with the 1 cycle/chip signal.

The SNR_{+1} obtained by coded DWI with longer chips is higher at closer depths. For example, the SNR_{+1} of 2-cycles/chip signal is 2 dB, 4.4 dB, and 11.1 dB higher at 1 cm depth than the SNR_{+1} of signals with 1.5, 1, and 0.5 cycle/chip lengths, respectively. This result conforms with the expectation that the correlator output will increase if the signal energy is increased.

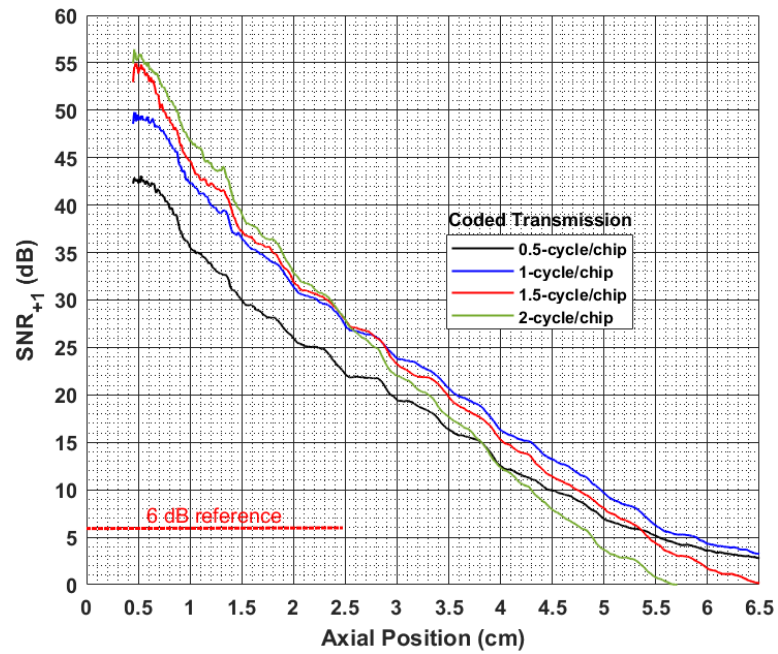
SNR_{+1} difference decreases as the DW propagates and the order among 1, 1.5, and 2 cycle/chip lengths become reversed at about 2.5 cm depth. The coded signal with a 1-cycle/chip has the highest SNR_{+1} beyond 2.5 cm depth. The penetration depth is 8 mm larger than that of the 2-cycle/chip.

This result is counter-intuitive since 1-cycle/chip coded signal has lower energy than 1.5 and 2 cycle/chip signals. More energy leads to SNR improvement

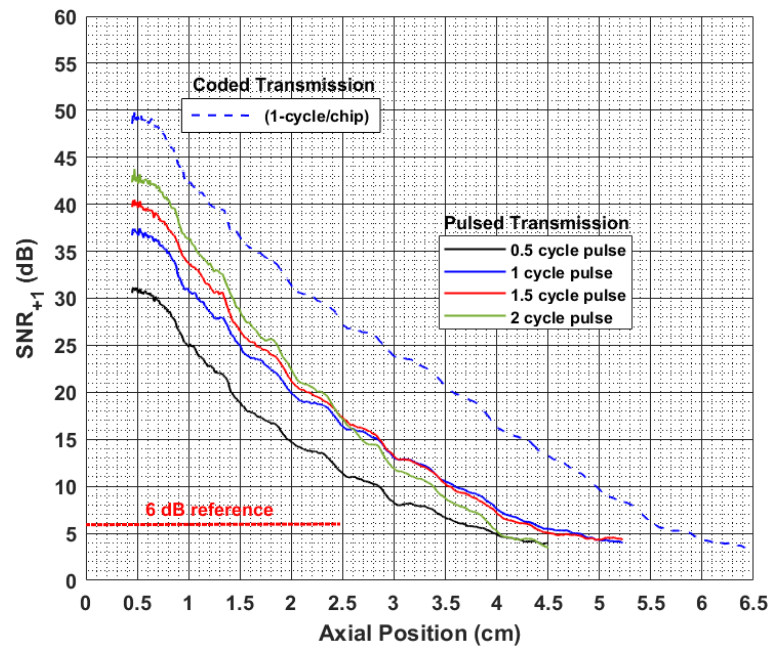
if the transmitted signals are coherently superimposed in the field. However, the coherent addition is not possible in general unless the signals are focused to a particular region. On the other hand, DWI inherently avoids the coherent addition of the transmitted signals in the field, which is more aggravated as the propagation distance increases. The signals with longer chip duration suffer more and undergo the destructive addition of chip signals. Furthermore, the signals scattered in the media interfere with each other at every point in the field. The DW effect favors shorter chip signals for better SNR when combined with propagation in multiple scattering medium.

The shortest chip duration also has a remarkable performance, as shown in Figure 9.1(a). The penetration depth of 0.5 cycle/chip signal is 5.3 cm, which is higher than that of the 2 cycle/chip signal. This signal is the shortest duration signal and has the lowest transmitted pressure amplitude. The SNR difference between this signal and the 1-cycle/chip signal is 6.6 dB at 0.5 cm depth, whereas it is 2.7 dB at 5 cm. Indeed, the received signal amplitude of the 0.5-cycle/chip signal in water is approximately half of the 1-cycle/chip signal because the 67% bandwidth of the transducer transfer function affects the 0.5-cycle signal more [67]. If the driving transmitted energy were the same for 0.5 and 1 cycle/chip signals, the peak amplitude would be approximately 100 V instead of 70 V for 0.5 cycle/chip signal. This equalization would result in a 3 dB increase in SNR and make 0.5 cycle/chip signal best in penetration depth.

Figure 9.1(b) also shows the SNR_{+1} for pulsed DWI with four different pulse lengths when r_v is 10.5 mm. The same dependence of SNR_{+1} to the chip length also exists in uncoded transmission, except the SNR levels are 12 dB lower. The SNR of 1-cycle/chip coded signal is also plotted in Figure 9.1(b) for reference. 3 dB of the difference is due to single transmission in the uncoded case and 9 dB for 8-bit coding (See Chapter VIII). Therefore, it is conjectured that SNR in any linear coding scheme will have a similar dependence on the chip length.



(a)



(b)

Figure 9.1: SNR_{+1} measurement results in speckle region for (a) coded DW transmission (8 chips and $r_v = 10.5$ mm) with 4 different chip lengths and for (b) pulsed DW transmission (1 chip and $r_v = 10.5$ mm) with 4 different pulse lengths. SNR_{+1} for 1-cycle/chip coded signal is also shown for reference. Speckle amplitude is measured over 11 different measurements each yielding statistically independent data. 6-dB reference is also plotted with dotted line for penetration depth analysis.

We show that the 67% two-way transducer bandwidth limits the maximum amplitude, and hence, the received signal's peak power [67]. The received uncoded signals with different durations in freshwater measurement are shown in Figure 9.2. The received 1-cycle signal has a maximum amplitude, which is only 80% of 2-cycle and 1.5-cycle signals. The latter two have the same maximum amplitude since there is sufficient time for the transient to develop. The 0.5-cycle signal suffers the most and remains at 40%. The 0.5-cycle received signal has approximately nine times less energy than the 2-cycle pulse, whereas the ratio of the energies of the respective drive signals is approximately 4-to-1.

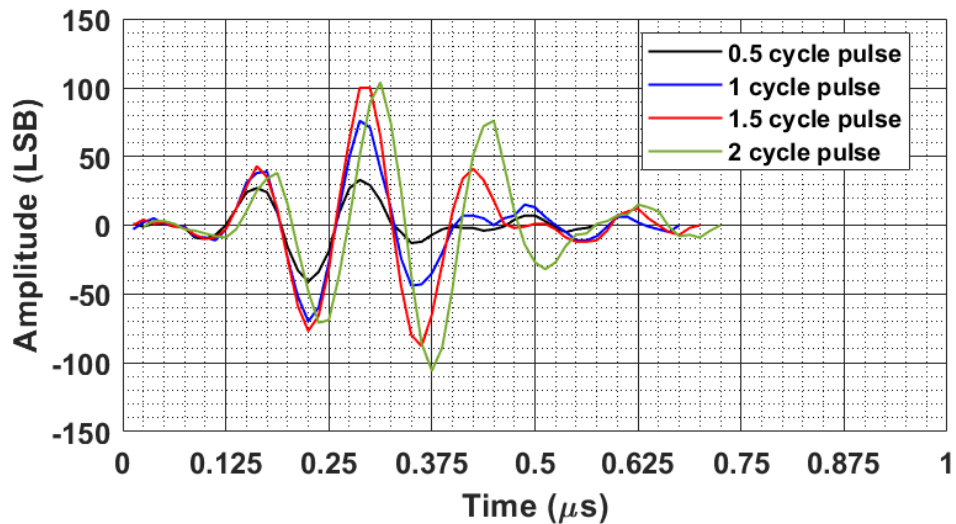


Figure 9.2: The reflected signals with 0.5, 1, 1.5, and 2 cycles from the steel plate in freshwater and received by the 64th element of the phased array transducer.

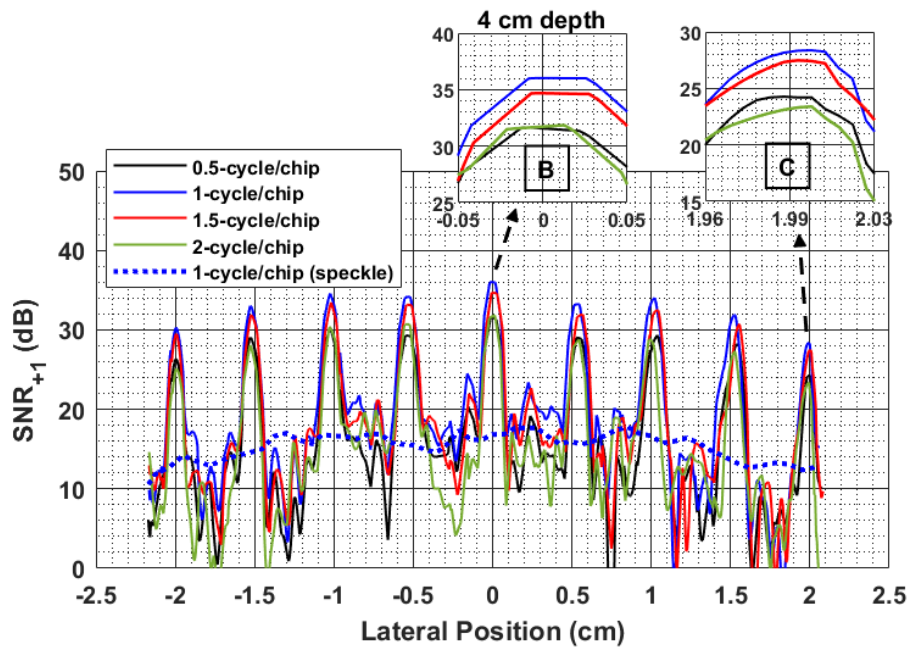
9.2 SNR for Pin Targets

We also measured the SNR_{+1} at pin targets. Figure 9.3(a) shows the SNR_{+1} along the horizontal pin targets positioned at 40 mm depth.

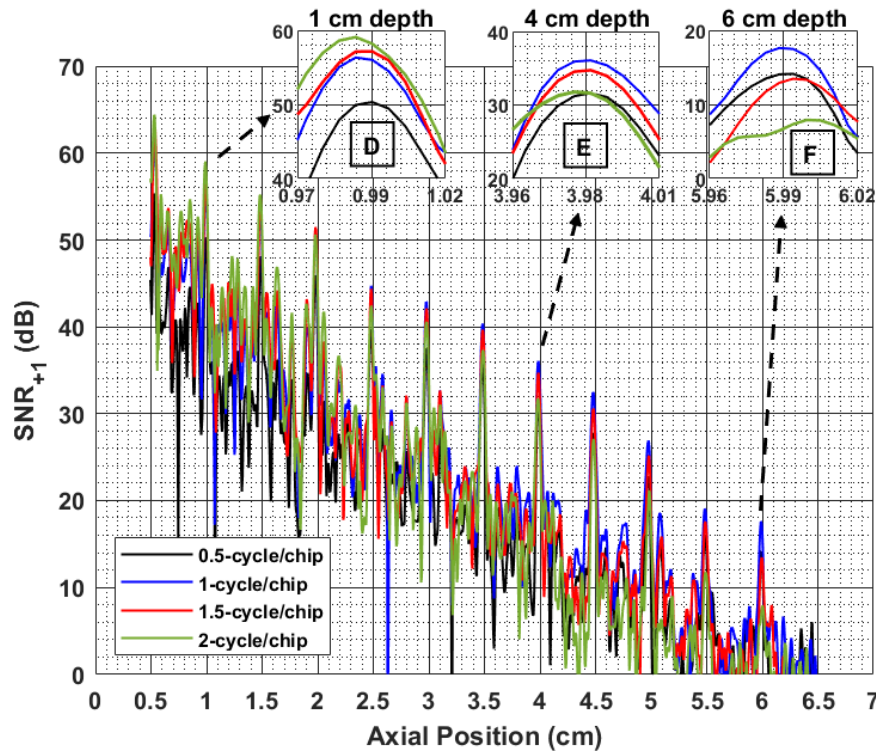
We achieved the maximum SNR_{+1} at the central pin target for all chip signal lengths. The SNR_{+1} of the coded signal with 1-cycle/chip is higher than that of the other coded signals in all horizontal pin targets. For example, it is 4.1 dB higher than that of the coded 2-cycle/chip signal at the central pin target (See Inset B). The SNR_{+1} decreases along the line of horizontal pin targets away from the center for all chip lengths. This decrease is due to the attenuation effect on the increased path length at the outermost pin targets. Nevertheless, the SNR_{+1} of the coded signal with 1-cycle/chip is 5 dB higher than that of the coded signal with 2-cycle/chip (See Inset C).

The speckle level variation between two pin targets is large and not smooth in Figure 9.3 (a). This is because the data had to be taken in a single transducer position in the pin target region. The SNR along the horizontal direction at 40 mm depth measured in the speckle region is also plotted in Figure 9.3 (a) for comparison.

Figure 9.3 (b) depicts the SNR_{+1} variation along the line of vertical pin targets for all chip signal lengths. The variation is similar to the case in the speckle region. At closer depths, SNR is higher when chip length is longer (See Inset D). For depths larger than 2.5 cm, again, the coded signal with 1-cycle/chip offers the maximum SNR (See Insets E and F). The results shown in Figure 9.3 agree with those given in Figure 9.1.



(a)



(b)

Figure 9.3: The SNR_{+1} for coded DWI (8 chips and $r_p = 10.5$ mm) with 4 different chip lengths. (a) SNR_{+1} along the line of horizontal pin targets positioned at 40 mm depth. The SNR_{+1} along the horizontal direction in speckle region is also plotted on the same graph to make a comparison for speckle level variation. (b) SNR_{+1} along the line of vertical pin targets.

Chapter 10

Comparison of Optimized DWI with Conventional Single Focused Imaging

10.1 Noise in CSFI

The noise contribution per transmission is lowest in CSFI-GF, as shown in Figure 7.2. The noise amplitude is approximately 10 dB larger at every depth when MF is employed in CSFI. We calculated the noise contribution in CSFI-MF using a 1-cycle pulse reference signal. Since there is an 8-to-1 energy difference between the CSFI-MF and DWI reference signals, the correlator provides a 9 dB gain to any signal detected using an 8-bit coded reference signal. Two transmissions in the coded DWI add another 3 dB to the noise level. In Figure 7.2, the 12 dB noise level difference between DWI and CSFI-MF is observable. Since the gains are different in each transmission scheme, the noise contributions in the received signals are also different. Therefore, the noise analysis for each scheme is required to obtain an accurate SNR measurement.

10.2 SNR Comparison in the Speckle Region

The SNR_{+1} of the 8-chip coded DWI with 1-cycle/chip is compared to CSFI-GF and CSFI-MF in the speckle region in Figure 10.1. To assess the compensation effect on SNR_{+1} , Figure 10.1 also shows the SNR_{+1} of the coded DWI when the uncompensated two-way transmitted-and-received signal is used as the reference signal in MF. The SNR_{+1} of the coded DWI is 6.5 dB higher than the CSFI-GF up to 3 cm depth. SNR obtained by CSFI-GF is inferior to the coded DWI at all depths, even in the focal region. The SNR values of the coded DWI and CSFI-GF are the same only at the focal depth, which is 4 cm.

Coded DWI also offers better SNR than CSFI-MF up to 3 cm depth. However, the SNR of the latter scheme increases at the focal region and exceeds the SNR of coded DWI, reaching a maximum difference of 7.1 dB. Using MF with CSFI increases the effect of focusing gain, producing the highest SNR in the focal region.

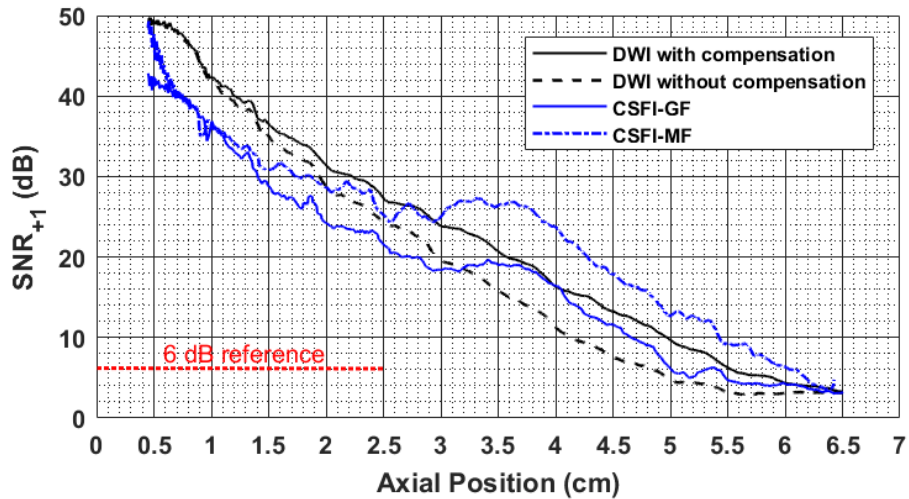


Figure 10.1: Speckle region SNR_{+1} measurement results for CSFI-GF, CSFI-MF and coded DWI (8 chips and $r_v = 10.5$ mm). The maximum SNR is available in the vicinity of the focal region when CSFI-MF is used. In the nonfocal region, the coded DWI offers the highest SNR when attenuation compensation is applied. Note that the coded DWI with compensation offers higher SNR than the uncompensated case, while the results are similar at closer range. A 6-dB reference is plotted with a dotted line for penetration depth analysis.

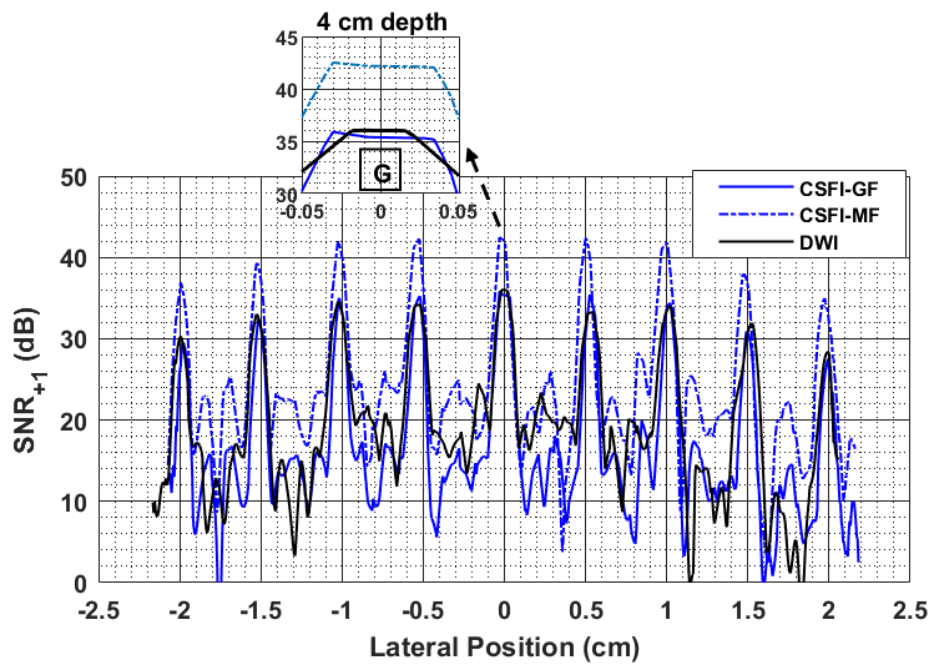
It is clear from Figure 10.1 that the compensation of the reference signal improves the SNR_{+1} of the coded DWI as the depth increases. Compensation gives the same SNR_{+1} as the uncompensated case at lower depths (e.g., 1 cm) because the coded ultrasound beam does not alter significantly due to the attenuation. The effect of compensation becomes very significant at larger depths. For example, the SNR_{+1} of the compensated case is 5 dB larger at a depth of 4 cm. The penetration depth improves by approximately 7 mm (15%).

Figure 10.1 also shows the 6 dB reference for penetration depth. The 8-chip CGS-coded DWI offers a larger penetration depth (5.6 cm) than CSFI-GF. The penetration depth of the CSFI-GF is 5 cm, which is very close to the focus point. The penetration depth of the CSFI-MF (6 cm) is 4 mm larger than that of the coded DWI.

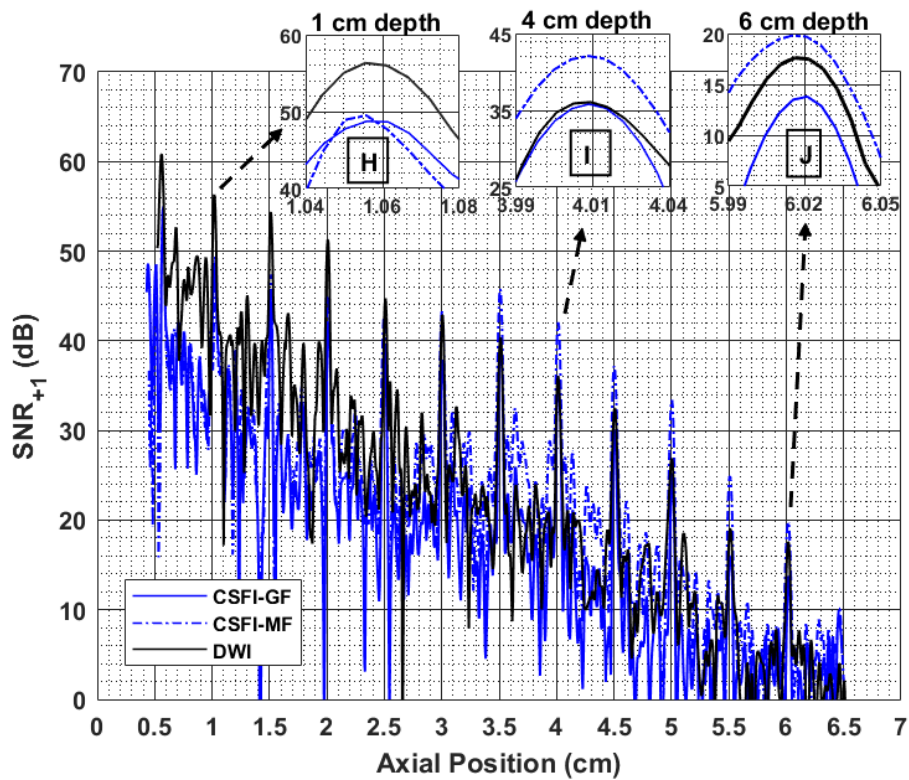
10.3 SNR Comparison in the Pin Target Region

The SNR variation along the horizontal pin targets positioned at 40 mm depth is shown in Figure 10.2(a). The SNRs of the 8-chip coded DWI and CSFI-GF are similar (See Inset G). If MF is used instead of GF in CSFI, the SNR improves by 6-8 dB and exceeds the SNR attained by coded DWI. The SNR of coded DWI is 6.5 dB less at the center pin (See Inset G).

Figure 10.2(b) clearly shows that the coded DWI has a significant SNR advantage over the CSFI-GF in the nonfocal region. For example, it is 7.6 dB larger at 1 cm depth (See Inset H) and 3.8 dB larger at 6 cm depth (See Inset J) compared to CSFI-GF. Coded DWI does not lose its SNR advantage even in the focal region. In the focal region, the CSFI-MF offers 6 dB better SNR than coded DWI (See Inset I). However, the SNR of coded DWI is superior in the nonfocal regions. For example, it exceeds CSFI-MF by 7 dB at 1 cm depth.



(a)



(b)

Figure 10.2: SNR for CSFI and coded DWI (8 chips and $r_p = 10.5$ mm). CSFI-GF and CSFI-MF are shown for comparison. (a) SNR for horizontal pin targets at 40 mm depth (b) SNR for vertical pin targets.

10.4 SSR Comparison

SSR is the ratio between the signal amplitude and the speckle amplitude in a pin target region, where the speckle reduces the perceived resolution of a pin target [71]. We measured the SSR along the vertical line of pin targets. We calculated SSR as the difference between the signal amplitude at the pin targets and the speckle amplitude. Figure 10.3 shows the SSR in DWI, CSFI-GF, and CSFI-MF. SSR in DWI maintains a level of 19 dB between 1.5 cm and 4.5 cm depths. SSR of CSFI is similar to that of the DWI with minor differences.

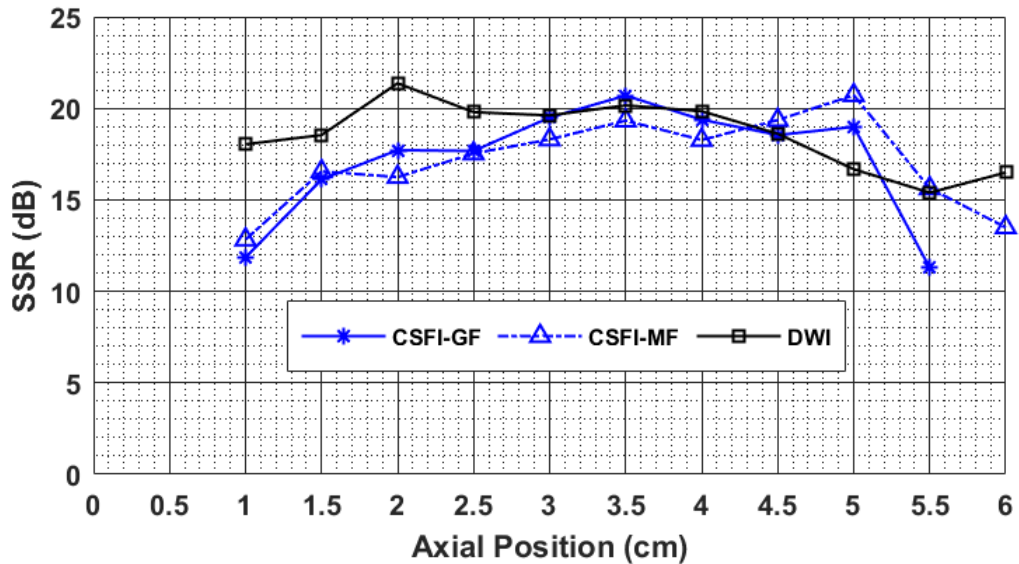


Figure 10.3: SSR of CSFI-GF, CSFI-MF, and coded DWI (8 chips, 1-cycle/chip, and $\tau_v = 10.5$ mm) along the vertical line of pin targets.

The pin targets in the phantom are relatively small and made of monofilament nylon. The pin target radius, a , is 1/8 of the wavelength at the center frequency, 7.5 MHz. The ka is 0.785, where k is the wavenumber. The average ka is even lower for the acoustic pulse in the medium since the acoustic signal energy is dominated by a lower frequency band as the attenuation becomes effective [67]. The nylon pin targets' reflection coefficient leads to a reflected signal amplitude which is 10 dB less than that of steel wire targets [72]. Hence, these pin targets are particularly suitable for SNR and SSR assessment.

Chapter 11

Discussion of Results

11.1 Performance Variation

DW transmission inherently avoids the coherent addition of the transmitted signals while the energy propagates in the medium. Coded signals, however, perform best when the signals are coherently summed up for maximum energy. This contradiction in combining the physics of DWs and the mathematics underlying coded signals manifests itself as maximum SNR is obtained in DWI when the chip signal is as short duration (wideband) as possible.

Short-duration signals have comparatively more energy at lower frequencies [67], which also emerges as an advantage in a multiscattering environment where the attenuation is significant. As the depth increases, energy at lower frequencies prevail, and attenuation compensation is more effective in short-duration signals.

Coded DWI offers approximately 90° imaging sector when virtual source distance, r_v , is 10.5 mm. For this optimum virtual source distance, we compared the SNR performance with respect to the chip duration when the drive voltage amplitude is kept constant. Therefore, the energy of the shorter chip signals is lower. The signal with the shortest duration chip that the transducer can deliver to the medium with adequate peak power provides maximum SNR in DWI despite its lower energy. We used an array with a 67% two-way bandwidth in this work; signals with 1-cycle/chip yield the maximum SNR in coded DWI.

The minimum chip length can be 0.5-cycle, in which case the received signal suffers from the energy due to the two-way transducer transfer function. Despite this energy loss, the coded signal with 0.5 cycle/chip has excellent performance as far as SNR is considered. Consequently, the wider the transducer bandwidth, the higher the SNR.

The temporal resolution is 55.25 frames per second (fps) in CSFI when the image frame is constructed using 181 transmissions. However, we acquired one frame of CGS coded DW data in 200 μ s in this study, which corresponds to 5000 fps. 8-chip coded DWI with 1-cycle/chip provides an approximately 90-fold increase in frame rate without compromising from SNR compared to CSFI even in the focal region.

We employed CGS as a code sequence in this study because these codes do not have any code range lobes. However, they require two transmissions, and the correlation properties of CGS-coded signals deteriorate in attenuating medium. In this respect, we expect that similar performance improvement is possible when other code sequences (e.g., the sequences mentioned in [20-26]) are employed. This issue must be investigated for possible improvements.

11.2 Limitations and Potential Improvements

The performance of coded transmission relies on maintaining a high correlation between the received coded signals and the reference signal. The similarity between the received and the reference signals determines the correlator output. The attenuation compensation increases this similarity, which increases the correlator output. We found out that using an attenuation compensated reference signal significantly improves the SNR. Refinement in the attenuation compensation of the reference signal will further improve the SNR. The effects of multi-layered medium with different attenuation conditions on code range lobes must also be investigated.

We did not use any apodization in this work. Determination and use of appropriate apodization for DWI using optimized pulse length is a potential area for improvement.

The temperature increase at the transducer array surface is one of the main limitations of ultrafast imaging methods such as DWI. The temperature increase at the transducer surface is due to the combination of the power dissipated in the transducer and the absorbed power in the tissue in the vicinity of the contact surface. The average of this power per transmission is proportional to the power delivered to the transducer. Hence, we can compare the temperature increase at the transducer surface in different transmission schemes by comparing the average power delivered to the transducer in each scheme. Simple arithmetic yields the following relative comparison: The transmitted power in 8-bit coded DWI is eight times larger than CSFI per transmission. Note that there are 181 transmissions in one CSFI frame. The transmitted power per frame is equalized if 8-bit coded DWI is operated at 625 fps compared to 55.25 fps maximum temporal resolution of CSFI. Alternatively, 4-bit coded DWI has the same energy per unit of time if operated at 1250 fps, but at the expense of a 3 dB decrease in SNR. This comparison includes the transmitted energy of different transmission scheme-signal length combinations based on simple arithmetic. However, the heating effect of the ultrasonic transmission is important [51], and it must be further investigated.

We collected a large dataset during this study. We deposit all datasets, C++ codes used for DiPhAS programming, and MATLAB codes for post-processing in Bilkent University Institutional Repository.

11.3 Coded Images

We performed a measurement in anechoic targets region. The measurement setup is shown in Figure 11.1(a), where the transducer is positioned to center the cyst

with 3 mm diameter. We presented the ultrasound images of the anechoic cyst targets for CSFI-GF, coded DWI with 1-cycle/chip and 2-cycle/chip in Figure 11.1(b), Figure 11.1(c), and Figure 11.1(d), respectively. The anechoic cyst targets are encircled with a dashed line in Figure 3.5. Each image is normalized with respect to its own maximum [73]. The dynamic range of the displayed images is 45 dB. We complemented the 2.3 dB/cm variable gain to 7.5 dB/cm in post-processing before constructing the images to compensate for the two-way attenuation at the center frequency.

The SNR performances of different imaging settings can be comparatively evaluated at the regions of low SNR, where the signal power is low and noise becomes significant. The image quality is inevitably low in such regions and main problem becomes to detect the presence of various features. The vicinity of the penetration depth is such a region. The anechoic cyst targets are particularly suitable for assessing the SNR and noise-related imaging performance. The signal level in the cyst region is similar to the noise level at low SNR regions, whereas the speckle signal level in the nearby region depends on the depth.

The CSFI-GF image is shown in Figure 11.1(b) as a reference. The focusing gain in the vicinity of the transmit focus at 40 mm depth manifests itself as an increased brightness in the image. The anechoic cysts at 50 mm depth are barely visible since the penetration depth of the CSFI-GF is 50 mm, as shown in Figure 10.1. On the other hand, the anechoic cyst targets at 60 mm depth are not visible.

DWI with 1-cycle/chip is shown in Figure 11.1(c), where the SNR and the penetration depth improvement can be observed. All the anechoic cyst targets up to 50 mm depth are visible, but those at 60 mm depth are barely visible. This result complies with the penetration depth of the coded DWI with 1-cycle/chip, which is 56 mm, as shown in Figure 10.1. Note that the comparison between CSFI-GF and coded DWI is performed on a single frame basis. There are almost 90 times fewer transmission events in DWI compared to CSFI-GF.

When the chip signal duration is increased from 1-cycle to 2-cycle in coded transmission, the penetration depth decreases to 48 mm, as shown in Figure 9.1(a). This decrease is visible in Figure 11.1(d) since the anechoic cyst targets at 50 mm depth are not visible. It is also shown in Figure 9.1(a) that the SNR decreases rapidly down to 0 dB after the penetration depth when coded signal with 2-cycle/chip is transmitted. This decrease appears as the darker region in Figure 11.1(d).

The clarity and definition in all images agree with the quantitative analysis results.

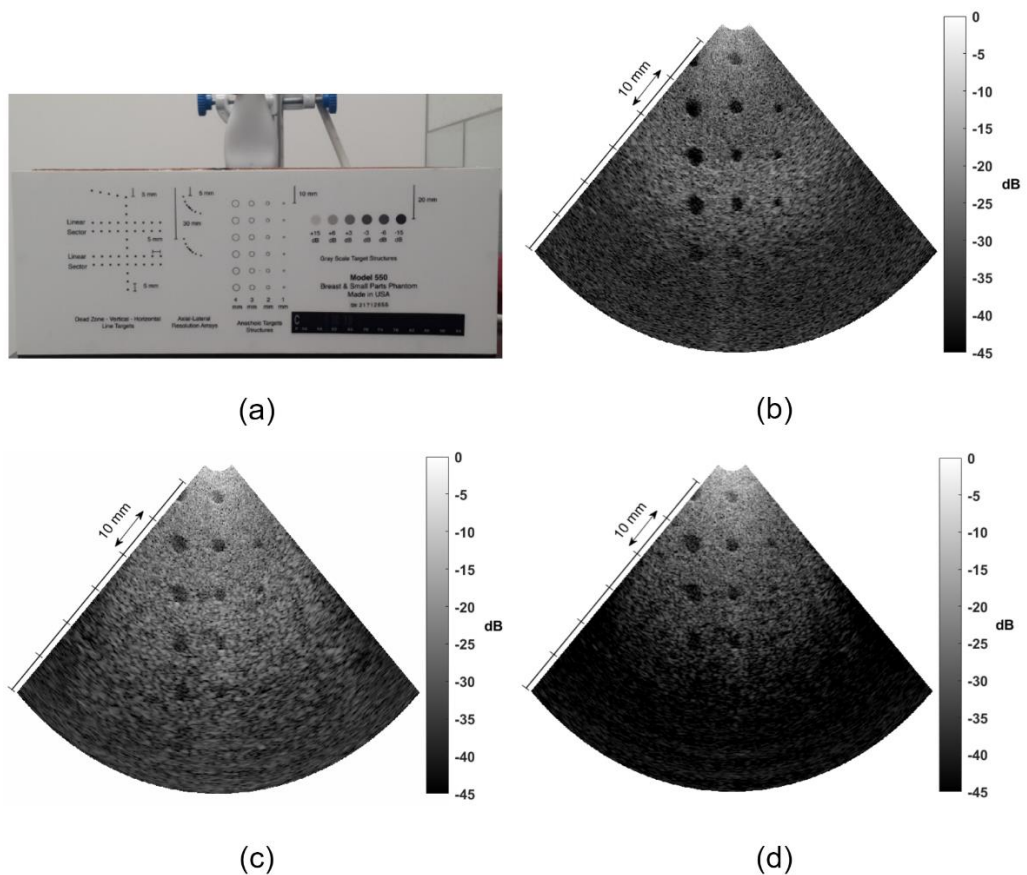


Figure 11.1. Ultrasound images of the anechoic cyst targets. A dynamic range of normalized image intensity values are from 0 to -45 dB. (a) The photo of the measurement setup. (b) CSFI-GF image constructed by 181 focused transmissions. (c) 1-cycle/chip coded DWI image. (d) 2-cycle/chip coded DWI image. Coded DWI images are constructed by using two transmissions (acquired in 200 μ s) and attenuation compensation.

11.4 System Hardware Requirements

The coded excitation is a computationally intensive method and requires a high demand for hardware [3]. Hardware considerations include a correlation receiver and a receive beamformer. For example, 2.198.322 multiplication and 2.190.719 addition per frame are required for each array element in the correlation receiver when 8-bit coded CGS (A) and CGS (B) signals with 1-cycle/chip are processed successively. This much arithmetic operation in 200 μ s is a modest capacity for commercial off-the-shelf (COTS) processors.

Correlation at every array element is inherently parallel, and hence, it can be independently implemented. In receive beamformer, 1.5×10^7 additions are required when beamforming is applied at 117.831 image points. Again, this can also be easily handled by available COTS processors.

Clearly, available COTS computation hardware meets the requirements of a real-time 5000-fps rate.

11.5 Sound Speed Estimation

Medical ultrasound systems generally employ a pre-specified constant sound velocity [74]. However, the sound velocity may significantly vary through the propagation medium, the tissues, ranging from 1400 m/s to 1600 m/s. The mismatch between the actual and assumed sound propagation velocity degrades the beamforming process accuracy, which causes a spatial shift, defocusing, and resolution degradation in ultrasound imaging [75], [76].

Sound velocity determination had been assessed, dating back to World War II for underwater applications. Several equations for sound speed as a function of temperature, salinity, depth, latitude, and pressure were published. Several

researches were carried out to derive simple sound speed equations [77]. An equation, which is a valid reference among underwater acoustics community, is;

$$c = 1449.2 + 4.6 T - 0.055 T^2 + 0.00029 T^3 + (1.34 - 0.010 T)(S - 35) + 0.016 D \quad (11.1)$$

where T is temperature, S is salinity, and d is depth in the ranges of $0 \leq T \leq 35^\circ\text{C}$, $0 \leq S \leq 45 \text{ ppt}$ (parts per thousand) and $0 \leq D \leq 1000 \text{ m}$. This equation gives 1504 m/s as a sound velocity in freshwater.

After World War II, the advent of the ultrasound imaging systems provided further improvements in medical ultrasound. The rapid growth in electronics led to beamforming in medical ultrasound imaging allowing directional transmission and reception. Both pitch-catch and pulse-echo techniques have been employed to measure the sound velocity in medical ultrasound to increase the beamforming efficiency. Similar to those proposed for underwater acoustics, the developments in methods used for accurate sound velocity estimation in medical ultrasound imaging were summarized and discussed in [78].

Several approaches have been used for sound speed estimation in literature, including estimation with a priori knowledge on target [78], estimation without the need of this prior knowledge [79], [80], and estimation with iterative approaches from a set of trial sound velocities [81], [82].

In this study, we used the specified sound velocity, 1450 m/s, in both transmit and receive beamforming. The beamforming imperfections due to the mismatch between 1450 m/s and the actual velocity experienced in our study have the same multiplicative effect to the performance variables. Although our comparative results are independent of the sound speed mismatch, an accurate sound speed estimation would increase the performance of each imaging method individually.

As a future implementation, the approach presented in this study must be handled together with a more accurate sound velocity for possible improvements.

Chapter 12

Conclusion

This study addresses a physical acoustics phenomenon in medical ultrasonic imaging, which has been neither observed nor studied before. The objective of this study is to assess this phenomenon using measurement data.

The research presented in this study focuses on maximizing the SNR of diverging waves in multiple-scattering, attenuating, and diffracting media by proper choice of the burst duration in uncoded transmission or chip signal duration in coded transmission. The main research result is that the SNR improves when the chip signal duration, the modulating pulse in BPSK modulation, is decreased. The SNR at deeper ranges in multiple-scattering, attenuating, and diffracting media ($>2.5\text{cm}$ in this study) increases if the transmitted burst duration or the chip signal duration is reduced when DWs are used. The maximum penetration depth, hence maximum SNR at deeper regions, is obtained when the burst duration corresponds approximately to the inverse of the transducer bandwidth. Consequently, the wider the transducer bandwidth is the higher the SNR.

Furthermore, since SNR is determined by the amount of signal power available in the region of interest, we considered the tradeoff between the SNR and the divergence angle. We determined the optimum DW profile to confine the transmitted ultrasound energy in the imaging sector and thus to contribute to the SNR maximization. We showed that a divergence angle, which is significantly lower than the imaging sector angle, can be used to insonify the entire imaging sector since the ultrasound energy also spreads due to diffraction and multiple

scattering. We found out that a divergence angle of 62° is sufficient to image 90° sector when DWs are used. This divergence angle corresponds to a 10.5 mm virtual source distance.

These results are independent of the type of code sequence employed or whether the transmitted signal is coded or uncoded. We carried out measurements using both coded and pulsed (uncoded) transmissions. SNR obtained by single-pulse transmission is 12 dB lower than 8-bit Golay sequence coded transmission at all depths and for all chip lengths. Using coded transmission increases the SNR everywhere in the region of interest. It enables sufficiently large penetration depth. Therefore, coded transmission enables us to clearly observe the SNR dependence to chip length (from 0.5 cycle upwards). We prefer to code the transmitted signal with CGSs since they offer zero code range lobe.

On the other hand, any code sequences can also be used to increase the SNR in the region of interest. We also used BPSK to modulate the transmitted signal since it supports the complementarity property. The SNR improvement is not limited to using CGSs and BPSK. Any coding sequence used with a linear modulation scheme (e.g., BPSK) provides similar results.

We also investigated the SNR dependence on code length when coded DWs are transmitted through the medium. We made a clear distinction between SNR and SSR, which are commonly confused with each other in literature. We found that SNR improves by 3 dB if the code length is doubled. We also show that this result agrees with the theoretical analysis. Throughout this study, we measured the noise at each channel to assess the SNR reliably.

We used the focal zone of CSFI as a reference in this study. We compared the performances of DWI and CSFI on a single-frame basis. The performance metrics are penetration depth, SNR in speckle, and pin targets, and CNR. We showed that when longer excitation signals are used in CSFI, the SNR in the focal region

increases, unlike the DWI. This is because, the transmitted signals are added constructively in the focal region of CSFI. In other words, the longer the excitation pulse, the higher the SNR in CSFI. We found out that the SNR of the optimized coded diverging wave is higher than that of the conventional single-focused phased array imaging at all depths and regions.

8-chip coded DWI with 1-cycle/chip provides an approximately 90-fold increase in frame rate without compromising from SNR compared to CSFI even in the focal region. This result reveals that DWI enables fast ultrasound imaging, and a 5000 fps rate is possible at the imaging depth of 7.5 cm while improving SNR.

Bibliography

- [1] L. Demi, "Practical guide to ultrasound beamforming: Beam Pattern and image reconstruction analysis," *Applied Sciences*, vol. 8, no. 9, Sep. 2018.
- [2] R. Y. Chiao, X. Hao, "Coded excitation for diagnostic ultrasound: a system developer's perspective," *IEEE Trans. Ultrason., Ferroelectr., Freq. Control*, vol. 52, no. 2, pp. 160-170, Feb. 2005.
- [3] T. Misaridis, J. A. Jensen, "Use of modulated excitation signals in medical ultrasound. Part I: basic concepts and expected benefits," *IEEE Trans. Ultrason., Ferroelectr., Freq. Control*, vol. 52, no. 2, pp. 177-191, Feb. 2005.
- [4] A. Aubry and A. Derode, "Multiple scattering of ultrasound in weakly inhomogeneous media: application to human soft tissues," *J. Acoust. Soc. Am.*, vol. 129, pp. 225-233, 2011.
- [5] E. Badescu et al, "Comparison Between Multiline Transmission and Diverging Wave Imaging: Assessment of Image Quality and Motion Estimation Accuracy," *IEEE Trans. Ultrason., Ferroelectr., Freq. Control*, vol. 66, no. 10, pp. 1560-1572, Oct 2019.
- [6] N. Bottenus, "Comparison of virtual source synthetic aperture beamforming with an element-based model," *J. Acoust. Soc. Am*, vol. 143, no. 5, pp. 2801-2812, 2018.
- [7] K. Kaburaki, M. Mozumi, H. Hasegawa, "Estimation of two-dimensional motion velocity using ultrasonic signals beamformed in cartesian coordinate for measurement of cardiac dynamics," *Japanese Journal of Applied Physics*, vol. 57, April 2018.
- [8] E. Roux, F. Varray, L. Petrusca. et al., "Experimental 3-D Ultrasound Imaging with 2-D Sparse Arrays using Focused and Diverging Waves," *Sci Rep.*, pp. 1-12, June 2018.
- [9] M. Correia, J. Provost, S. Chatelin, O. Villemain, M. Tanter and M. Pernot, "Ultrafast Harmonic Coherent Compound (UHCC) Imaging for High Frame Rate Echocardiography and Shear-Wave Elastography," *IEEE Trans. Ultrason., Ferroelectr., Freq. Control*, no. 3, pp. 420-431, March 2016.
- [10] C. Samson, R. Adamson and J. A. Brown, "Ultrafast Phased-Array Imaging Using Sparse Orthogonal Diverging Waves," *IEEE Trans. Ultrason., Ferroelectr., Freq. Control*, vol. 67, no. 10, pp. 2033-2045, Oct 2020.
- [11] J. Kang, D. Go, I. Song and Y. Yoo, "Wide Field-of-View Ultrafast Curved Array Imaging Using Diverging Waves," *IEEE Transactions on Biomedical Engineering*, vol. 67, no. 6, pp. 638-1649, June 2020.
- [12] D. Posada, J. Porée, A. Pellissier, B. Chayer, F. Tournoux, G. Cloutier, and D. Garcia, "Staggered Multiple-PRF Ultrafast Color Doppler," *IEEE Transactions on Medical Imaging*, vol. 35, no. 6, pp. 1510-1521, June 2016.

- [13] D. T. Blackstock, *Fundamentals of Physical Acoustics*, New York: John Wiley and Sons, 1 ed., 2001.
- [14] D. J. Shull, E. E. Kim, M. F. Hamilton, and E. A. Zabolotskaya, "Diffraction effects in nonlinear Rayleigh wave beams," *J. Acoust. Soc. Am.*, vol. 97, no. 4, pp. 2126-2137, 1995.
- [15] C. Papadacci, M. Pernot, M. Couade, M. Fink, M. Tanter, "High-contrast ultrafast imaging of the heart," *IEEE Trans. Ultrason., Ferroelectr., Freq. Control*, vol. 61, no. 2, pp. 288-301, Feb. 2014.
- [16] H. Hasegawa, H. Kanai, "High frame rate echocardiography using diverging transmit beams and parallel receive beamforming," *J. Med. Ultrason.*, vol. 38, pp. 129-140, May. 2011.
- [17] J. Grondin, V. Sayseng, E. E. Konofagou, "Cardiac strain imaging with coherent compounding of diverging waves," *IEEE Trans. Ultrason., Ferroelectr., Freq. Control*, vol. 64, no. 8, pp. 1212-1222, Aug. 2017.
- [18] J. Porée, D. Posada, A. Hodzic, F. Tournoux, G. Cloutier and D. Garcia, "High-Frame-Rate Echocardiography Using Coherent Compounding With Doppler-Based Motion-Compensation," *IEEE Transactions on Medical Imaging*, vol. 35, no. 7, pp. 1647-1657, July 2016.
- [19] Y. Takeuchi, "An investigation of a spread energy method for medical ultrasound systems-Part one: Theory and investigation," *Ultrasonics*, pp. 175-182, 1979.
- [20] M. O'Donnell, "Coded excitation system for improving the penetration of real-time phased-array imaging systems," *IEEE Trans. Ultrason., Ferroelectr., Freq. Control*, vol. 39, no. 3, pp. 341-351, May 1992.
- [21] K. L. Gammelmark and J. A. Jensen, "Multielement synthetic transmit aperture imaging using temporal encoding," *IEEE Transactions on Medical Imaging*, vol. 22, no. 4, pp. 552-563, April 2003.
- [22] S. Nikolov and J. A. Jensen, "Comparison between different encoding schemes for synthetic aperture imaging," *Medical Imaging 2002: Ultrasonic Imaging and Signal Processing*, vol. 4687, pp. 1-12, 2002.
- [23] A. Lahav, T. Chernyakova, and Y. C. Eldar, "FoCUS: Fourier-Based Coded Ultrasound," *IEEE Trans. Ultrason., Ferroelectr., Freq. Control*, vol. 64, no. 12, pp. 1828-1839, Dec 2017.
- [24] J. Zhao, Y. Wang, J. Yu, T. Li, and Y. P. Zheng, "Feasibility of coded vibration in a vibro-ultrasound system for tissue elasticity measurement," *J. Acoust. Soc. Am.*, vol. 140, no. 1, pp. 35-44, 2016.
- [25] R. Kažys, L. Svilainis, L. Mažeika, "Application of orthogonal ultrasonic signals and binaural processing for imaging of the environment," *Ultrasonics*, vol. 38, no. 1-8, pp. 171-175, 2000.
- [26] J. Shen and E. S. Ebbini, "A new coded-excitation ultrasound imaging system: Part I: Basic principles," *IEEE Trans. Ultrason., Ferroelectr., Freq. Control*, vol. 43, no. 1, pp. 131-140, Jan 1996.

- [27] I. Trots, A. Nowicki, W. Secomski, and J. Litniewski, "Golay sequences—side lobe—cancelling codes for ultrasonography," *Archives of Acoustics*, vol. 29, no. 1, pp. 87-97, 2004.
- [28] X. Wang, J. Yang, J. Ji, Y. Zhang, S. Zhou, "Research on Golay-coded excitation in real-time imaging of high frequency ultrasound biomicroscopy," *Nature*, vol. 11, pp. 1-12, 2021.
- [29] C. Leavens, R. Willams, P. Burns, and M. Sherar, "The use of phase codes in ultrasound imaging: SNR gain and bandwidth requirements,," *Applied Acoustics*, vol. 70, no. 10, pp. 1340-1351, 2009.
- [30] T. Misaridis, J. A. Jensen, "Use of modulated excitation signals in medical ultrasound. Part II: design and performance for medical imaging applications," *IEEE Trans. Ultrason., Ferroelectr., Freq. Control*, vol. 52, no. 2, pp. 192-207, Feb. 2005.
- [31] T. Misaridis, J. A. Jensen, "Use of modulated excitation signals in medical ultrasound. Part III: high frame rate imaging," *IEEE Trans. Ultrason., Ferroelectr., Freq. Control*, vol. 52, no. 2, pp. 208-219, Feb. 2005.
- [32] B. Lashkari, A. Manbachi, A. Mandelis, and R. S. C. Cobbold, "Slow and fast ultrasonic wave detection improvement in human trabecular bones using Golay code modulation," *J. Acoust. Soc. Am*, vol. 132, no. 3, pp. 222-228, 2012.
- [33] F. Zhao, L. Tong, Q. He, J. Luo, "Coded excitation for diverging wave cardiac imaging: a feasibility study," *Phys Med Biol.*, vol. 62, no. 4, pp. 1565-1584, Jan. 2017.
- [34] I. Trots, "Mutually orthogonal golay complementary sequences in synthetic aperture imaging systems," *Archives of Acoustics*, vol. 40, no. 2, pp. 283-289, Apr. 2015.
- [35] F. Zhao, J. Luo, "Diverging wave compounding with spatio-temporal encoding using orthogonal golay pairs for high frame rate imaging," *Ultrasonics*, vol. 89, pp. 155-165, Sep. 2018.
- [36] L. J. Thomas and R. Y. Chiao, "Method and Apparatus for ultrasonic synthetic transmit aperture imaging using orthogonal complementary codes". US Patent 6048315, 11 Apr 2000.
- [37] G. Ping, S. Pengfei, C. Shigao, "Ultrafast synthetic transmit aperture imaging using hadamard-encoded virtual sources with overlapping sub-apertures," *IEEE Trans. Med. Imag.*, vol. 36, no. 6, pp. 1372-1381, June. 2017.
- [38] P. Gong, M. C. Kolios, and Y. Xu, "Delay-encoded transmission and image reconstruction method in synthetic transmit aperture imaging," *IEEE Trans. Ultrason., Ferroelectr., Freq. Control*, vol. 62, no. 10, pp. 1745-1755, October 2015.
- [39] Y. Zhang, Y. Guo and W. Lee, "Ultrafast Ultrasound Imaging With Cascaded Dual-Polarity Waves," *IEEE Transactions on Medical Imaging*, vol. 37, no. 4, pp. 906-917, April 2018.

- [40] Y. Zhang, H. Li and W. -N. Lee, "Imaging Heart Dynamics With Ultrafast Cascaded-Wave Ultrasound," *IEEE Trans. Ultrason., Ferroelectr., Freq. Control*, vol. 66, no. 9, pp. 1465-1479, Sept 2019.
- [41] T. Harrison, A. Sampaleanu, and R. J. Zemp, "S-sequence spatially encoded synthetic aperture ultrasound imaging," *IEEE Trans. Ultrason. Ferroelectr. Freq. Control*, vol. 61, no. 5, pp. 886-890, 2014.
- [42] A. Ramalli, F. Guidi, E. Boni, and P. Tortoli, "A real-time chirp-coded imaging system with tissue attenuation compensation," *Ultrasonics*, vol. 60, pp. 65-75, July 2015.
- [43] J. Kang, Y. Kim, W. Lee and Y. Yoo, "A New Dynamic Complex Baseband Pulse Compression Method for Chirp-Coded Excitation in Medical Ultrasound Imaging," *IEEE Trans. Ultrason., Ferroelectr., Freq. Control*, vol. 64, no. 11, pp. 1698-1710, November 2017.
- [44] Y. Kumru and H. Köymen, "Signal-to-noise ratio of diverging waves in multiscattering media: Effects of signal duration and divergence angle," *The Journal of the Acoustical Society of America*, vol. 151, no. 2, pp. 955-966, 2022.
- [45] J. A. Jensen, "Medical ultrasound imaging," *Progress in Biophysics and Molecular Biology*, vol. 93, no. 1, pp. 153-165, 2007.
- [46] Z. He, F. Zheng, Y. Ma, H. H. Kim, Q. Zhou, and K. K. Shung, "A sidelobe suppressing near-field beamforming approach for ultrasound array imaging," *J. Acoust. Soc. Am*, vol. 137, no. 5, pp. 2785-2790, 2015.
- [47] R. S. C. Cobbold, *Foundations of biomedical ultrasound*, New York: Oxford University Press, 2007, p. 530.
- [48] Y. Kumru, K. Enhoş, H. Köymen, "Pulse coding with complementary Golay sequences for signal to noise ratio improvement in ultrasound mammography," in *Proceedings of Meetings on Acoustics*, 2018.
- [49] C. L. Palmer, B. O. Haugen, E. Tegnander, S. H. Eik-Nes, H. Torp and G. Kiss, "Mobile 3D augmented-reality system for ultrasound applications," in *2015 IEEE International Ultrasonics Symposium (IUS)*, 2015.
- [50] N. M. Tole, *Basic physics of ultrasonographic imaging*, Geneva: World Health Organization, 2005, pp. 22-25.
- [51] G. R. Harris, "Progress in medical ultrasound exposimetry," *IEEE Transactions on Ultrasonics, Ferroelectrics, and Frequency Control*, vol. 52, no. 5, pp. 717-736, May 2005.
- [52] M. Martensson, *Evaluation of Errors and Limitations in Ultrasound Imaging Systems*, PhD Thesis, Royal Institute of Technology, Stockholm, Sweden, 2011.
- [53] "k-Wave: A MATLAB toolbox for the time-domain simulation of acoustic wave fields," [Online]. Available: http://www.k-wave.org/documentation/example_us_bmode_linear_transducer.php. [Accessed 31 January 2022].

- [54] X. Li, "Ultrasound Scan Conversion on TI's C64x+ DSPs," Texas Instruments, Texas, 2009.
- [55] H. Liebgott, R. Prost, and D. Friboulet, "Pre-beamformed RF signal reconstruction in medical ultrasound using compressive sensing," *Ultrasonics*, vol. 53, no. 2, pp. 525-533, 2013.
- [56] B. Carlson, *Communication Systems: an Introduction to Signals and Noise in Electrical Communication*, New York: McGraw-Hill, 1968, p. 495.
- [57] K. F. Üstüner, G. L. Holley, "Ultrasound imaging system performance assessment," Mountain View, CA, USA, 2003.
- [58] "Field II Simulation Program," [Online]. Available: https://field-ii.dk/?examples/cyst_phantom/cyst_phantom.html. [Accessed 1 February 2022].
- [59] "Field II Simulation Program," [Online]. Available: https://field-ii.dk/documents/users_guide.pdf. [Accessed 1 February 2022].
- [60] M. Golay, "Complementary series," *IRE Transactions on Information Theory*, vol. 7, no. 2, pp. 82-87, April 1961.
- [61] D. Z. Dokovic, "Equivalence classes and representatives of Golay sequences," *Discrete Math*, vol. 189, pp. 79-93, July. 1998.
- [62] E. Kalashnikov, "An Introduction to Golay Complementary Sequences," *Eureka*, vol. 4, no. 1, pp. 40-48, 2014.
- [63] S. Kounias, C. Koukouvinos, K. Sotirakoglou, "On Golay sequences," *Discrete Mathematics*, vol. 92, no. 1-3, pp. 177-185, January 1991.
- [64] P. Fan, W. Yuan, and Y. Tu, "Z-complementary Binary Sequences," *IEEE Signal Processing Letters*, vol. 14, no. 8, pp. 509-512, August 2007.
- [65] U. Madhow, *Fundamentals of digital communication*, New York, USA: Cambridge University, 2008, p. 55.
- [66] J. G. Proakis, *Digital Communications*, Fourth ed., New York: McGraw-Hill, 2001, p. 234.
- [67] Y. Kumru, H. Köymen, "Ultrasonic array characterization in multiscattering and attenuating media using pin targets," arxiv, 2021.
- [68] H. Eriksson, P. O. Borjesson, P. Odling and N. Holmer, "A robust correlation receiver for distance estimation," *IEEE Trans. Ultrason., Ferroelectr., Freq. Control*, vol. 41, no. 5, pp. 596-603, Sept. 1994.
- [69] Y. Kumru, H. Köymen, "Coded Divergent Waves for Fast Ultrasonic Imaging: Optimization and Comparative Performance Analysis," arXiv:2104.10526, 2021.
- [70] K. F. Üstüner, G. L. Holley, "Ultrasound imaging system performance assessment," Mountain View, CA, USA, 2003.
- [71] D. Hyun, L. L. Brickson, K. T. Looby, and J. J. Dahl, "Beamforming and Speckle Reduction Using Neural Networks," *IEEE Transactions on Ultrasonics, Ferroelectrics, and Frequency Control*, vol. 66, no. 5, pp. 898-910, 2019.

- [72] W. G. Neubauer, *Underwater Acoustic Reflection from Surfaces and Shapes*, Peninsula Publishing, 2017, pp. 225-233.
- [73] L. Demi, M. Demi, R. Prediletto, and G. Soldati, "Real-time multi-frequency ultrasound imaging for quantitative lung ultrasound-first clinical results," *J. Acoust. Soc. Am.*, vol. 148, pp. 998-1006, 2020.
- [74] P. N. T. Wells, *Biomedical Ultrasonics*, London: Academic Press, 1977.
- [75] H. C. Shin, R. Prager, H. Gomersall, N. Kingsbury, G. Treece, A. Gee, "Estimation of average speed of sound using deconvolution of medical ultrasound data," *Ultrasound Med Biol*, vol. 36, no. 4, pp. 623-636, April 2010.
- [76] J. F. Krucker, J. B. Fowlkes and P. L. Carson, "Sound speed estimation using automatic ultrasound image registration," *IEEE Transactions on Ultrasonics, Ferroelectrics, and Frequency Control*, vol. 51, no. 9, pp. 1095-1106, Sept 2004.
- [77] K. V. Mackenzie, "Discussion of sea water sound-speed determinations," *The Journal of the Acoustical Society of America*, vol. 70, pp. 801-806, 1981.
- [78] D. E. Robinson, J. Ophir, L. S. Wilson, and C. F. Chen, "Pulse-echo ultrasound speed measurements: Progress and prospects," *Ultrasound in Medicine & Biology*, vol. 17, no. 6, pp. 633-646, 1991.
- [79] M. E. Anderson and G. E. Trahey, "The direct estimation of sound speed using pulse-echo ultrasound," *J Acoust Soc Am*, vol. 104, no. 5, pp. 3099-3106, 1998.
- [80] F. R. Pereira, J. C. Machado and W. C. Pereira, "Ultrasonic wave speed measurement using the time-delay profile of rf-backscattered signals: simulation and experimental results," *J Acoust Soc Am*, vol. 111, no. 3, pp. 1445-1453, 2002.
- [81] D. Napolitano, C. H. Chou, G. McLaughlin, T. L. Ji, L. Mo, D. DeBusschere and R. Steins, "Sound speed correction in ultrasound imaging," *Ultrasonics*, vol. 44, pp. 43-46, 2006.
- [82] X. Qu, T. Azuma, J. T. Liang and Y. Nakajima, "Average sound speed estimation using speckle analysis of medical ultrasound data," *Int J Comput Assist Radiol Surg*, vol. 7, no. 6, pp. 891-899, 2012.
- [83] A. Cigier, F. Varray and D. Garcia "SIMUS: an open-source simulator for ultrasound imaging. Part II: comparison with three popular simulators," arXiv:2103.05521, 2021.

Appendix A

Measurement Protocols

A.1 Phantom Measurement Protocol for DWI

1. Design the coded or pulsed transmit waveform in MATLAB Simulink using pulse width modulation at 480 MHz sampling rate.
2. Place the transducer array on the phantom region where data is collected. Connect the transducer array connector to the ultrasound scanner. Check all the device connections.
3. Adjust the time delays applied to each transducer array element to form the desired diverging wave profile.
4. Adjust the transmit phase length based on the transmit signal duration and maximum time delay.
5. Adjust the receive phase length (record length) based on the sound speed and the maximum depth of interest.
6. Adjust the time gain compensation based on the nominal phantom attenuation.
7. Adjust the driving voltage amplitude.
8. Specify a destination folder where the received data will be saved and give a specific name for the data to be saved.
9. Transmit the pulse width modulated signal and receive at 80 MHz sampling rate using all transducer array elements.
10. Check if the received data is recorded to the destination folder.
11. Record the room and phantom temperature.
12. Repeat all the procedures for CGS(A) and CGS(B) coded signals. If a pulsed transmission is used, a single transmit-receive event is sufficient.

13. Move the transducer by 1 mm and repeat the procedures described above at least 11 times if the region is a speckle region. In other regions, a single transmit-receive event is sufficient.

A.2 Phantom Measurement Protocol for CSFI

1. Design the pulsed transmit waveform in MATLAB Simulink using pulse width modulation at 480 MHz sampling rate.
2. Place the transducer array on the phantom region where data is collected. Connect the transducer array connector to the ultrasound scanner. Check all the device connections.
3. Adjust the time delays applied to each transducer array element to form the desired focused and steered beam transmission required in CSFI.
4. Adjust the transmit phase length based on the transmit signal duration and maximum time delay.
5. Adjust the receive phase length (record length) based on the sound speed and the maximum depth of interest.
6. Adjust the time gain compensation based on the nominal phantom attenuation.
7. Adjust the driving voltage amplitude.
8. Specify a destination folder where the received data will be saved and give a specific name for the data to be saved.
9. Transmit the pulse width modulated signal and receive at 80 MHz sampling rate using all transducer array elements.
10. Check if the received data is recorded to the destination folder.
11. Record the room and phantom temperature.
12. Repeat the procedures described above for a different steering direction by updating the time delays applied to each array element until the entire region of interest is scanned.

A.3 Freshwater Measurement Protocol

1. Fill the water tank with freshwater, immerse a steel plate at a depth of approximately 5 cm, and place the transducer array looking downwards. Check all the device connections.
2. Design the coded or pulsed transmit waveform in MATLAB Simulink using pulse width modulation at 480 MHz sampling rate.
3. Adjust the transmit phase length based on the transmit signal duration.
4. Adjust the receive phase length (record length) based on the sound speed and the maximum depth of interest.
5. Adjust the time gain compensation to be very small due to negligible freshwater attenuation.
6. Adjust the driving voltage amplitude.
7. Specify a destination folder where the received data will be saved and give a specific name for the data to be saved.
8. Transmit the pulse width modulated signal using the mid-element of the transducer array.
9. Receive at 80 MHz sampling rate using all transducer array elements.
10. Check if the received data is recorded to the destination folder.
11. Record the room and freshwater temperature.
12. Repeat the procedures described above for CGS(A) and CGS(B) coded signals. If a pulsed transmission is used, a single transmit-receive event is sufficient.

A.4 Noise Measurement Protocol

1. Place the transducer array on the speckle phantom region where the noise data is collected. Connect the transducer array connector to the ultrasound scanner. Check all the device connections.
2. Adjust the receive phase length (record length) and time gain compensation such that they are the same as those used for speckle or signal measurements.
3. Set the driving voltage amplitude to 0 Volt.
4. Specify a destination folder where the received noise data will be saved and give a specific name for the data to be saved.
5. Record the noise data without any transmission.
6. Check if the received noise data is recorded to the destination folder.
7. Record the room and phantom temperature.
8. Repeat the procedures described above at least 13 times to collect statistically independent noise data.

Appendix B

Analytical Expression for Pressure

B.1 Derivation for Non-Attenuating Medium

In our efforts to estimate the pressure at the field point and the received signal, we first derived the analytical expression for the pressure field generated in a non-attenuating medium. We considered an unapodized array of equally spaced point sources and cylindrical spreading in this derivation.

The pressure generated at the field point by the i th element of the transducer array is

$$P_i(\omega, t, r, \theta) = \frac{A}{\sqrt{r_i}} e^{j(\omega t - kr_i + \varphi_i)} \quad (\text{B.1})$$

$$r_i = \sqrt{r^2 + (n_i \Delta x)^2 - [2 r n_i \Delta x \cos(\theta)]} \quad (\text{B.2})$$

where r_i is calculated by using the cosine theorem as in Eq. (B.2). It is the distance between the i th element and the field point, the product of $n_i \Delta x$ is the distance between the i th element and the mid-element (64th element) of the transducer array, r is the distance from the mid-element to the field point, k is the wavenumber, ω is the angular frequency, φ_i is the externally applied phase delays to form a desired beam transmission and θ is the angle between the array surface and the \vec{r} .

We now calculate the pressure from a pair of point sources at the field point, each radiating as in Eq. (B.1):

$$P_{tot}(\omega, t, r, \theta) = \sum_{i=1}^{128} \frac{A}{\sqrt{r_i}} e^{j(\omega t - kr_i + \varphi_i)} \quad (\text{B.3})$$

Substituting Eq. (B.2) into Eq.(B.3) yields

$$P_{tot}(\omega, t, r, \theta) = \sum_{i=1}^{128} \frac{A}{\sqrt[4]{r^2 + (n_i \Delta x)^2 - [2 r n_i \Delta x \cos(\theta)]}} e^{j(\omega t - k\sqrt{r^2 + (n_i \Delta x)^2 - [2 r n_i \Delta x \cos(\theta)]} + \varphi_i)} \quad (\text{B.4})$$

Using the Taylor series expansion for r_i , which are expressed in Eq. (B.6),

$$P_{tot}(\omega, t, r, \theta) = \sum_{i=1}^{128} \frac{A}{\sqrt{r} \left[1 + \frac{1}{4} \left(\frac{n_i \Delta x}{r} \right)^2 - \frac{1}{2} \frac{n_i \Delta x}{r} \cos(\theta) \right]} e^{j \left\{ \omega t - kr \left[1 + \frac{1}{2} \left(\frac{n_i \Delta x}{r} \right)^2 - \frac{n_i \Delta x}{r} \cos(\theta) \right] + \varphi_i \right\}} \quad (\text{B.5})$$

The pressure in Eq.(B.3) can be written as in Eq.(B.6)

$$\sqrt[2]{1 + \left(\frac{n_i \Delta x}{r} \right)^2 - 2 \frac{n_i \Delta x}{r} \cos(\theta)} \approx 1 + \frac{1}{2} \left(\frac{n_i \Delta x}{r} \right)^2 - \frac{n_i \Delta x}{r} \cos(\theta) \quad (\text{B.6})$$

$$\sqrt[4]{1 + \left(\frac{n_i \Delta x}{r} \right)^2 - 2 \frac{n_i \Delta x}{r} \cos(\theta)} \approx 1 + \frac{1}{4} \left(\frac{n_i \Delta x}{r} \right)^2 - \frac{1}{2} \frac{n_i \Delta x}{r} \cos(\theta)$$

For an arbitrary excitation signal, $s(t)$, the total pressure generated at the field point can be written as in Eq.(B.7), where $P_{tot}(\omega, r, \theta)$ is the phasor of the pressure and $S(\omega)$ is the excitation signal in frequency domain. Note that the phase delays, φ_i , are represented as Δt_i in time domain.

$$F^{-1}\{P_{tot}(\omega, r, \theta) S(\omega)\} = \sum_{i=1}^{128} \frac{A}{\sqrt{r} \left[1 + \frac{1}{4} \left(\frac{n_i \Delta x}{r}\right)^2 - \frac{1}{2} \frac{n_i \Delta x}{r} \cos(\theta)\right]} s\left(t - \left(\frac{r - n_i \Delta x \cos(\theta)}{c_0} + \frac{(n_i \Delta x)^2}{2rc_0}\right) + \Delta t_i\right) \quad (\text{B.7})$$

B.2 Derivation for Attenuating Medium

In the presence of attenuation, the analytical expression derived for the pressure in non-attenuating medium shown in Eq.(B.3)(4.1) extends to Eq. (B.8), where the exponential term with the attenuation coefficient, α , represents the attenuation.

$$P_{tot}(\omega, t, r, \theta) = \sum_{i=1}^{128} \frac{A}{\sqrt{r_i}} e^{j(\omega t - kr_i + \phi_i)} e^{-\alpha f r_i} \quad (\text{B.8})$$

Using the similar approach described in Appendix B.1 results in the total pressure field in an attenuating medium,

$$F^{-1}\{P_{tot}(\omega, r, \theta) S(\omega)\} = \sum_{i=1}^{128} \frac{A e^{-\alpha f r} \left[1 + \frac{1}{2} \left(\frac{n_i \Delta x}{r}\right)^2 - \frac{n_i \Delta x}{r} \cos(\theta)\right]}{\sqrt{r} \left[1 + \frac{1}{4} \left(\frac{n_i \Delta x}{r}\right)^2 - \frac{1}{2} \frac{n_i \Delta x}{r} \cos(\theta)\right]} s\left(t - \left(\frac{r - n_i \Delta x \cos(\theta)}{c_0} + \frac{(n_i \Delta x)^2}{2rc_0}\right) + \Delta t_i\right) \quad (\text{B.9})$$

Appendix C

Characterization of the Phased Array Transducer used in the Measurements

C.1 Transducer Diagram for Transmission and Reception

The pulse-echo measurements detailed in this appendix allow us to measure the bandwidth and the two-way response of the transducer for various input pulse waveforms. For this purpose, we performed measurements in freshwater using the measurement setup shown in Figure 6.1. Figure C.1 shows the transmit and receive transducer diagram. The reflected pressure at the i th element surface is approximately given as

$$P_{RX,i}(r; \omega) \approx \left(\frac{P_{TX,i}(\omega)}{\sqrt{r}} e^{-jkr} \right) \Gamma(\omega) \left(\frac{1}{\sqrt{r}} e^{-jkr} \right) \quad (\text{C.1})$$

where, the subscripts TX and RX represent the transmission and reception. i represents the transducer array element, and it is 64. The first term on the right-hand side expresses the pressure field at the field point. $\Gamma(\omega)$ is the reflection coefficient of the target. The last term accounts for the propagation from target to the array element. Here, the return path is approximately 10 cm, i.e., $r \approx 5$ cm, and the propagation is cylindrical. The pressure reflection coefficient at the steel plate surface is taken as unity (impedance mismatch is 1.5 MRayls to 44 MRayls) and the pressure phasor on the element surface during transmission is given as

$$P_{TX,i}(\omega) = H_{TX,i}(\omega) V_{TX}(\omega) \quad (C.2)$$

where $H_{TX,i}(\omega)$ is the forward electromechanical transfer function of the i th transducer element in a rigid baffle, and $V_{TX}(\omega)$ is the Fourier transform of the voltage waveform used for transmission. The received signal is then given by

$$s_{RX,i}(t) = F^{-1}\{H_{RX,i}(\omega) P_{RX,i}(r; \omega)\} \quad (C.3)$$

where $H_{RX,i}(\omega)$ is the backward transfer function of the i th transducer element. $s_{RX,i}(t)$ is measured at the receiver ADC output in units of LSB.

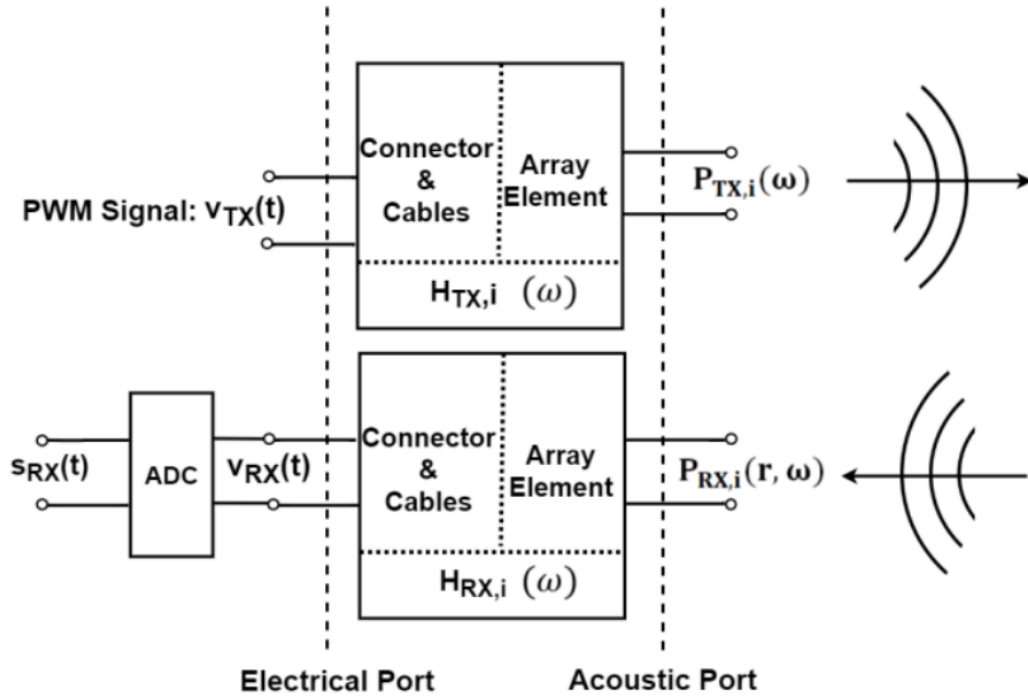


Figure C.1: The transmit and receive diagram of the phased array transducer used in this study.

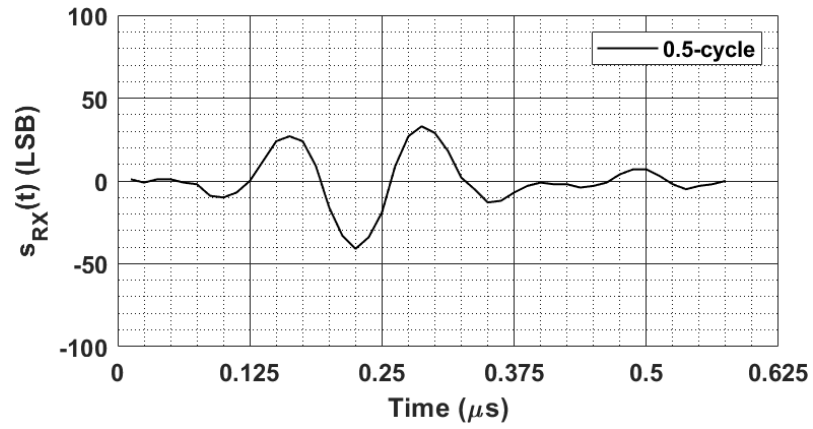
C.2 Comparison of the Measured Data and the Data Provided by the Transducer Manufacturer

We characterized the ultrasound imaging transducer array by measuring the array element transfer function. For this purpose, we transmitted a 0.5-cycle signal. Using the set-up shown in Fig. 3(a), we applied ± 70 V pulse to an array element when all other elements were undriven. Then, we measured the reflected signal at the electrical terminals of the same element. Figure C.2 shows the received signal at the 64th element together with its spectrum. This signal includes cumulative effects of the connector, cables, all matching circuits in the transducer assembly. The 3 dB bandwidth of the received signal is less than 5 MHz and is well within the drive signal bandwidth. The transducer two-way electromechanical transfer function determines the acoustic signal bandwidth. The two-way transfer function, $H_2(\omega)$, is given as

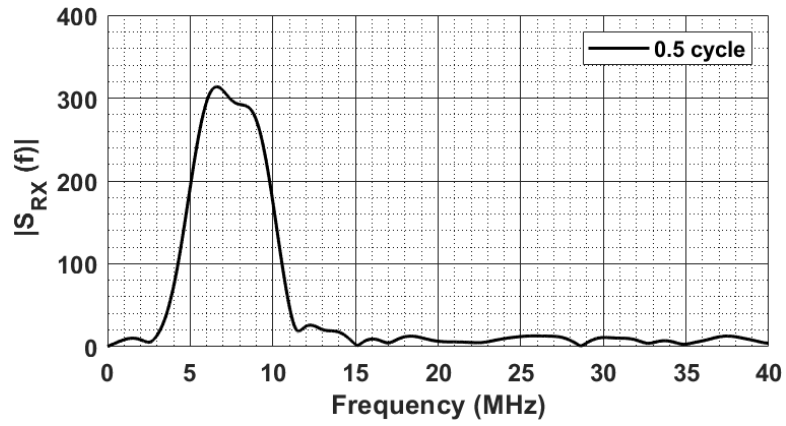
$$H_2(\omega) = H_{RX,i}(\omega) H_{TX,i}(\omega) \quad (\text{C.4})$$

The measured two-way transfer function, from electrical input to received signal at the same terminal, is shown in Figure C.3. The ratio between the frequency responses of the received and the transmitted signals yields the two-way transfer function of that terminal. The 3 dB bandwidth of this element is 4.5 MHz, between 9.92 MHz and 5.37 MHz. The measured fractional bandwidth is approximately 67% for a single transducer array element.

The empirical observation obtained in measurements agrees with the data provided by the transducer manufacturer given in Figure C.4.



(a)



(b)

Figure C.2: Fresh-water measurement result. Only the 64th element of the transducer array is fired. 0.5-cycle pulse is transmitted. All the elements receive the echo signal. (a) Received signal at the 64th element, $s_{RX}(t)$. (b) The frequency spectrum of this received signal, $S_{RX}(f)$.

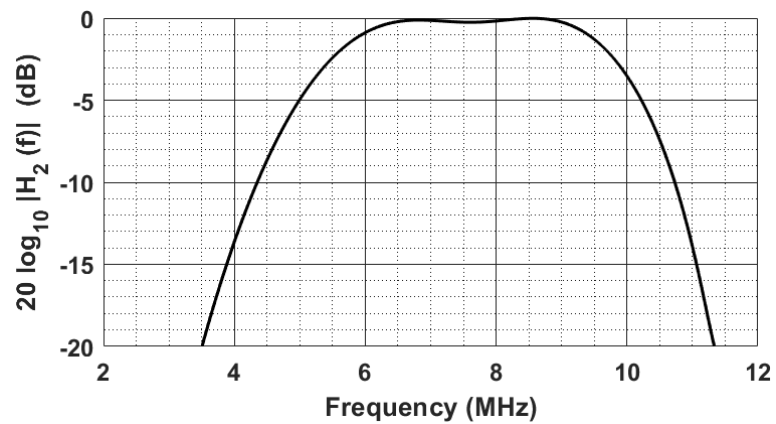
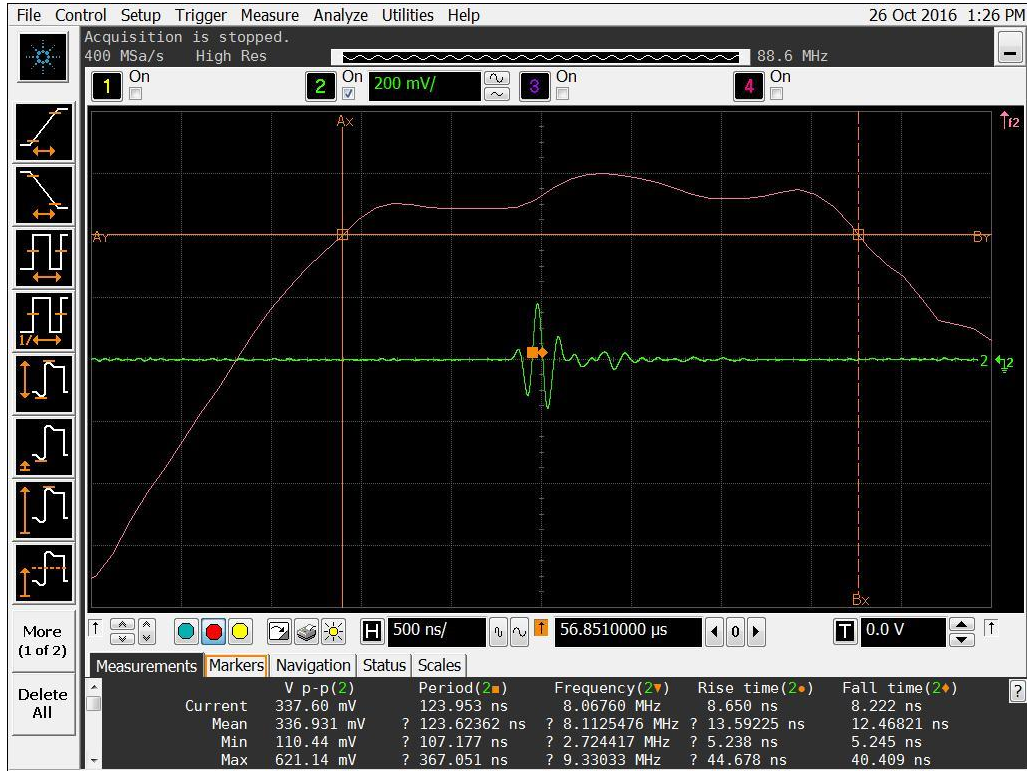


Figure C.3: The measured two-way transfer function of the 64th element of the phased array transducer used in the measurements.



Acquisition: Sampling Mode real time, High Resolution
 Memory Depth manual 2.048 kpts
 Sampling Rate automatic 400 MSa/s
 Averaging off, Interpolation Auto

Channel 2: Scale 200 mV/, Offset 0.0 V, Skew 0.0 s
 Coupling DC, Impedance 50 Ω

Horizontal: Scale 500 ns/, Position 56.8510000 μ s, Reference center

Trigger: Mode edge, Source aux, Slope rising
 Sweep auto, Sensitivity normal, Holdoff Time 100 ns

Function 2: FFT magnitude Channel 2
 Vertical Scale 6.00000 dB/, Offset -45.0969 dBm
 Horizontal Scale 1.00 MHz/, Center Frequency 7.500000 MHz
 Window Hanning, Resolution 300.0 kHz

Measure:

	V p-p(2)	Period(2)	Frequency(2)	Rise time(2)	Fall time(2)
Current	337.60 mV	123.953 ns	8.06760 MHz	8.650 ns	8.222 ns
Mean	336.931 mV	? 123.62362 ns	? 8.1125476 MHz	? 13.59225 ns	12.46821 ns
Min	110.44 mV	? 107.177 ns	? 2.724417 MHz	? 5.238 ns	5.245 ns
Max	621.14 mV	? 367.051 ns	? 9.33033 MHz	? 44.678 ns	40.409 ns
Range (Max-Min)	510.70 mV	? 259.874 ns	? 6.60592 MHz	? 39.439 ns	35.164 ns
Std Deviation	107.987 mV	? 8.96202 ns	? 347.00039 kHz	? 8.46125 ns	7.22312 ns
Number of Meas	2.477 k	1.618 k	1.618 k	2.454 k	2.477 k
Meas Window	Hsin	Hsin	Hsin	Hsin	Hsin
Drag&Drop Time					
Edge Direction		Rising	Rising	Rising	Falling

Markers:

	X	Y
A---(f2)	5.29 MHz	-33.020 dBm
B---(f2)	11.02 MHz	-32.994 dBm
Δ	5.73 MHz	26 mDb
1/ Δ X	174.4 ns	

Figure C.4: The data provided by the manufacturer of the phased array transducer (courtesy: Fraunhofer IBMT). The parameters and respective values at the bottom part of the figure can be clearly seen if this figure is enlarged.